NIMN BASED FERROMAGNETIC SHAPE MEMORY ALLOYS FOR

STRUCTURAL HEALTH MONITORING

A Dissertation

by

NICHOLAS E. BARTA

Submitted to the Office of Graduate and Professional Studies of
Texas A&M University
in partial fulfillment of the requirements for the degree of

DOCTOR OF PHILOSOPHY

Chair of Committee,	Ibrahim Karaman
Committee Members,	Miladin Radovic
	Karl "Ted" Hartwig
	Raymundo Arroyave
Head of Department,	Ibrahim Karaman

December 2018

Major Subject: Materials Science and Engineering

ABSTRACT

With the push for advanced space craft and super structures requiring complex and inventive design and construction, monitoring of these structures will become ever increasingly more important. As the health and safety of the public will rely on the continued performance of these structures, monitoring them for damage and structural failure, or "health", becomes paramount. First among these is acoustic monitoring through the use of piezoelectric sensors interacting with the acoustic vibrations that generally are present during damage processes. Their lightweight and simple construction, along with its ease of miniaturization has permitted their use in a number of civil and aerospace applications for structural health monitoring. Unfortunately, this monitoring method relies on active damage mechanisms to produce measurable acoustic events, can easily be overwhelmed from external vibrations or "noise," and requires the sensors to be robustly designed and remain attached to surfaces for extended periods of time. Despite these drawbacks, it is one of the cheapest and most easily integrated methods for structural health monitoring. Therefore, a need exists to develop an additional system capable of monitoring the structure in the event of acoustic sensor failure, and can quickly confirm and quantify damage detected by the acoustic sensor network.

This work proposes to embed magnetic shape memory particles to interact with stress concentrations at crack tips and operate in conjunction with the acoustic sensors. Magnetic shape memory alloys possess a unique relationship between stress and

magnetization as the material undergoes a martensitic transformation from one crystallographic system to another. Herein, the feasibility of the idea is demonstrated through the consolidation of powder precursors of $Ni_{43}Co_7Mn_{39}Sn_{11}$ magnetic shape memory alloy and pure aluminum. The composite materials demonstrate similar thermo-magnetic properties to the starting $Ni_{43}Co_7Mn_{39}Sn_{11}$, and under certain processing conditions lead to a brittle, dual region diffusion zone that negatively affects mechanical properties of the composite. Composite manufactured with $Ni_{43}Co_7Mn_{39}Sn_{11}$ and aluminum 7075 yield better compatibility between the matrix and sensory particles, and demonstrated a change in magnetization at 300K from 65.8emu.g-1 at 0% compressive strain to 17.5 emu.g-1 at 11.8% compressive strain, successfully demonstrating the feasibility of the proposed method.

DEDICATION

To my mother and father, for inspiring my curiosity.

And to Francesco. I never would have made it without you.

ACKNOWLEDGEMENTS

laughing with me in my darkest hours, your friendship is invaluable. Further thanks to Dr. Daniel Salas Mula, Ben Young, Joel Sam, Dominic Gehring, Jahanzaib Malik, Malesela Mahlatji, Matt Vaughan, Olga Eliseeva, Omer Karakoc, Sezer Picak, Tejas Umale, Wahaz Nasim, Wenhoa Lin, Woohyun Cho, Xavier Huerta-San Juan, Raiyan Seede, Abhinav Srivastava, Alex Demblon, and Willie Trehern. I have learned a great deal from each and every one of you, consider it an honor to call you my friends, and am very thankful to have spent my doctoral years with you.

I would also like to acknowledge Mrs. Lisa Conn, Mrs. Kristine Crawford, Mrs. Gale McGibbon, and Mr. Jeff Setzer for their diligence and compassion as teachers providing an excellent foundation of knowledge on which to build; and my undergraduate professors at the University of Cincinnati for introducing me to the world of materials science and engineering and granting me the framework I needed to come this far.

Lastly, I would like to thank my father and mother, John and Leann Barta, for their unwavering support and motivation throughout my life and for whom I have to thank for cultivating my intense curiosity of the world; to my brothers and sister for their love, support, and (sometimes annoyingly) insightful and difficult questions about my research; and finally to my husband Dr. Francesco de Dilectis. His love, support, motivation, and indomitable ability to make me smile regardless of how terrible the day may have been were the sole reasons I was able to complete this degree. Thank you Francesco, with all the love I have in my heart.

CONTRIBUTORS AND FUNDING SOURCES

Contributors

This work was supervised by a dissertation committee consisting of Professors Ibrahim Karaman, Miladin Radovic, and Karl "Ted" Hartwig of the Department of Materials Science and Engineering and Professor Raymundo Arroyave of the Department of Mechanical Engineering.

The data for Section 3 was provided and partially analyzed by the following collaborators: Dr. Andrew Mott and Dr. Wilson Serem of the Materials Characterization Facility at Texas A&M University; Cole Fincher and Wesley Higgins under the guidance of Professor George Pharr; Vahid Attari under the guidance of Professor Raymundo Arroyave, and Dr. Amy M. Bolon during her time working with Professor Miladin Radovic.

All other work conducted for the dissertation was completed by the student independently.

Funding Sources

NOMENCLATURE

°C	Degrees Celsius
A	Amps
A_f	Austenite Finish
Al7075	Aluminum 7075 alloy
A_s	Austenite Start
At.%	Atomic Percent
BSE	Back Scatter Electron
BVID	Barely Visible Impact Damage
CALPHAD	Calculation of Phase Diagrams
DC	Direct Current
DI	Deionized
DSC	Differential Scanning Calorimetry
EDM	Electric Discharge Machining
EDS	Energy-Dispersive X-Ray Spectroscopy
emu	Electromagnetic Units
FCC	Face Centered Cubic
FOS	Fiber Optic Sensors
g	gram
H	Hardness
Hz	Hertz

K	Kelvin
M_f	Martensite Finish
mm	Millimeter
MPa	Mega Pascals (stress)
ms	Millisecond
M_s	Martensite Start
nm	Nanometer
Oe	Oersted
P	Load
PID	Proportional–Integral–Derivative
P_{max}	Maximum Load Applied
RMS	Root Mean Square
rpm	Rotations Per Minute
RUS	Resonant Ultrasonic Spectroscopy
SE	Secondary Electron
SEM	Scanning Electron Microscopy
SHM	structural health monitoring
SMA	shape memory alloy
SPS	Spark Plasma Sintering
SQUID-VSM	Superconducting Quantum Interference Device-Vibrating Sample Magnetometer
T	Tesla

T_c	Curie Temperature
T_m	Melting Temperature
UTS	Ultimate Tensile Strength
V	Volts
Vol.%	Volume Percent
WDS-EPMA	Wavelength Dispersive Spectrometer-Electron Probe Micro-Analyzer
Wt.%	Weight Percent
μm	Micrometer
μN	Micronewton

TABLE OF CONTENTS

LIST OF FIGURES

xvi

xvii

xviii

LIST OF TABLES

1. INTRODUCTION

1.1 Motivation

The expansion of space missions pushing for interplanetary colonization, and the need for larger "mega" structures requires advancements in monitoring critical components for safety and reliability. Even with the advance of manufacturing capabilities, no material is produced without inherent flaws or defects. Under appropriate loading conditions, these flaws grow in size and diminish the materials capability to perform at optimum levels. Eventually, the growth of the flaw or defect diminishes performance below an acceptable threshold, indicating the material has "failed" [1]. The application of safety factors in designs try to compensate for this eventuality, however if the failure is not correctly identified, the failed component can lead to catastrophic failure of an entire system putting the safety of the general public at risk. The methods and systems employed to monitor the "health" of a structure or component are referred to as "Structural Health Monitoring" (SHM) [2-5]. Each of these methods or systems rely on the fundamental assumption that sufficiently large damage, of a given type, will alter stiffness, or mass or energy dissipation, modifying the dynamic properties of the monitored component or system [1]. This is reasonable as the effects of defects and flaws on material properties are well known [6]. However, implementation of this idea encounters great difficulty as the size scales of the damage trying to be detected is on the orders of microns, while the structure requiring monitoring can be hundreds of meters; additionally, depending on the type of damage being monitored, accumulation of

sufficient damage to render a structure or component "failed" can take fractions of seconds to years [7]. This requires constant monitoring of the given structure using repeatable, accurate measurements on complex systems in typically dangerous and adverse environments [8].

Given the potential for economic loss, nearly every private and governmental industry implement some form of SHM, particularly so for the aerospace industry. It is estimated that 24% of an aircraft's cost is devoted to maintenance of the airframe [9]. Currently maintenance plans are time based, meaning that after a certain time in use, the part or vehicle is retired regardless of actual remaining lifetime (which is often unknown) [1, 5, 9]. A transition then to more informed "condition based maintenance," where parts or vehicles are retired only when they have fully exhausted their usage lifetimes, holds the potential for significant economic impact on manufacturing and usage costs [4, 5, 10-17]. Further reduction in costs could be achieved by implementing statistical models and artificial intelligence to better predict component and vehicle lifetimes [1]. However, to increase the effectiveness of the statistical models and better refine the data for artificial learning, progress must be made in the current ability to accurately detect, locate, and quantify damage [18-20].

The next section will review common methods for damage detection and briefly discuss their advantages and disadvantages (with a focus on acoustic monitoring). It will then propose a method intended to account for some of the deficiencies of acoustic monitoring, and bolster its effectiveness, through the incorporation of magnetic shape memory materials. It will set forth benchmarks for successful demonstration of the

proposed method, and will discuss material selection for the subsequent experiments. These benchmarks for success, sensory material requirements, and discussion on material selection will lay the foundation on which the remaining body of work will be constructed.

1.2 Background

Techniques and systems that monitor the state, integrity, and lifetime of components and structures are known as SHM systems [1, 2]. In general, a mix of sensors and analysis techniques monitor structures from the micro to macro scale to inform users about the state of a material or structure. Since the intent of monitoring extends across the size scale from microns to meters, the ability of a technique to identify and quantify damage is broadly divided into the following four categories: existence, location, type, extent, and prognosis [19], with advanced methods spanning all five categories or a subset thereof. This body of work will focus on techniques and methods that utilize a combination of the first four categories, with a particular focus paid to those that attempt to detect barely visible impact damage (BVID) caused from low velocity impacts and fatigue [21].

Of the methods and techniques developed for flaw detection within a material, four have demonstrated efforts for application in actual structures: surface observation through dyes and penetrants, ultrasonics, fiber optics, and acoustic emission.

Dyes and penetrants have demonstrated effective usage across multiple industries [22]. In brief, a dye or penetrant is applied to a clean surface, allowed to settle and

penetrate surface defects, excess is removed, and a developer is then added to enhance visual contrast [23]. This method is simple, effective for defects that are on the order to be observed with the human eye, and kits general are small, portable, and readily available commercially. The main drawbacks however, is that the surface or part must be accessible to an individual; defects must be on the surface under inspection and sufficiently large to be observed with the eye [23]. While further work has been done to integrate this technique with fiber optics to overcome the limitations of accessibility and surface interactions [24], the technique requires that the crack have interaction with the outside atmosphere. If the damage remains internal, it is difficult to impossible to detect using this technique.

Ultrasonics is another widely used damage detection technique. Along with X-rays, it is one of the only methods that is able to reveal substantial subsurface flaws [23]. High frequency soundwaves, ranging from 5-20kHz, are generated from a transducer and either reflected back to the transducer (pulse-echo) or are transmitted to a secondary transducer (pitch-catch) [23, 25, 26]. This yields information about sample geometry, material properties, flaws beneath the surface, and by scanning across a surface, create 2- and 3-D images of the specimen. Unfortunately, this technique works best when directly attached to a specimen; the resulting data can difficult to analyze requiring extensive training of operators; large surfaces can be time consuming to test; and while applicable to metallic systems, works best in composite to detect damage [21]. Finally, this technique is not able to detect cracks or planar flaws that lie parallel to the traveling direction of the acoustic waves [23].

4

Fiber optic sensors (FOS) have recently sparked interest for structural health monitoring [27], particularly in the civil engineering fields [27-33]. Fiber optic lines are attached to the the structure requiring monitoring, and Bragg gratings are spliced into the lines at period intervals (up to 64). A carefully chosen spectrum of light is then passed through the fiber optic cable, and the reflected frequencies of light are then monitored. Stretching of the fiber optic cable alters the frequency reflected back, due to interactions with the Bragg grating, permitting highly accurate detection in changes of strain [32]. This sensing method is passive, requiring no more energy input that needed to create the light spectrum. Immune to electromagnetic interference, this system is capable of spanning kilometers in length and detecting changes in the system with a resolution two orders of magnitude smaller [34, 35]. This technique however is best implemented in polymer matrix composites, and systems with sufficiently low processing temperatures [32]. Additionally, the fiber optic cable themselves are delicate and are susceptible to fracture during packing, shipping, and installation [32], and are inclined to strain-temperature cross-sensitivity [36]. This makes fiber optics difficult to embed into metallic systems and composites.

Acoustic emission is the last of the common techniques and has demonstrated tremendous growth in its development and application [37-46]. Acoustic sensing employs piezoelectric sensors interacting with the natural vibrations during deformation and damage processes to identify when damage is occurring. Piezoelectric sensors are connected to wire leads, and then adhered to the surface or material under observation. As the material undergoes deformation, dislocation motion, other deformation

mechanisms, i.e. deformation twinning and martensitic transformation, crack propagation, and precipitate fracture release acoustic (physical) vibrations [47]. These acoustic waves then stretch and compress the piezo material, and the subsequent voltage created by the material is recorded and transmitted to a computer for analysis. Waveforms can then be recreated, determining frequencies of vibration, and infer the amount of energy being released [48, 49] and is widely used for metallic systems [21]. As each deformation process occurs at different length and time scales, theoretically all deformation processes have unique signatures that could be identified through acoustic monitoring and analysis. Furthermore, with the advancement of miniaturization techniques and wireless technologies, networks of these sensors can be integrated wirelessly to monitor large structures [11, 23].

Despite this techniques flexibility and scalability, it is possesses a few noteworthy disadvantages. First, the sensors themselves must be robustly manufactured, and attached externally to the structure undergoing monitoring/observation. Sensor failure, or incorrect application of a sensor renders it useless, or unable to function optimally. Second, each damage process is assumed to occur with a well-defined energy level producing unique and specific acoustic emissions [21]. Damage processes that quickly evolve/grow very slowly, or external interference, can be misidentified or missed altogether. Third, and while not directly related to the sensor itself, power loss to the recording system halts all monitoring rendering the sensors themselves useless. These deficiencies can be overcome, however, by combining acoustic emission with an embedded sensory material that directly interacts with the damage (e.g. cracks), and

6

undergoes a fundamental change in its material properties that can be detected externally.

The advantages to embedding a sensory material are threefold. First, by reducing the system that interacts with the damage to a singular material, the likelihood of system failure is reduced. Second, embedding the sensor into the material under observation reduces the issues encountered when trying to attach an external sensor. Finally, the sensory material can be selected to interact with a universal and defining feature of damage and cracks: stress concentrations at crack tips. Selection of an appropriate sensory material for embedding would then need to fulfill the following nine requirements:

1. Assist in location determination

2. Should not initiate damage (i.e. source for cracks)

3. Should demonstrate large change in material response when in presence of damage/crack

4. Preferably metallic

5. Should be embeddable

6. Similar resistance to environmental effects as host (matrix) materials

7. Tailorable threshold for sensing

8. Record that damage occurred even after stimulus has passed

9. Should demonstrate controllable reactions with host (matrix) materials

1.3 SMA and Magnetic SMA as Sensory Materials

An advanced SHM method would employ a non-destructive evaluation method using an embedded sensory material into the structural material that passively monitors the structure and signifies damage to the host material with a notable change in its (the sensory material) properties that would be easily detected [50-54]. The sensory material would need to interact with a unique trait of the propagating damage (for example, stress concentrations at crack tips), and demonstrate a measurably significant change in property or signal once interaction with damage occurred. In addition, any change in property or signal would need to be maintained after interaction with the stimulus, e.g. stress concentrations at crack tips, had passed beyond the sensory material. Shape memory alloys [55-57], specifically magnetic shape memory alloys [58-80], can function as this sensory material and interact with stress fields to fundamentally alter their material properties. In the case of magnetic shape memory alloys (SMAs), the expected change upon interacting with the crack tip stress fields would be in their magnetic properties as the stress can lead to structural phase change in SMAs, and in some magnetic SMAs, the structural phase change, i.e. martensitic transformation, occurs simultaneously with a magnetic phase change. In other words, in magnetic SMAs, one structural phase, for example, parent phase or austenite, can be ferromagnetic while the other phase, martensite, can be paramagnetic or anti-ferromagnetic, and this structural phase change can be induced by stress fields repeatedly.

Before development and application of this idea can proceed, a few simple questions must first be addressed. Firstly, is it possible to embed a sensory material into a host matrix? If successful, does the embedded sensory material retain its ability to undergo the necessary change to its properties for damage detection? What types of properties should the interface between the matrix and sensory material possess to ensure interactions with damage induce changes in the sensory material? Finally, to what degree does the inclusion of the sensory material into the matrix affect the mechanical properties of the matrix?

First steps towards the development of embedded SMA as sensory materials were taken in the early 1990s [50], and was further developed on into the early 2000s [52, 53, 81-83]. Then in 2015, Leser et al demonstrated that NiTi particles, embedded between two plates of Al7050 and monitored via digital image correlation, underwent sufficient strain in the presence of a crack to indicate they underwent martensitic transformation from austenite to martensite [84]. While promising, NiTi does not solve the issues presented with acoustic monitoring. Therefore, we propose to use a magnetic SMA rather than NiTi. Like NiTi, a magnetic SMA would undergo similar martensitic transformations, except that with the correct selection of chemistry, reverse transformation would not occur. Additionally, correct selection of a magnetic SMA would ensure transformation from austenite to martensite would demonstrate almost two orders in magnitude difference in magnetization. In doing this, the sensory particle would be able to interact with a growing crack and "record" the damage even if the acoustic sensors were not available or are malfunctioning. As long as the magnetic

9

signature of the particles was recorded before, a change in the magnetization of an area would indicate the presence of a crack. The size could then be estimated based on the area demonstrating a change in magnetization.

1.4 Material Selection

In the present work, we attempt to demonstrate the feasibility of the proposed method of utilizing magnetic SMAs as sensory materials and begin uncovering answers to the proposed questions. To demonstrate the concept, we have chosen $Ni_{43}Co_7Mn_{39}Sn_{11}$ alloy as the magnetic SMA particles as the sensory material and pure aluminum as the host matrix. The reasons for the selection of this particular magnetic SMA are manifold. Firstly, NiMn(In,Ga,Sn,Sb) based magnetic SMAs demonstrate the largest magnetization changes upon martensitic transformation among all known ferromagnetic SMAs [62, 67, 69, 77, 85-88], structurally transforming between ferromagnetic austenite and anti-ferromagnetic martensite, most of the times fully reversibly, with the change in temperature, or under the application of stress or magnetic field. Co is added to these alloys to increase the Curie temperature of austenite, and thus, the change in the magnetization upon martensitic transformation. Secondly, Sn results in the cheapest alloy as compared to its In and Ga counterparts. Thirdly, the composition $Ni_{43}Co_7Mn_{39}Sn_{11}$ yields a Curie temperature above 400K (127°C) and an Ms near room temperature. Finally, $Ni_{43}Co_7Mn_{39}Sn_{11}$ is much less sensitive to the heat treatments the material may be exposed to during processing, as compared to NiCoMnIn and NiCoMnGa alloys [89-92]. Using a magnetic SMA less susceptible to magnetic property

change over a wide range of processing temperatures would ease processing of the proposed composite, and reduce the likelihood that processing might affect the magnetic response of the sensory material.

As many aerospace vehicle structural components are manufactured with aluminum alloys [93], it would be sensible to select an aluminum alloy often used in aerospace structural components as the host matrix for the magnetic SMA. However, these alloys typically require multistage heat treatments to achieve their well-known material properties. As processing parameters are largely unknown, it is likely this would further complicate the processing of the composite, and efforts demonstrating the effect of including the sensory material into the aerospace grade material. Therefore pure aluminum was selected as the host material instead. While it is understood no structural component would be manufactured from pure aluminum it is an ideal candidate material to demonstrate the feasibility of the proposed idea for the following reasons. Firstly, pure aluminum is an easy material to work with and is readily available in numerous states including powder, bars, sheets, and foils. Secondly, its low modulus of elasticity and high ductility permit large degrees of deformation without fracture, indicating it is amenable to a multitude of processing methods. Finally, any interface that might form between the magnetic SMA and the aluminum matrix due to diffusion would result only from the interactions of aluminum and the magnetic SMA. This would provide insight as to what diffusional products would be expected for aerospace grade aluminum matrices without the influence of alloying elements, easing characterization.

Once sufficient progress has been made using pure aluminum, a transition to aerospace grade aluminum (e.g. Al7075) should be instigated as the ultimate use is intended for aerospace structural components.

1.5 Benchmarks for Successful Integration as Sensory Material

Successful integration of the magnetic SMA as a sensory material will need to achieve the following four benchmarks to demonstrate feasibility:

1. Magnetic SMA particles can be successfully embedded through the consolidation of powder precursor.

2. Magnetic SMA particles retain a magnetic response similar to that of the "parent powder" after embedding in the host matrix.

3. Composite derived from magnetic SMA particles and host matrix must demonstrate a change in magnetic response due to plastic strain in the composite.

4. Any diffusion products between magnetic SMA particles and host matrix require identification.

We believe these are the first four steps that must be achieved to demonstrate feasibility of the proposed idea, and guide successful development of magnetic SMA as sensory materials in this regard.

2. COMPOSITE CONSISTING OF PURE ALUMINUM AND $NI_{43}CO_7MN_{39}SN_{11}$

2.1 Introduction and Background

Given the requirements for the sensory particle to succeed, it was chosen to begin with pure aluminum as an initial matrix material.

2.2 Experimental

2.2.1 Powder Consolidation

High purity aluminum powder (99.9% aluminum by metals basis), sieved to -325 mesh particle size, with an average particle size ranging from 7 to 15µm was purchased from Alfa Aesar (item number 11067). $Ni_{43}Co_7Mn_{39}Sn_{11}$ pre-alloyed powders were fabricated using gas atomization, then sieved to between 27 and 63 µm. The magnetic SMA powder was sealed under an ultra-high purity argon atmosphere in a quartz tube and heat treated at 900°C for 12 hours to homogenize the powder. A small amount of sintering occurred during the heat treatment, however, the powder state was recovered through very gentle grinding with a mortar and pestle.

Three powder compacts were manufactured through the consolidation of the above powders via spark plasma sintering (SPS). The first compact contained only the aluminum powder, while the second and third compacts were a mixture of the aluminum powder and the $Ni_{43}Co_7Mn_{39}Sn_{11}$ powders with a ratio of 90 vol.% aluminum and 10 vol.% $Ni_{43}Co_7Mn_{39}Sn_{11}$. To ensure thorough and homogenous mixing of the powders, low energy ball milling was employed with a ball to powder ratio of 1:1 (using 20 of 6.3

mm and 80 of 3.11 mm stainless steel balls) in a polypropylene jar under an inert atmosphere at a rotational speed of 85 rpm. The stainless steel balls were extracted via sieve and the powder mixture was poured into a 40 mm graphite SPS die. Appropriate amounts of materials were used to yield compacts with a final thickness of 8mm (based on 100% theoretical density).

For each consolidation process, the following sintering procedure was repeated: the graphite die was placed in the SPS chamber and a stress of 5 MPa was applied to the powder (the lowest stress the SPS is able to register). High vacuum atmosphere was then applied on the SPS chamber (10^{-5}Torr). The die and powder were heated with pulsed DC current (20V, 100A; 20/2ms on/off cycles) at a rate of 100°C/min to the required sintering temperature, and was maintained until the consolidation was completed. After achieving the required sintering temperature, stress was increased on the die at the required rate to the sintering pressure, and was maintained until the ram of the SPS registered zero change in position for 60 seconds (except for the 400°C consolidation). **Table 1** summarizes the main processing parameters used.

Table 1. Summary of the main sintering parameters used to fabricate three powder compacts of pure aluminum or Al / $Ni_{43}Co_7Mn_{39}Sn_{11}$ using SPS.

Powder Mixture (Matrix/Additive)	Sintering Temperature (°C)	Sintering Pressure (MPa)	Loading Rate (MPa/min)	Sintering Starting Atmosphere
Al	560	100	100	
Al/$Ni_{43}Co_7Mn_{39}Sn_{11}$ 90/10 vol.%	560	100	20	Vacuum ($\sim10^{-5}$Torr)
Al/ $Ni_{43}Co_7Mn_{39}Sn_{11}$ 90/10 vol.%	400	100	50	

In the case of the 400°C consolidation, the load was held for 10 minutes in an attempt to allow time for the matrix to sinter as much as possible. Previous attempts (not shown here) at consolidating the mixed powders yielded a composite with no diffusion between the $Ni_{43}Co_7Mn_{39}Sn_{11}$ particles and the aluminum matrix at this temperature, and it was thought that adding additional time might allow the matrix to achieve full density and notable diffusion zone. Each compact was allowed to cool in the die to a temperature between 50-80°C before extraction from the SPS chamber and graphite die. This was done to expedite the final cooling to room temperature and permit safe handling for specimen cutting.

The loading rates for each consolidation differed due to initial attempts (not shown here) at consolidating the mixed powders under 100 MPa/min fracturing the graphite die; due to the expansion of the die, the loading rate was reduced by a factor of five for the 560°C consolidation of the mixed powders, and then increased by a factor of 2.5 for the 400°C of the mixed powder when the 560°C consolidation demonstrated success. We do not anticipate that the different loading rates had significant effect on the final compacts.

2.2.2 Microstructural Analysis and Thermo-magnetic Characterization

Small amounts of the as received aluminum and $Ni_{43}Co_7Mn_{39}Sn_{11}$ powders and a small sample of the solution heat treated $Ni_{43}Co_7Mn_{39}Sn_{11}$ powder were mounted to adhesive carbon tape for imaging with an electron microscope.

Portions of the as received gas atomized $Ni_{43}Co_7Mn_{39}Sn_{11}$ and solution heat treated $Ni_{43}Co_7Mn_{39}Sn_{11}$ powders were mounted in epoxy and were mechanically polished using various steps from 600 grit silicon carbide to 0.25 μm diamond suspension at a platen speed of 150 rpm, then vibratory polished for 14 hours in 50 nm colloidal silica solution. A final polish on a polishing media felt cloth and DI water was used to remove polishing media still adhered to the surface of the specimens. The powder specimens mounted in epoxy were then sputter coated with a 6 nm layer of iridium to reduce charging during imaging with an electron microscope.

Specimens for optical and electron microscopy were cut from the compacts containing the $Ni_{43}Co_7Mn_{39}Sn_{11}$ sensory particles using a diamond saw rotating at 100 rpm. These were mechanically polished using various steps starting from 600 grit silicon carbide paper down to 50 nm colloidal silica in the case of the 400°C compact specimens, and down to 0.5 μm diamond suspension in the case of the 560°C compact specimens, at the platen speed of 125-200 rpm. One specimen from the 560°C compact was further polished to 0.1 μm diamond suspension and vibratory polished for 26 hours. A final polish on a polishing media free felt cloth and DI water was used on all specimens as previously stated.

A specimen was also taken from the compact consisting of only aluminum powder consolidated at 560°C. This was mechanically polished from 600 grit silicon carbide paper down to 0.25 μm diamond suspension, then vibratory polished for 5.5 hours in 50 nm colloidal silica solution. A final polish on a polishing media free felt cloth and DI water was used as previously stated.

The thermo-magnetic measurements of the homogenized $Ni_{43}Co_7Mn_{39}Sn_{11}$ powder were carried out using a Quantum Design SQUID-VSM magnetometer with a heating-cooling rate of $10°C.min^{-1}$ for the temperature range of $127°C – -173°C – 127°C$ under constant magnetic fields of 0.05, 1 and 7 Tesla.

Small pieces (2mm x 2mm x 3mm) were cut from the compacts containing the $Ni_{43}Co_7Mn_{39}Sn_{11}$ sensory particles (consolidated at 400°C and 560°C) using the diamond saw and placed in the same SQUID-VSM magnetometer. The magnetization response of the composites were then measured over a temperature sweep from $127°C – -173°C – 127°C$ with a heating-cooling rate of $10°C.min^{-1}$ under a 1 Tesla bias magnetic field. All transformation temperatures were calculated from the magnetization versus temperature plots through the intersecting tangent method. Tangents are taken at the inflection point during transformation and at the linear portions pre and post transformation, with the transformation temperature defined as tangent lines' intersection. Subscripts "s" and "f" were used to denote the onset, or "start," and finish temperatures determined for the martensitic transformation, either from austenite to martensite (M_s and M_f), or martensite to austenite (A_s and A_f).

2.2.3 Mechanical Characterization

Small dog-bone-shaped tension samples with a gauge section of 1.5 mm × 3 mm × 8 mm were cut from the aluminum- $Ni_{43}Co_7Mn_{39}Sn_{11}$ and aluminum only compacts, listed in Table 1, using wire electrical-discharge machining (EDM). Mechanical experiments were conducted on an MTS Systems Corporation MTS 810 servohydraulic test frame

and an extensometer, directly attached to the gauge section of the samples, with the help of ceramic extension rods, was used to record the axial strain. Specimens were loaded at a strain rate of $4.75 \times 10^{-4}(s^{-1})$ until they fractured. Tensile specimens of the aluminum-$Ni_{43}Co_7Mn_{39}Sn_{11}$ compact consolidated at 400°C were not tested because of the high porosity detected in the samples, despite the extended consolidation time.

Single edge notched fatigue crack sample with dimensions 26.2 mm × 8.9 mm × 1.5 mm and a notch size of 1.75 mm were cut from the aluminum- $Ni_{43}Co_7Mn_{39}Sn_{11}$ compact consolidated at 400°C using wire EDM. Fatigue crack growth experiments were carried out on a Deben Microtest 5kN tensile tester (Serial# MT10150). Initiation of a crack in the single edge notch was achieved by cycling load 300-700N thirty times at room temperature; crack growth was achieved by cycling load 450-800N two times at a specimen temperature of 50°C. The specimen temperature during these experiments was controlled by placing an Uxcell 6V 300°C MCH metal ceramic micro heater (dimensions 10 × 10 × 1.2mm), attached to a PID controller and appropriate power supply, directly beneath the fatigue crack specimen in the microtensile stage; specimen temperature was monitored using a K-type thermocouple attached directly to the top surface of the fatigue specimen. Single edge notched fatigue specimens were not cut from the aluminum- $Ni_{43}Co_7Mn_{39}Sn_{11}$ compact consolidated at 560°C due to the debonding of the diffusion region from the aluminum matrix observed after tensile tests of the same material. See Section 4.2 for further discussion.

Observations of crack growth and particle interaction were performed using a Keyence VH-S30K digital optical microscope (the same used for optical microscopy) by

placing the microtensile stage beneath the lens of the microscope during fatigue cracking. Images were taken of various locations before crack initiation, and then in the same locations after crack growth to capture images of the $Ni_{43}Co_7Mn_{39}Sn_{11}$ particles to determine whether or not transformation occurred.

2.3 Experimental Results

2.3.1 Starting Aluminum and $Ni_{43}Co_7Mn_{39}Sn_{11}$ Powders

Figure 1 presents scanning electron microscopy images of the as received starting powders, and the solution heat treated $Ni_{43}Co_7Mn_{39}Sn_{11}$, after gentle grinding with a mortar and pestle. The sizes of the aluminum powder particles (a-c) confirmed the size distribution stated by Alfa Aesar, and ranged from approximately 7 µm to 45µm (325 mesh). The particles displayed elongated structures, with the smaller particles clustered around the larger ones.

The images of the as received $Ni_{43}Co_7Mn_{39}Sn_{11}$in (d) revealed the starting material consisted of mostly spherical particles with small, round protrusions from the surface. A few others were elongated in structure, but also possessed the round protrusions on their surfaces. The microstructure, seen in (e,f), exhibited distinct features of rapid quenching, and the light etching of the dendritic structure indicated phase separation during cooling, similar to what is presented buy Ito *et al* [94].

The reground $Ni_{43}Co_7Mn_{39}Sn_{11}$powder after solution heat treatment, seen in (g), revealed smoother particle surfaces than seen in the as received state, and an exterior marked with small divots. These were likely the result of a small amount of sintering

that formed "necks" between particles during heat treatment, and was subsequently broken during grinding with the mortar and pestle. Particles marked buy the red arrows indicate particles still sintered together and joined by a "neck." The microstructure in (h,i) displayed a homogenous interior with no phase separations or dendrites. This demonstrated the particles were fully homogenized.
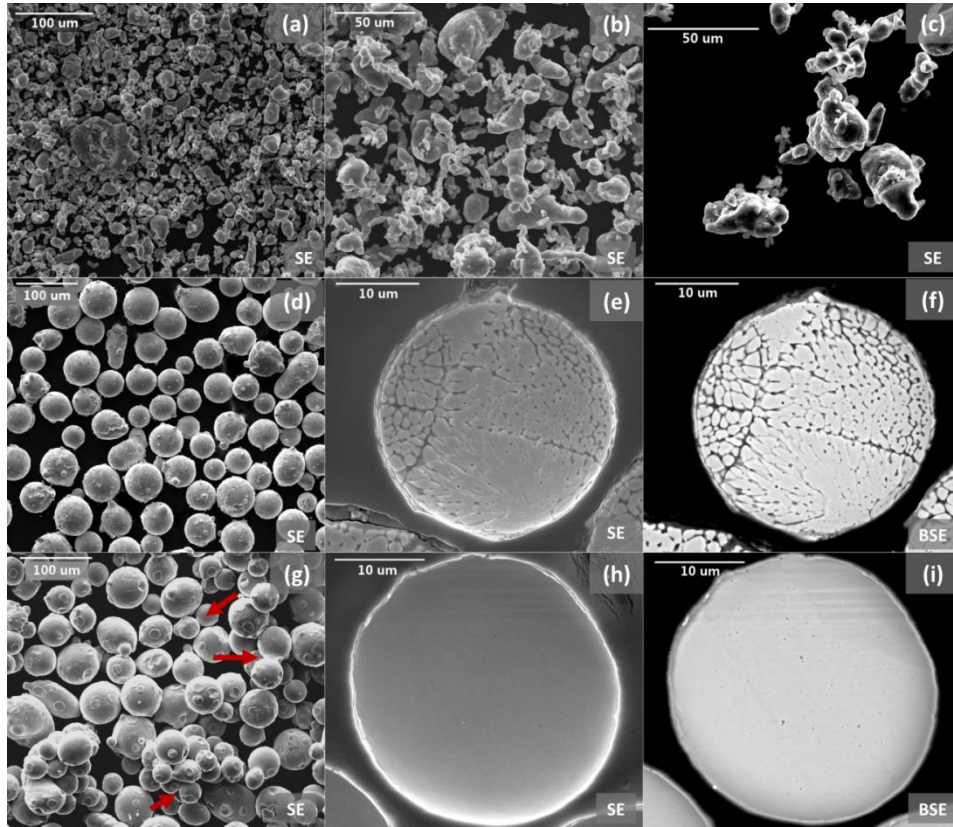
Figure 1. Scanning electron microscopy images of the as received aluminum (a-c), as received $Ni_{43}Co_7Mn_{39}Sn_{11}$ (d-f), and solution heat treated $Ni_{43}Co_7Mn_{39}Sn_{11}$ (g-i) powders. The type of image (secondary electron versus back scatter electron) is indicated in the lower right corner of each image. Partial sintering, or "necking," of the $Ni_{43}Co_7Mn_{39}Sn_{11}$ powder after solution heat treatment is indicated with red arrows in image (g).

Figure 2 displays the thermo-magnetic response of the solution heat treated $Ni_{43}Co_7Mn_{39}Sn_{11}$ powder with increasing bias magnetic field. The powder demonstrated an increase in magnetization for each increase in field intensity from 25 emu.g^{-1} at 0.05 Tesla to 110 emu.g^{-1} for 7 Tesla. The powder demonstrated a distinct shift in the thermo-magnetic response from a broader, more diffuse transformation at 0.05 Tesla during transformation from austenite to martensite, to a condensed and sudden transformation from austenite to martensite at 1 Tesla. The powder retained the distinct and abrupt thermo-magnetic response during transformation for the 7 Tesla bias magnetic field as well. This distinct and sharp change in magnetization indicated massive martensitic transformation in the $Ni_{43}Co_7Mn_{39}Sn_{11}$ particles. The transformation temperatures for each thermo-magnetic curve were determined using the intersecting tangent lines method indicated by the dashed black lines in **Figure 2**. The transformation temperatures and hysteresis measured for the solution heat treated $Ni_{43}Co_7Mn_{39}Sn_{11}$ powder at each field intensity is summarized in **Table 2**.
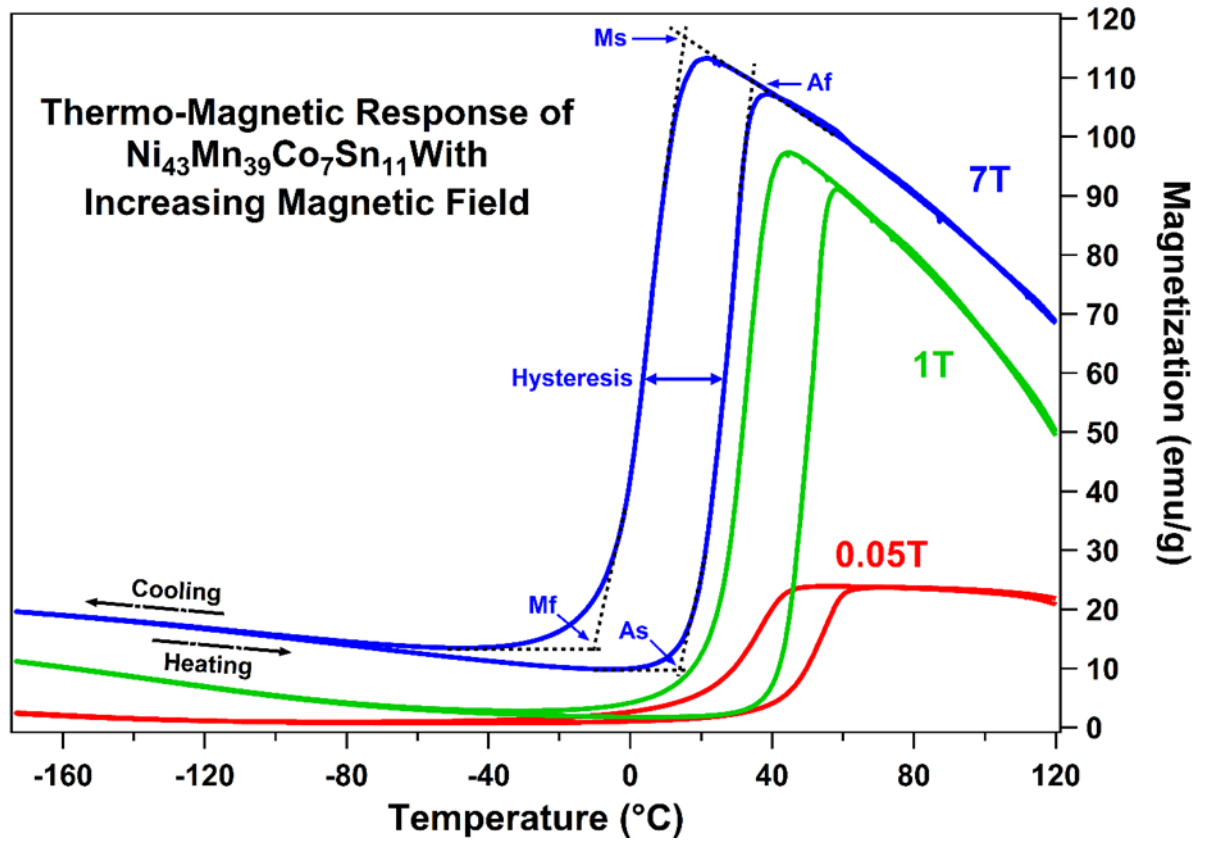
Figure 2. Thermo-magnetic response of solution heat treated $Ni_{43}Co_7Mn_{39}Sn_{11}$ powder under increasing bias magnetic field. Transformation temperatures were determined using the intersecting tangent lines method (represented with dashed black lines), and cooling and heating curves are indicated by black segmented arrows.

Table 2. Summary of the transformation temperatures and thermal hysteresis for the solution heat treated $Ni_{43}Co_7Mn_{39}Sn_{11}$ Powder under increasing bias magnetic field

Bias Magnetic Field (T)	Martensite Start (Ms) (°C)	Martensite Finish (Mf) (°C)	Austenite Start (As) (°C)	Austenite Finish (Af) (°C)	Hysteresis (°C)
0.05	44	20	42	61	19
1	41	24	42	56	18
7	15	-10	14	34	22

The maximum magnetizations for 0.05 and 7 Tesla, as well as their corresponding transformation temperatures, are in good agreement with those reported in the literature [77, 94].

2.3.2 Pure Aluminum consolidated at 560°C

Figure 3 exhibits the microstructure of the 560°C consolidated pure aluminum powder. Given the soft nature of aluminum a high quality polish, free of surface contamination, was difficult to achieve. Despite this, the images revealed a highly dense matrix, with only the occasional pore observed with sizes less than 1 μm. We differentiated pores from surface damage based on the geometries and locations of the marks. Pores demonstrated highly round void shapes along grain boundaries or at grain junctions, while the polishing damage consisted of voids with angular geometries and traversed both grain boundaries and interior of grains. While the interior microstructure of the initial powder was not investigated, we were unable to find any spherical pores or voids within the interior of the grains. This might indicate that they were eradicated during sintering, or the starting powder particles never contained them. Grains sizes of the consolidated materials were on the order with the starting particle sizes of the powder.
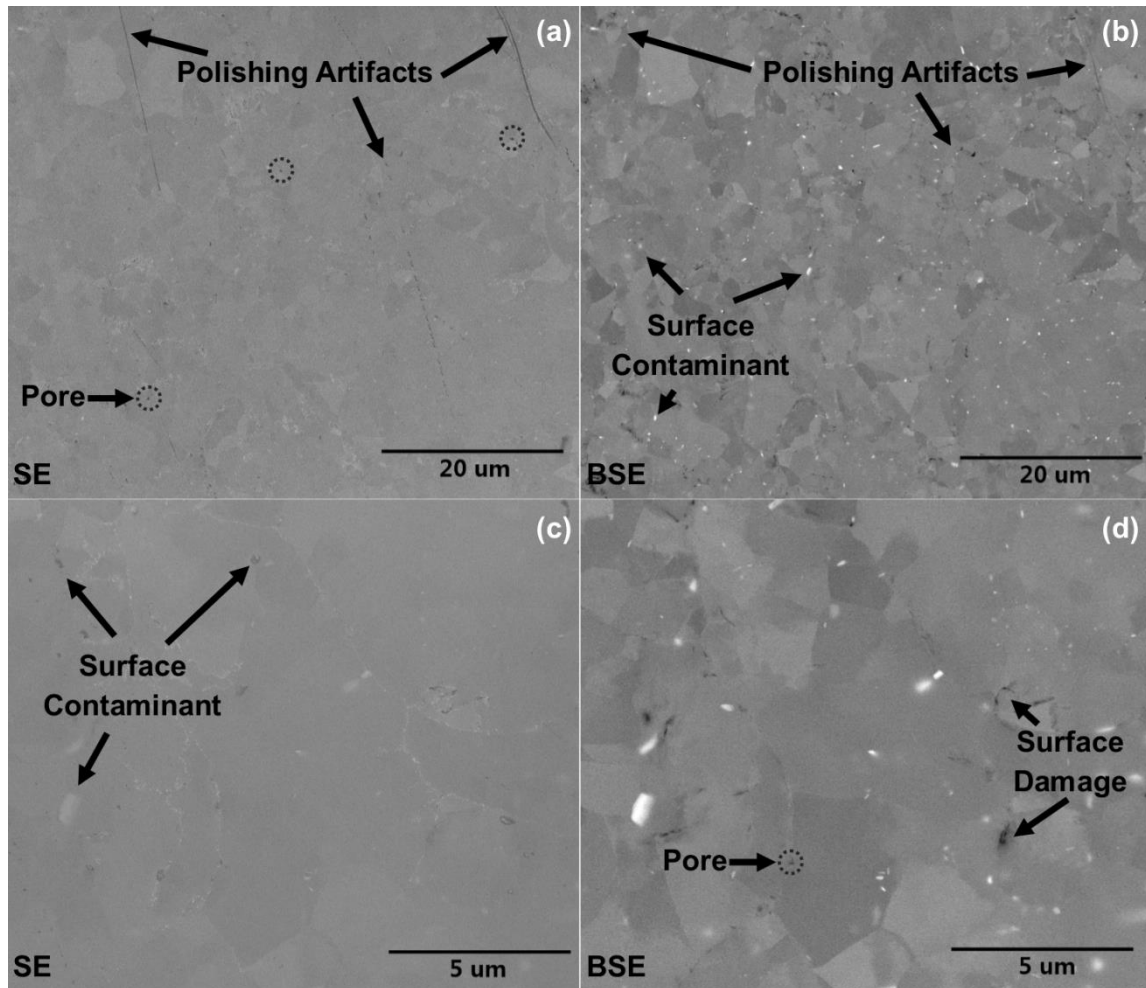
Figure 3. Scanning electron microscopy images of the pure aluminum powder spark plasma sintered at 560°C. Pores are indicated by dashed circles. Secondary and back scatter electron modes are indicated in the lower left hand corners of the images.

2.3.3 Aluminum- Ni$_{43}$Co$_7$Mn$_{39}$Sn$_{11}$ Composite Consolidated at 400°C

Figure 4 shows secondary and back-scattered electron microscopy images of the composites consolidated at 400°C. Here, small pores and voids were observed both in the back-scattered (BSE) and secondary electron (SE) images. The pores exhibited various sizes and shapes, maintaining mostly round geometries, indicative of poor

sintering of powder. No discernable diffusion occurred between the aluminum matrix and the $Ni_{43}Co_7Mn_{39}Sn_{11}$ sensory particles, which could be revealed at these or higher magnifications. Closer inspection of the BSE image at the high magnification revealed martensite variants beginning to form within the $Ni_{43}Co_7Mn_{39}Sn_{11}$ sensory particle. The particles retained their spherical shape, although the lower right edge appears to have flattened due to sintering to another particle that likely occurred while the powder was being homogenized. This is supported the two particles seen still joined by a small neck at the bottom right portion of the lower magnification SEM images and the conjoined $Ni_{43}Co_7Mn_{39}Sn_{11}$ powder particles observed in **Figure 1**.
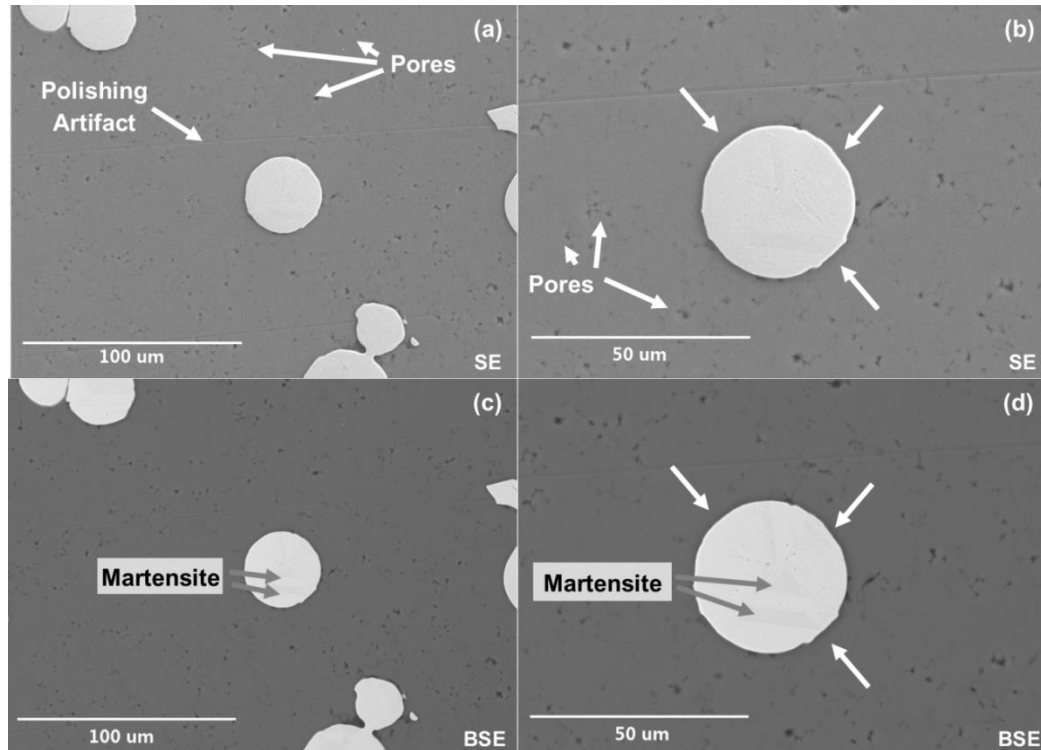
Figure 4. Secondary and back-scattered electron (indicated lower right) scanning electron microscopy images of the Al – $Ni_{43}Co_7Mn_{39}Sn_{11}$ composite material sintered at 400°C using SPS. Note the porosity, and the faint martensite variants forming within the particle.

Figure 5 shows the thermo-magnetization responses of the composite sintered at 400°C under a bias magnetic field of 1 Tesla. Two magnetization versus temperature curves are plotted: the first displays the magnetization normalized to the entire mass of the sample tested. The second shows the magnetization normalized to the estimated mass of the magnetic SMA within the specimen tested (approximately 25 wt%). The magnetization versus temperature curve for the magnetic SMA powder is plotted for reference. Interestingly, both of the curves relating to the magnetic response of the composite material retained the distinct change in magnetization which indicated massive martensitic transformation in the particles.
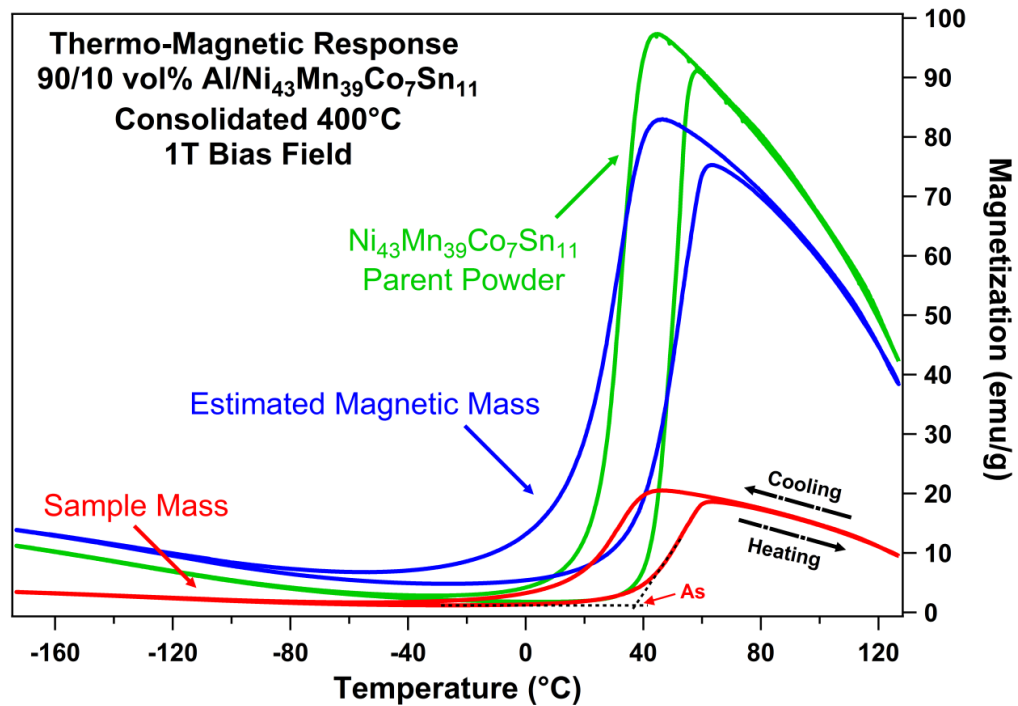
Figure 5. Thermal-magnetization response of the homogenized $Ni_{43}Co_7Mn_{39}Sn_{11}$ powder and the Al- $Ni_{43}Co_7Mn_{39}Sn_{11}$ composite material, sintered at 400°C, under a bias magnetic field of 1 Tesla. Transformation temperatures were determined using the intersecting tangent lines method (dashed black lines).

A distinct difference in shape of the two curves normalized to the different masses was observed, with the response normalized to the estimated mass of magnetic SMA demonstrated a similar response to that of the parent magnetic SMA powder. The shape of both curves show an elongation of the transformation range, and a reduction in maximum magnetization, from 110 emu.g^{-1} for the magnetic SMA powder, to 83 emu.g^{-1} for the curve normalized to the estimated magnetic mass and 20 emu.g^{-1} normalized to the sample mass. The transformation temperatures of the Al- $Ni_{43}Co_7Mn_{39}Sn_{11}$ composite were determined from the magnetization versus temperature curves normalized to the entire sample mass, using the intersecting tangent method previously stated, and are as follows: and $M_s = 40°C$, $M_f = 14°C$, $A_s = 37°C$, $A_f = 61°$. Almost no change was observed in M_s for the composite compared to the magnetic SMA powder, however M_f, A_s, and A_f transformation temperatures demonstrated shifts of -10°C, -5°C, and 5°C respectively when compared to the magnetic SMA powder. The hysteresis for the composite was determined to be 23°C, a 4°C increase compared to the magnetic SMA powder.

The reduction in the overall magnetization observed, once the $Ni_{43}Co_7Mn_{39}Sn_{11}$ sensory particles were embedded in the aluminum matrix in the present composite material, was expected due to having only 10 vol.% (approximately 25 wt%) magnetic SMA particles in the composite. In addition, the change in magnetization of the composite was not as distinct as that of the starting homogenized powder. Still, the transformation of the magnetic SMA particles embedded in the aluminum matrix retained a distinct change in magnetization between the austenite and martensite phases.

Figure 6 shows the polished surface of a single edge notched fatigue crack specimen. The edge of the specimen where the fatigue crack notch begins was the same as the top of the compact from which the specimen was cut; the notch terminated in the direction toward the bottom of the compact. The distribution of the sensory particles was homogenous throughout the composite. The shape of the particles retained the same geometries as those observed in the scanning electron microscopy images of **Figure 1**. The image also revealed either pores that occurred during sintering, or locations where polishing removed $Ni_{43}Co_7Mn_{39}Sn_{11}$ particles. Given the micron size of the pores observed in **Figure 3**, and the scale of the optical microscopy image, it was more likely the observed voids were due to magnetic SMA particle pull out rather than gases trapped during the sintering process. This was a sign that suggested confirmation of no chemical diffusion occurring between the aluminum matrix and the magnetic SMA particle. Had chemical diffusion occurred between the two, it would have been expected that polishing would not have induced enough force to pluck the particles from the matrix.
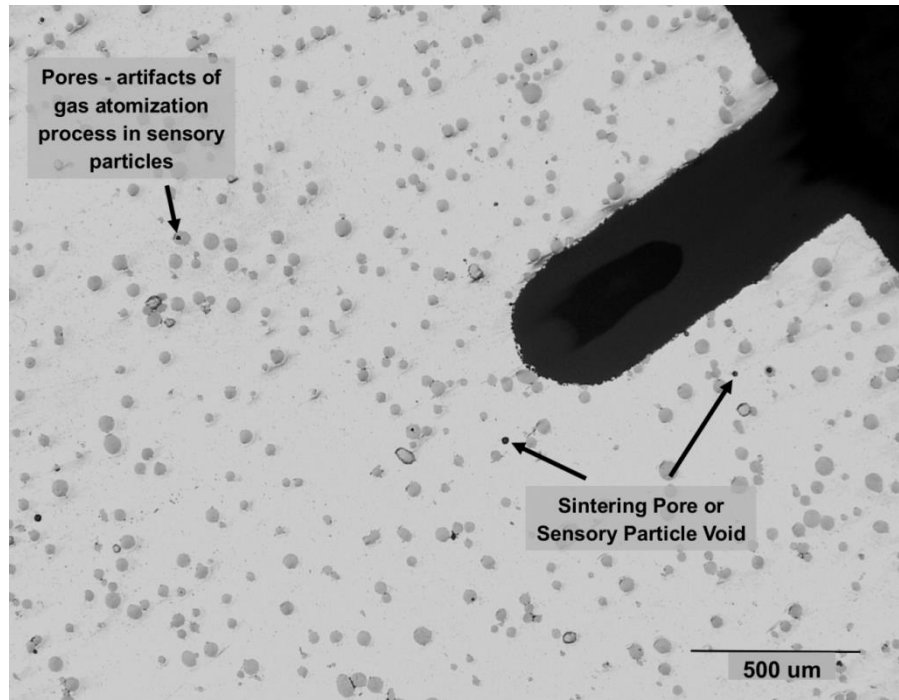
Figure 6. Optical microscopy image of a single edge notch fatigue specimen cut from the Al-$Ni_{43}Co_7Mn_{39}Sn_{11}$ composite material sintered at 400°C. Locations where $Ni_{43}Co_7Mn_{39}Sn_{11}$ particles were missing were labeled as "voids", indicating that the particles were removed during sectioning of the material or during polishing.

Figure 7 shows the optical microscopy images taken during the fatigue testing of the single edge notched specimens cut from the composite material consolidated at 400°C. The top images show the structure before the evolution of the crack. No surface relief of martensitic variants are observed until after the material has been deformed and the crack has passed through or interacted with the particles. The particles not within the path of the crack did not show signs of transformation (surface relief of martensite). Debonding of the particles from the matrix without the transformation, and some fracture between particles was also observed. The appearance of the martensite surface reliefs in particles which are only on the crack path clearly proves that the crack interacts

29

with the magnetic SMA sensory particles and the crack tip and/or wake stress field is

sufficient to induce martensitic transformation in these particles.
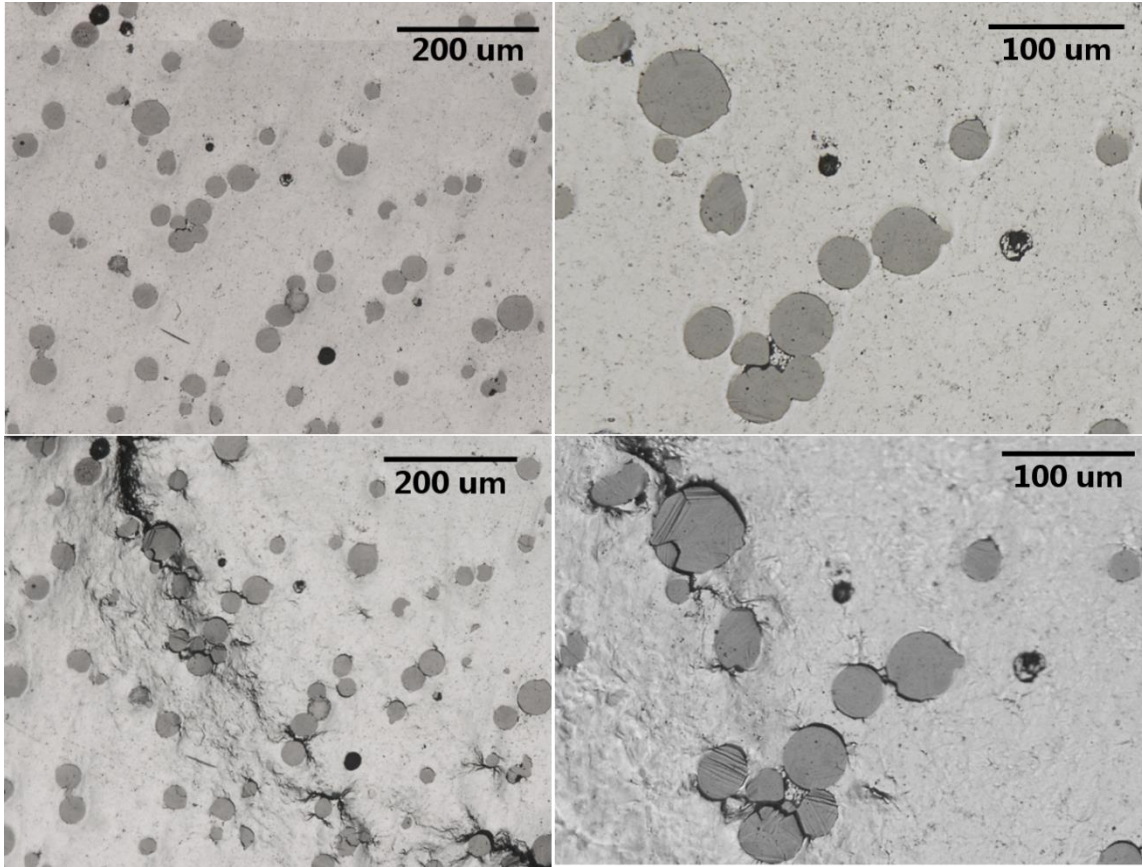
Figure 7. Optical microscopy images of the initial crack-particle interactions in the Al-$Ni_{43}Co_7Mn_{39}Sn_{11}$ composite material sintered at 400°C. The white dashed circle is intended to act as a guide in comparing before (top), and after (bottom) the fatigue crack growth in the material. The black dashed box denotes the regions shown in (b) and (c). The blue arrows in (b) and (d) mark where the martensitic transformation, as seen by the surface relief, was observed after the crack interacted with the $Ni_{43}Co_7Mn_{39}Sn_{11}$ particles. The red arrows indicate debonding of the particles from the matrix.

2.3.4 Aluminum- $Ni_{43}Co_7Mn_{39}Sn_{11}$ Composite Consolidated at 560°C

Figure 8 shows optical and scanning electron microscopy images regarding microstructure of the composite material consolidated at 560°C. The optical microscopy images revealed a diffusion region surrounding most of the particles. Higher magnification showed the magnetic SMA particles exhibited a two phase region within the diffusion zone, and quantitative measurement through image analysis yielded a mean outer diffusion region thickness of 6.89 μm ± 0.5μm, and an inner diffusion region thickness of 3.54μm ± 0.5μm. The electron microscopy images, (b and d), confirmed the two phase region of the diffusion zone, while the back scatter electron image, (d), demonstrated a brighter contrast in the inner diffusion region which suggested the heaviest element of the Al-$Ni_{43}Co_7Mn_{39}Sn_{11}$ system (i.e. tin) segregated during diffusion inside this region. Particles that appeared to be fully consumed by the diffusion region suggested that only portions of their $Ni_{43}Co_7Mn_{39}Sn_{11}$-Al matrix interactions were observed. As the images taken represented a 2D slice through a 3D material, it was possible portions of the diffusion zone for a still intact particle were captured. Electron microscopy also revealed a highly dense aluminum matrix with an occasional pore. More interestingly, at the boundary between the aluminum matrix and the diffusion zone, we observed gaps or voids which may have been indicative of the Kirkendall effect.
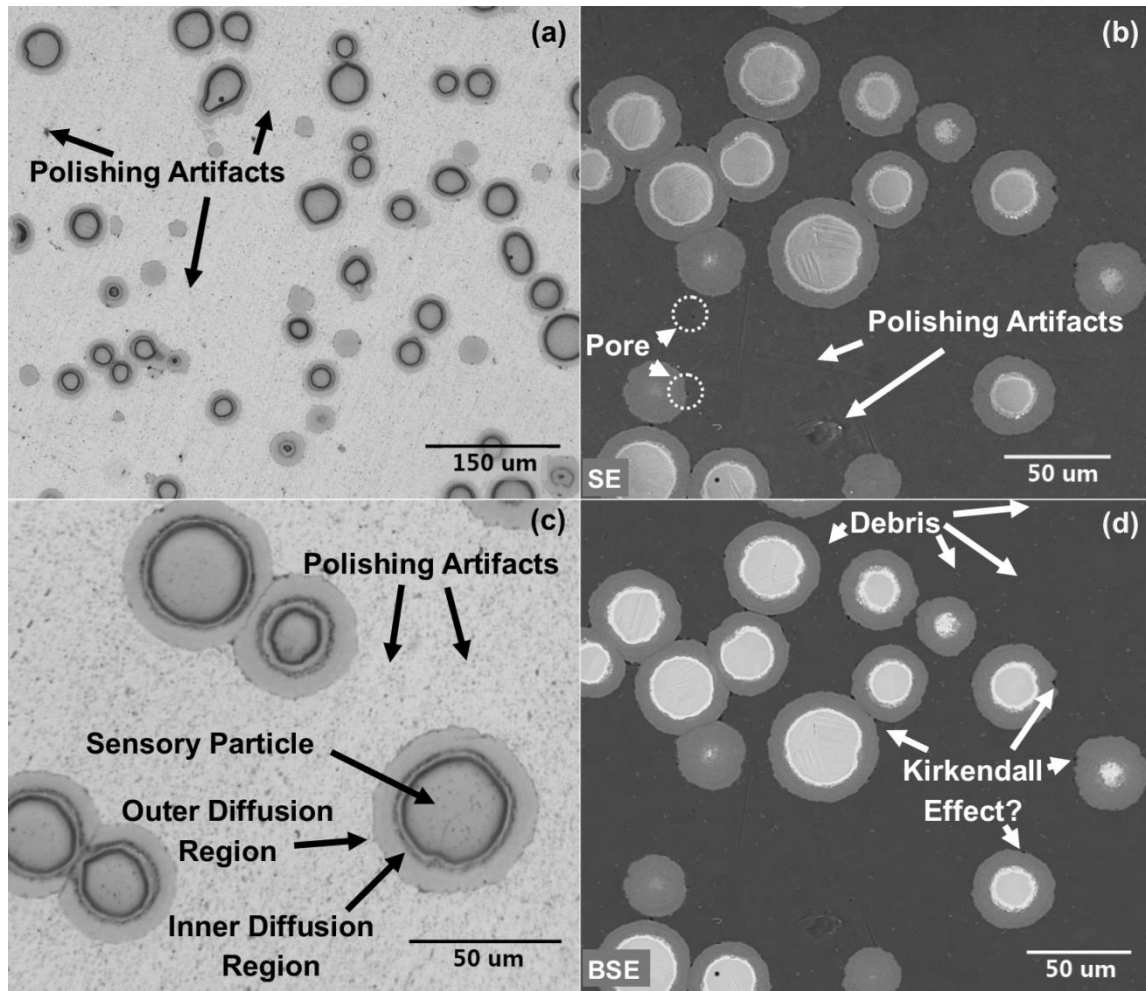
Figure 8. Optical (a,c) and scanning electron microscopy (b,d) of the Al- $Ni_{43}Co_7Mn_{39}Sn_{11}$ composite material sintered at 560°C. Two distinct regions were observed for the diffusion that occurred between sensory particle and aluminum matrix. Electron microscopy revealed a highly dense matrix region with only a few pores observed, and potential signs of the Kirkendall effect at the boundary of the outer diffusion region.

Figure 9 displays the thermo-magnetization response of the composite material consolidated at 560°C with a bias field of 1 Tesla. Again, both the curves for the estimated magnetic mass (representing 23 wt% magnetic SMA material), as well as the mass of the composite as a whole (sample mass) are plotted for comparison. The magnetization versus temperature curve for the magnetic SMA powder is plotted for reference. The two curves demonstrated significantly different intensities as would be expected normalizing the magnetization signal to two noticeably different masses. However doing so emphasized the change in magnetization between the austenite and martensite. Despite this, all of the transformation temperature determinations and comparisons between materials were performed using the magnetization versus temperature curves normalized to the entire mass of the composite sample tested. We believed this to be a more honest and better representation of the magnetic properties of the composite specimen.
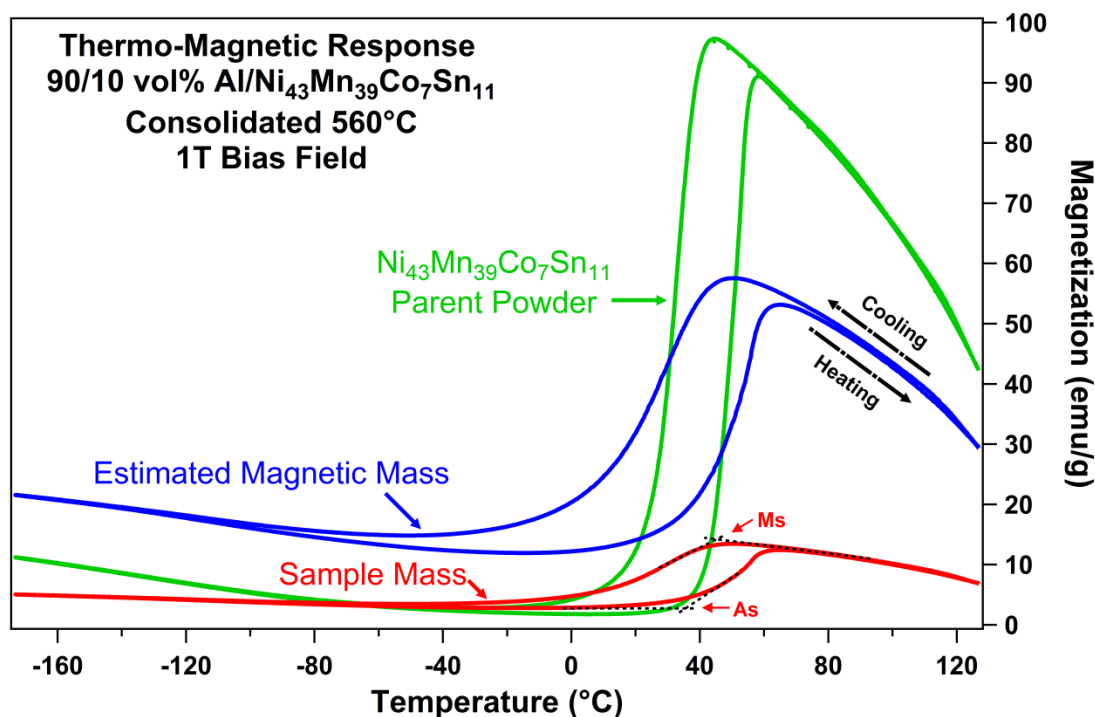
Figure 9. Thermo-magnetization response of the Al – $Ni_{43}Co_7Mn_{39}Sn_{11}$ composite material consolidated at 560°C under a bias magnetic field of 1 Tesla. The magnetization-temperature curves for the estimated mass of the magnetic particles and mass of the composite (sample) are plotted for to demonstrate difference in signal intensity. Determined transformation temperatures used the intersection tangent method and are denoted with dashed black lines. The thermo-magnetic response of the solution heat treated $Ni_{43}Co_7Mn_{39}Sn_{11}$ powder from **Figure 2** is plotted for comparison.

As compared to the results obtained from the composite material consolidated at 400°C, a further reduction in the maximum magnetization was observed: the 400°C composite had a maximum magnetization of 20 emu.g$_{-1}$, whereas only 14 emu.g^{-1} was achieved in the 560°C composite, due probably to the reduction in the transforming volume in the latter as a consequence of the notable diffusion zone. The transformation temperatures measured for the 560°C composite were: $M_s = 47°C$, $M_f = -38°C$, $A_s = 32°C$, and $A_f = 60°C$, using the intersecting tangent lines method, and the transformation

34

hysteresis of 22°C was detected. The M_s temperature increase 6°C above that determined for the parent magnetic SMA homogenized powder, which was expected given the reaction with the matrix material. The two composite shared nearly identical Ms and Af temperatures, but demonstrated distinct differences for Mf and As: -38°C and 32°C, respectively, for 560°C consolidation, and 14°C and 37°C, respectively, for 400°C consolidation.

Figure 10 shows the room temperature engineering stress vs. engineering strain responses of the aluminum and the aluminum − $Ni_{43}Co_7Mn_{39}Sn_{11}$ sensory particle composite samples, both sintered at 560°C. Two specimens were tested from each material to validate the material response. The pure aluminum samples achieved elongation to failure values of 25%, while the composite demonstrated only about 9% elongation. The yield stress for both materials was 90 MPa; however, the pure aluminum samples exhibited an ultimate tensile strength of 120 MPa, while the composite yielded an ultimate tensile strength of only 98 MPa. Both materials demonstrated a highly plastic response despite the ultimate differences.
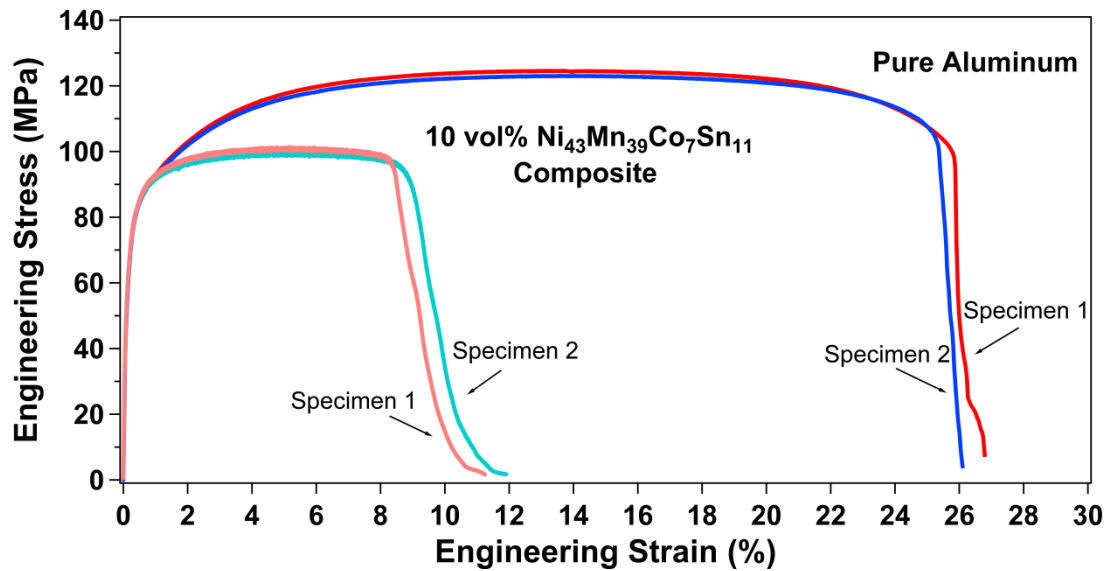
Figure 10. Room temperature true stress vs. true strain response of the consolidated pure aluminum powders, and the composite materials containing 10 vol.% of $Ni_{43}Co_7Mn_{39}Sn_{11}$ particles, both consolidated at 560°C. Two specimens were tested from each case to verify the material response.

Figure 11 displays optical microscopy images of two regions near the facture surface of the tensile tested composite samples before the test and after the failure. Cracks can be clearly seen cutting directly through a notable amount of the sensory particles, but several others either went through the diffusion region only or around the diffusion region/particle. Many polishing artifacts were noted, and a great deal of polishing media remained on the surface, despite extensive cleaning. It also appeared that during the final polishing stage with colloidal silica, grain boundaries of the aluminum matrix were slightly etched. This was unexpected given that it was not observed for the composite material consolidated at 400°C.
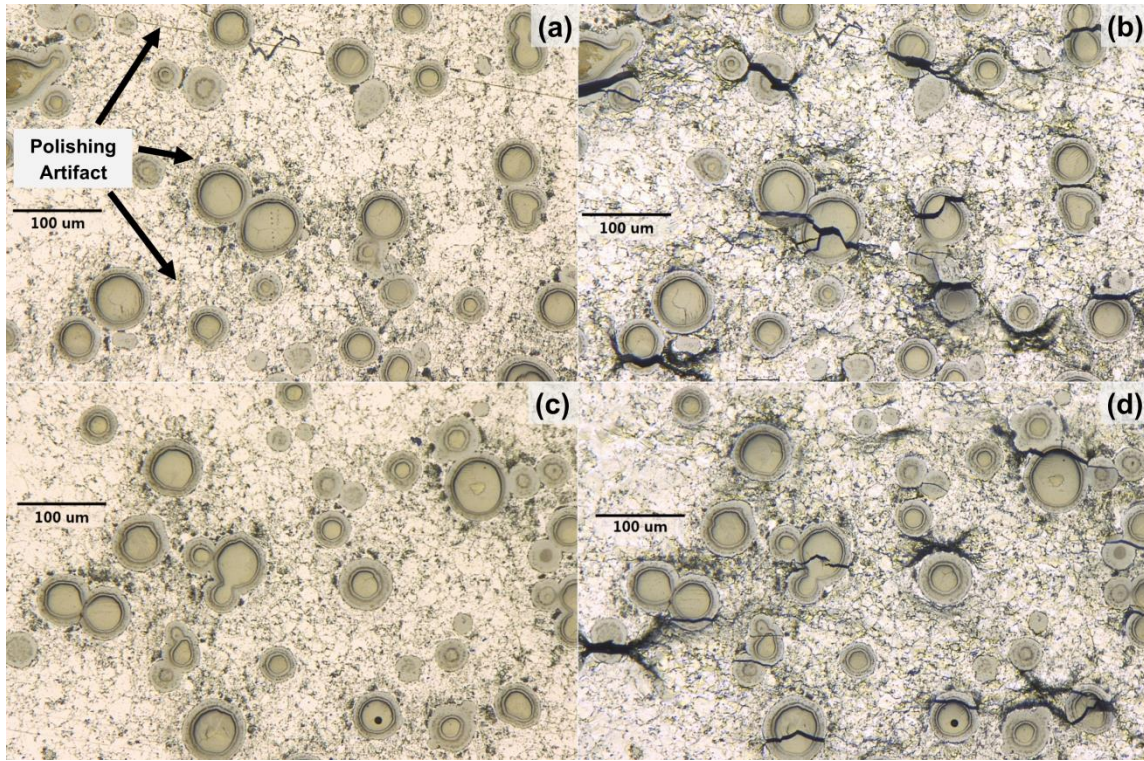
Figure 11. Optical microscopy images of the tensile specimens of the Al – $Ni_{43}Co_7Mn_{39}Sn_{11}$ composite material sintered at 560°C, before ((a) and (c)) and after ((b) and (d)) the tensile testing to failure. Two different regions of the surface of the composite are represented: (a) and (b) are closer to the fracture surface.

2.4 Discussion

In this study, we have shown that $Ni_{43}Co_7Mn_{39}Sn_{11}$ magnetic SMA particles can be successfully embedded into pure aluminum through the consolidation of powder precursors via SPS. Two composite materials $Ni_{43}Co_7Mn_{39}Sn_{11}$ were manufactured and both yielded thermo-magnetic responses comparable to the thermo-magnetic response of $Ni_{43}Co_7Mn_{39}Sn_{11}$ powder. The first composite was processed at 400°C and led to a porous aluminum matrix with no diffusion between the magnetic SMA. Fatigue crack testing of this composite demonstrated that cracks within the matrix caused martensitic

37

transformation in the magnetic SMA particles. In addition, it highlighted the need for strong bonding between the magnetic SMA particles and the matrix. The second composite processed at 560°C displayed a fully dense aluminum matrix with a diffusion zone between the aluminum matrix and the magnetic SMA particle. Characterization of this diffusion zone revealed the likely presence of brittle intermetallics. Comparing the composite to pure aluminum processed similarly demonstrated a significant reduction in UTS and elongation to failure. This was attributed to strain incompatibility between the ductile aluminum matrix and the stiff diffusion region. In this section the effect of temperature on the particle-matrix interactions, the mechanical responses of the composite material, and the effect of processing on magnetic responses of the composites will be discussed in further detail.

2.4.1 Effect of Consolidation Temperature on the Particle-Matrix Interface

In this study, it was shown that the consolidation of the composite powders at 400°C yielded a compact that demonstrated the feasibility of consolidating powder precursors as a means of embedding magnetic SMA sensory particles into a matrix material, while retaining the magnetic response of the magnetic SMA.

No discernable diffusion could be detected between the magnetic SMA particle and the aluminum matrix in any of the images from the composite sintered at 400°C. This indicated the lack of a long range chemical reaction between the particle and the matrix. Additionally, we observed was the similar magnetization response of the composite when normalized to of the magnetic SMA particles within the composite,

which indicated that the magnetic SMA particles retained the ability to transform largely unhindered.

Diffusion between the particle and the matrix was achieved by sintering at 560°C, yielding two distinct regions between the magnetic SMA particle and the aluminum matrix. The overall thickness of the diffusion region was approximately 10μm. The dark outline around the magnetic SMA particle is an optical effect, since due to hardness differences, the diffusion region did not polish as far into the surface as the sensory particle. This left a "ledge" where the diffusion region and the magnetic SMA material met, casting a shadow.

We compared the Al-Ni, Al-Co, Al-Mn, Al-Sn binary phase diagrams and the Al-Mn-Ni ternary phase diagram in an attempt to determine the composition of the diffusion regions [95-99]. Aluminum and tin were noted to be completely insoluble in each other, and is a likely explanation for the two regions observed in the diffusion zone between the magnetic SMA particle and the aluminum matrix. Aluminum-cobalt, aluminum-manganese, and aluminum-nickel pairs all formed numerous line compounds in the binary phase diagrams, and each has a eutectic line around 650°C for the compounds that formed for aluminum concentration ranging from 80-90 at%. Aluminum-nickel were the only pair to produce liquid below 600°C, however, it stopped at 580°C (twenty degrees above the consolidation temperature). Therefore, we were confident no liquid state was produced during the diffusional process. With this information, we propose the following diffusional mechanisms.

At 0.85 T_m of aluminum in equilibrium, the vacancy concentration in the crystal is 10^6 times higher than that at room temperature [100]. Additionally, the atomic sizes of aluminum, nickel, manganese, and cobalt are all within 2 pm (low spin/high spin atomic sizes need not be considered for cobalt and manganese due to processing occurring above Curie point). Given the abundance of the vacancies in the aluminum matrix, it is likely that the top layers of nickel, manganese, and cobalt diffuse first into the aluminum matrix, providing avenues for the aluminum to begin diffusing into the magnetic SMA. As tin and aluminum are insoluble, tin migrates opposite from the aluminum towards the center of the magnetic SMA particle. As diffusion continues, the tin should have greater difficulty penetrating further into the magnetic SMA due to its atomic size, and begin to accumulate, forming the inner diffusion ring around the particles. This slows the diffusion of nickel, manganese, and cobalt from the inside of the magnetic SMA particle to the aluminum matrix, ensuring that aluminum was the predominant element in the outer diffusion region. It is expected then that the outer diffusion region should consist of aluminum-manganese-nickel/cobalt intermetallics (given the relatively low concentration of cobalt in the magnetic SMA, it is expected to substitute for nickel rather than forming a quarternary intermetallic). The formation of the aluminum-manganese-nickel/cobalt intermetallics helps explain why the dark ring around the particles occurred during polishing; the intermetallics are considerably harder than either the magnetic SMA or the aluminum matrix, and would erode much slower during the polishing process.

If the above process is true, then it would be expected to see a core-shell structure with an outer diffusion shell region, an inner diffusion shell of tin-rich material, and a core of the magnetic SMA. **Figure 12** displays the energy-dispersive X-ray spectroscopy (EDS) elemental intensity maps for a magnetic SMA particle in the aluminum matrix consolidated at 560°C (same specimen used for imaging in **Figure 8**) and confirmed the proposed diffusion mechanisms. When the EDS maps were compared with the back scatter electron image taken at the same time, four distinct regions were visible: one containing only aluminum (the matrix), a second containing elemental mixtures of aluminum, cobalt, manganese, and nickel (outer diffusion region), a third rich in tin (inner diffusion region), and a fourth a containing only nickel, manganese, cobalt, and tin (magnetic SMA). Interestingly, there appeared to be a ring of depleted nickel at the boundary of the inner and outer diffusion regions. Given the intensities of the other elements in that region, it is possible a tin-manganese, or tin-manganese-cobalt, intermetallic was present. Additionally, the intensity (and therefore concentration) of manganese in the outer diffusion region was less homogenous than that of nickel, aluminum, and cobalt. It was unknown if this was an artifact of the resolution at which the maps were taken, or if variations in concentration indicated more complex intermetallics. Further quantitative compositional analysis is needed to better understand the development of the diffusion interface between magnetic SMA and aluminum matrix and its diffusional products.
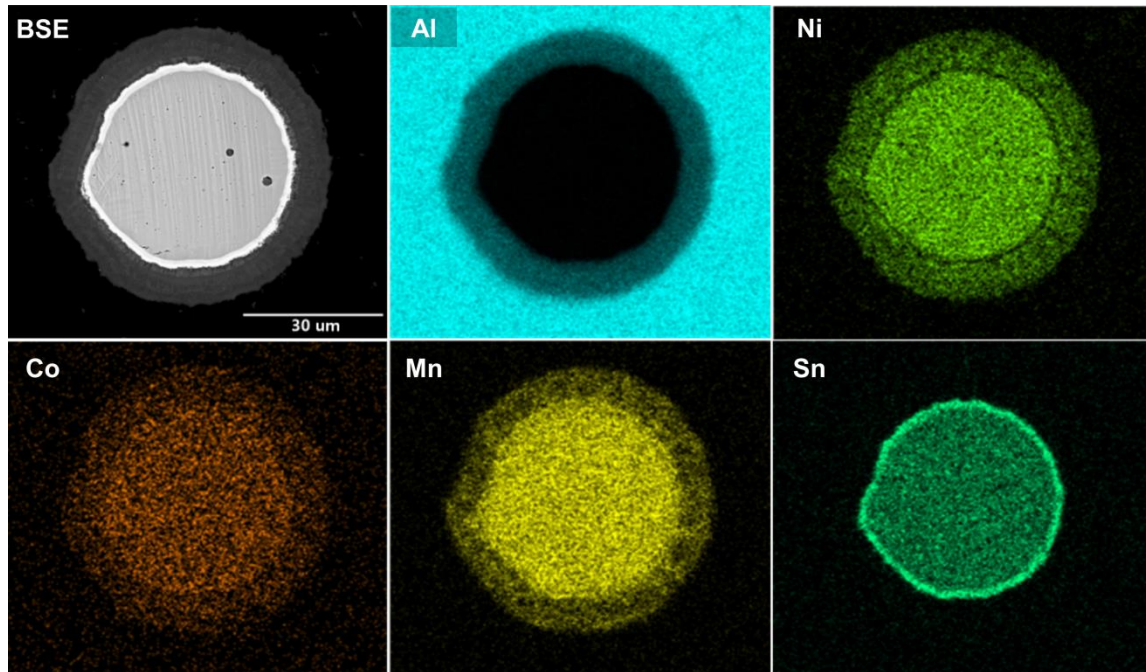
Figure 12. Back scatter electron image and EDS maps of a $Ni_{43}Co_7Mn_{39}Sn_{11}$ particle in the aluminum matrix after consolidation at 560°C. Elemental labels are given in the top left corner of each map, and greater color intensities indicate greater concentration of the particular element. Note the rings of depleted nickel, and greater tin concentration at the boundary of the inner diffusion region and the outer diffusion region.

2.4.2 Mechanical Properties of the Consolidates and Crack-Particle Interactions

Because of the porous nature of the 400°C consolidated composite, mechanical tensile tests were not performed on them. However, the investigation of the 400°C consolidated composite provided a means for preliminary investigation into whether or not cracks moving through the matrix would induce martensitic transformation in the magnetic SMA particles. **Figure 4** showing the optical images taken during the fatigue crack growth experiments confirmed that some particles in the path of the crack did undergo partial transformation as seen by the surface relief of the martensite. They additionally revealed that in some particles, debonding of the particle from the matrix occurred

42

before the particle martensitically transformed. Leser *et al.* noted diffusion between the NiTi particles and the matrix greatly increased the bond strength, and increased the chances of stress transfer from the matrix to the particle [84]. This confirmed the necessity of bonding between the magnetic SMA material and the host matrix for effective transmission of stress, and to ensure the particles did not act as crack initiation sites.

Comparison of the elongation at failure values for the samples from the pure aluminum compact consolidated at 560°C in this study, 26% engineering strain (23% true strain), with the results of Xie *et al.* [101], 12% (assumed engineering strain, type not denoted in publication), demonstrated the notably higher values in our material. This increase might have been caused by the higher pressure used to consolidate the powders (100 MPa in this work vs. Xie *et al.*'s 47 MPa) during the SPS, but might also be the differences in strain rates between methods; Xie et al reported a displacement rate of 0.03mms^{-1}, where as ours was 0.003mms^{-1} (converted strain rate, given specimen dimensions). The order of magnitude difference in testing rates is significant, however, further comparison to results in literature for expected elongation at failure for bulk 1000 – O (commercially pure aluminum plate, annealed) reveals an expected failure at 28% (true strain) at a strain rate of $3.0 \times 10^{-3}(\text{s}^{-1})(0.03 \text{ mms}^{-1}$, converted from given strain rate and stated sample dimensions) [102]. This comparison highlighted the improved mechanical response of our material over Xie et al.'s, however demonstrated that our material did not possess the same mechanical response as bulk aluminum (which is expected of sintered powder products). Despite this, the results indicated that the

processing parameters selected for both powder consolidations of our materials (pure aluminum and the composite) should be adequate to achieve full density in the matrix for good mechanical response.

The pure aluminum powder consolidated at 560°C also did not reveal any large pores. As the composite followed the same processing parameters as the pure aluminum compact, it was unlikely the composite material was poorly consolidated. Additionally, the two materials demonstrated nearly identical yield stresses and Young's moduli. Therefore the large differences in mechanical responses between the two materials were attributed to the creation of the diffusion region between the magnetic SMA sensory particle and the aluminum matrix. Strain incompatibility of the highly ductile aluminum matrix and the rigid diffusion region caused debonding and delamination of the diffusion region/sensory particle from the matrix, nucleating cracks, rather than inducing matensitic transformation in the magnetic SMA material. From these results, it appeared that the thickness of the diffusion region should be optimized to ensure stress transfer from the matrix to the particle without promoting debonding. Further work on processing is needed to confirm ideal thickness of the diffusion region, and optimize its properties.

The before and after images (**Figure 11**) of the tensile tested composite consolidated at 560°C were instructive in regards to why the composite material fails earlier than pure aluminum compacts, and confirmed the believed mechanism of early failure. The cracks appear to initiate at or near the interface of the diffusion region and the aluminum matrix. This was reasonable as the expected intermetallics of the diffusion

region would be strong and brittle compared to the ductile aluminum matrix. The highly ductile matrix would typically not exert enough stress to deform the intermetallic phase(s), and debond instead. A majority of the cracks that interact with the particles propagate through the diffusion region and debonded the particles. In the cases where the magnetic SMA particles were fractured due to the interaction with cracks, the closer inspection revealed that the fractures occurred along the grain boundaries of the magnetic SMA. For the magnetic SMA material to accommodate the strains induced through martensitic transformation across a grain boundary, five deformation systems would be required; this material only possess three [103, 104]. Given the demonstrated brittle nature of the diffusion region between the magnetic SMA and the aluminum matrix, any stresses that were sufficiently high enough to initiate fracture within this zone would have rapidly deformed the particles beyond their limit to accommodate the strain, preferentially fracturing at the grain boundaries (which was observed). The likely intermetallic nature of the diffusion region meant that should stresses reach the critical values needed to transform the magnetic SMA material, the brittle nature of the intermetallic would not permit the necessary strains for the magnetic SMA to do so. Thus the magnetic SMA would debond from the diffusion zone, relieving the stress needed to induce transformation, or the transformation would require further stress, ultimately fracturing the diffusion region and relieving the stress. For these reasons, we chose not perform the fatigue crack experiments on this material, as it was apparent more understanding of the diffusion region was required to ensure desirable performance of the sensory particles.

2.4.3 Effect of Consolidation Temperature on Magnetic Response of the Composites

The thermo-magnetization response of the 400°C consolidate composite demonstrated a neglible change in M_s, along with a 10°C change in M_f and a 5°C change in A_s and A_f as compared to the parent powder. The 560°C consolidated composite demonstrated a 6°C shift in M_s, a -62°C shift in M_f, a 10°C in A_s and a 5°C shift in A_f as compared to the parent powder. The hysteresis for both composite materials increased by 5°C from the parent powder and both possessed very similar shapes, though the 560°C consolidated composite exhibited a more elongated transformation range. The broader, flatter transformation of the both composites was stark in contrast to the sharp and abrupt transition of the parent magnetic SMA powder and indicated that an external influence was slowing or retarding transformation of the magnetic SMA. Shifts in transformation temperatures and changes in transformation ranges of magnetic SMA materials are typically caused by either compositional changes within the magnetic SMA [57, 66, 68, 105-109] or degree of ordering in the austenite phase (i.e. $L2_1$ vs B_2 ordering in this type of magnetic SMAs) [110-112].

The EDS maps in **Figure 12** exhibited a uniform distribution of the nickel, manganese, cobalt and tin elements within the core sensory particle from the composite sintered at 560°C. If diffusion of the elements occurred due to a compositional shift, a gradient of one or more elements would have been expected in the EDS maps for the core magnetic SMA material. As the other composite material was sintered at 400°C with no observed diffusion, we expected no change in that magnetic SMA material. Furthermore Bruno et al determined bulk $Ni_{43}Co_7Mn_{39}Sn_{11}$ does not exhibit significant

changes in transformation temperatures from secondary heat treatments at temperatures up to 600°C [68], since this particular composition and other similar Sn containing NiCoMn magnetic SMAs do not form second phase precipitates, and the crystallographic order in their austenite phase does not change by these heat treatments in contrast to significant changes in the crystallographic order in NiMnCoIn magnetic SMAs [113]. They also demonstrate that only small changes in transformation temperatures (less than 10°C) occurs for $Ni_{46}Mn_{39}Co_4Sn_{11}$ (very similar composition to our material) after aging at 600°C for 1 hour [68]. While these changes in transformation temperatures are more in line with those observed for the 400° consolidated composite, it does not fully explain the broadening of the transformation range for either composite material. Therefore, it is unlikely that either changes in magnetic ordering or composition within the magnetic SMA are causes for the shifts in transformation temperatures and elongation of the transformation range. In the case of the 400°C consolidated composite, a better explanation would be the residual stresses induced by different coefficients of thermal expansion for magnetic SMA and the aluminum matrix, and in the case of the 560°C consolidated composite, a result of the interplay of residual stress and diffusion between magnetic SMA and aluminum matrix.

Since the composite powders were sintered well above the austenite finish temperature, and at a high enough temperature that martensitic transformation in the particles would not be induced via stress, the particles remained in austenite for a majority of the consolidation process and in their spherical shapes. Additionally, the magnetic SMA and the aluminum matrix possess two noticeably different coefficients of

thermal expansion. This means that stresses induced during cooling of the composite between the magnetic SMA and the aluminum matrix would be applied isostatically because of the particles spherical shapes. Noting that dislocation annealing occurs in pure aluminum above 348°C [114], using the equation given below for a spherical inclusion in a composite material [115], we can estimate the residual stresses evolved during the cooling of the composite after consolidation.

$$\sigma_{rad} = -2\sigma_{tan} = \frac{(\alpha_m - \alpha_p)\Delta T}{(1 - 2\nu_p)/Y_p + (1 + \nu_m)/2Y_m}\left(\frac{R}{r + R}\right)$$

where σ_{rad} is the stress in the radial direction, σ_{tan} is the stress along the tangential direction, α_m and α_p are the coefficients of thermal expansion for the matrix and particle, respectively, ΔT is the change in temperature, ν_p and ν_m are the Poisson ratios for the particle and matrix respectively, Y_p and Y_m are the respective young's moduli for the particle and matrix, and r is the distance from the interface and R is the radius of the particle. Here, values for the material constants of $Ni_{43}Co_7Mn_{39}Sn_{11}$ were not readily available; therefore the necessary material constants for NiMnCoIn magnetic shape memory alloys, with similar transformation temperatures, were used instead as the two materials behave very similarly. Noting that the maximum stress occurs at the interface of the particle and matrix, when r=0, then the maximum stress is estimated to be 150 MPa. We determined a minimum distance of 30 μm from the particle was necessary before residual stresses fell below 30MPa.

The stresses caused by a difference in thermal expansion might have affected the transformation temperatures of the magnetic SMA. Hornbogen showed that the austenite phase of a shape memory alloy could be stabilized if there was a geometric limitation to the formation of martensite. If the shape of the austenite is physically constrained, then an additional energy cost must be paid to overcome the stresses induce through the creation of martensite, and the final product will likely yield a mixture of both austenite and martensite [116]. While their system is for coherent particles in a parent phase, something similar might have happened in the 400°C composite. The differences in coefficients of thermal expansion would have induced dislocation generation in the aluminum matrix, strengthening it. This would have confined the magnetic SMA particle, requiring further undercooling to initiate martensitic transformation, and only permitting select variants to form. Because of the stress state of the particle, and the single crystal or oligocrystalline like nature of the magnetic SMA particle, as one variant of martensite forms further variant formation is limited and required more driving force (undercooling) to form. This stretched out the transformation of the material from austenite to martensite, and modified the sharp transition of the free parent powder to the response seen in the 400°C composite.

As each magnetic SMA particle can be treated like a single crystal, orientation will impart a significant effect the strength of the particle. Softer orientations will deform more, while harder orientations will be more resistant to deformation. Noting that the aluminum matrix will have plastically deformed to accommodate the spherical shape of the austenite phase in the magnetic SMA, magnetic SMA particles oriented in

the harder directions would have additional driving force to transform to austenite due to geometric preferences of the matrix. This resulted in the reduction of A_s compared to the parent powder. For the magnetic SMA particles oriented in the softer directions, plastic deformation induced dislocations that stabilized the martensite phase. These particles would require further heating to induce complete transformation back to austenite, elongating the transformation and increasing A_f beyond that of the parent powder.

In the case of the 560°C consolidated composite, the process is made more complicated by the diffusion region. As the composite cooled from 560°C to 400°C, diffusion between the magnetic SMA and aluminum matrix slows and ultimately stops. As cooling continues beyond 348°C, differences in coefficients of thermal expansion between the matrix and diffusion zone begin to generate dislocations in the aluminum matrix, strengthening it as before. In this case, the diffusion region ensures bonding between the aluminum matrix and the magnetic SMA. As the composite cools to room temperature, the stresses inflicted by the matrix are transferred through the diffusion region, however the rigid nature of the (assumed) intermetallic restricts the strain of the magnetic SMA. Therefore even further driving force (undercooling) is required, than in the case of the 400°C, to transform the austenite to martensite elongating the transformation. Again as the individual orientations of the magnetic SMA particles will vary, particles oriented differently will experience different amounts of plastic deformation. As before, those particles oriented in the harder directions quickly change back to austenite (reducing A_s as compared to the parent powder), while the softer

orientations require more driving force (heating) to transform back to austenite and subsequently increasing A_f above what is observed for the parent powder.

2.5 Conclusions

In summary we have successfully demonstrated embedding a magnetic SMA material into a host matrix through the consolidation of powder precursors via SPS. The resulting compacts demonstrated notably different magnetic responses as compared to the parent magnetic SMA powder, but retained the distinct change in magnetization indicative of massive martensitic transformation. Consolidation at 400°C yielded a compact that was porous, and demonstrated successful transformation of the magenetic SMA sensory material in the presence of a crack. It subsequently revealed the requirement for an intimate interface between the matrix and the magnetic SMA sensory material. Consolidation at 560°C yielded a compact with a highly dense matrix and a diffusion zone between the magnetic SMA material and the aluminum matrix. Two regions were found to exist in the diffusion zone, one rich in tin and manganese, the other consisting of aluminum, nickel, manganese, and cobalt. Tensile tests demonstrated an overall reduction in mechanical properties for the composite as compared to pure aluminum powder processed similarly at 560°C. The diffusion region was determined to be highly brittle and the likely cause of the reduction in mechanical properties of the composite. This demonstrated that while a bond between the magnetic SMA and aluminum matrix was required for successful stress transfer and subsequent transformation of the magnetic

SMA, the interface/diffusion region between the magnetic SMA and aluminum matrix needed to be optimized to ensure the particle would not debond from the matrix.

Here the first two benchmarks for successful demonstration of magnetic SMAs as sensory particles have been achieved. Firstly, magnetic SMA particles were successfully incorporated into a host matrix through the consolidation of powder precursors; secondly, the particles were shown to retain similar properties as compared to the parent powder state.

To achieve optimized properties between the magnetic SMA particle and the aluminum matrix, more information about the composition, structure, and mechanical properties are required for the diffusion region. Additionally, as there is limited information available about oligocrystalline or single crystal $Ni_{43}Co_7Mn_{39}Sn_{11}$, the mechanical properties of the particles themselves should also be investigated.

3. MECHANICAL AND QUANTITATIVE ELEMENTAL ANALYSIS OF THE DIFFUSION PRODUCTS BETWEEN $NI_{43}CO_7MN_{39}SN_{11}$ AND PURE ALUMINUM

3.1 Introduction

As seen in the previous section, successful development of a magnetic SMA and aluminum composite was fabricated from powder precursors. To achieve a material with minimal porosity in the matrix, consolidation required temperatures high enough to permit diffusion between the magnetic SMA sensory particles and the aluminum matrix. As diffusion between the magnetic SMA and the matrix is an expected requirement for an effective composite [84], and minimized the debonding between the particles and the matrix, the brittle nature of the diffusion region caused a significant and detrimental reduction of the mechanical properties of the matrix. To move forward with development of a processing schedule that optimized the properties of the matrix, further understanding and information about the diffusion region was necessary. Given that this system had never been studied before, it was not possible to fabricate large scale specimens, and employ macroscale characterization techniques to determine chemical, structural, and mechanical properties. Even it were possible to do so, without knowledge of what existed in the composite material, no direct comparisons could have been performed. Therefore, a more reasonable approach was to investigate and test the magnetic SMA particles and diffusion region within the composite material itself.

3.2 Background

3.2.1 Microscale Quantitative Elemental Analysis

For effective monitoring, the sensory material would ideally be on the order of a few tens of microns. Therefore, any mechanical testing or compositional analysis would need to be effective at the micron scale. We have chosen to perform quantitative elemental analysis with a wavelength dispersive spectrometer equipped electron probe micro-analyzer (WDS-EPMA). This type of device is commonly used to determine elemental concentrations and locations in highly chemically complex specimens [117-122]. It is more precise in determining elemental concentrations than EDS, and less prone to error. As the ultimate microstructure is unknown, and will likely be on the order of 10 μm, high resolution and high accuracy are required.

3.2.2 Micromechanical Testing

For mechanical testing, we have chosen to perform nanoindentation. This offers the ability to directly probe the mechanical properties of the $Ni_{43}Co_7Mn_{39}Sn_{11}$ particles as well as the diffusion zone between the particles and matrix [120, 123-135]. Additionally, combining this with the microstructural and elemental analyses will offer greater insight into the mechanical properties of specific observed features.

3.2.3 $Ni_{43}Co_7Mn_{39}Sn_{11}$ Material Property Confirmation

Finally, the mechanical properties of single crystal and oligo-crystalline $Ni_{43}Co_7Mn_{39}Sn_{11}$ are largely unknown due to its well-known inability to be grown into

large scale singe crystals. Therefore, mechanical properties of the magnetic SMA, e.g. Young's Modulus, will be confirmed through resonant ultrasonic spectroscopy (RUS) of a polycrystalline specimen manufactured from sintering the $Ni_{43}Co_7Mn_{39}Sn_{11}$ powder used as the sensory material. RUS uses wave propagation through a material to determine the vibrational modes for well-known sample geometries, across a frequency spectrum, fit a mathematical model to the observed peaks, and subsequently determine material properties in a number of materials including magnetic SMAs [136-148].

3.2 Materials and Experimental Methods

3.2.1 Material Fabrication and Specimen Preparation

3.2.1.1 Powder Consolidation

Specimens used in the following characterization and analysis were taken from the same materials manufactured in section two.

A third powder compact was made containing only the $Ni_{43}Co_7Mn_{39}Sn_{11}$ pre-alloyed powder (the powder was not heat treated before consolidation). Sufficient powder was used to fabricate a compact that had the dimensions of 40mm diameter and 8mm, and followed the same sintering procedure stated previously, except that the sintering pressure was held for 20 minutes to promote diffusion and densification. The compact was then allowed to cool in the die until 50°C before extraction from the SPS chamber and graphite die. **Table 3** summarizes the main processing parameters used for the $Ni_{43}Co_7Mn_{39}Sn_{11}$ consolidation.

Table 3. Summary of the main sintering parameters used to fabricate the compact of $Ni_{43}Co_7Mn_{39}Sn_{11}$ using SPS.

Powder Mixture (Matrix/Additive)	Sintering Temperature (°C)	Sintering Pressure (MPa)	Loading Rate (MPa/min)	Sintering Starting Atmosphere
$Ni_{43}Co_7Mn_{39}Sn_{11}$	950	100	100	Vacuum ($\sim 10^{-5}$Torr)

3.2.1.2 Specimen Section and Preparation

Two specimens for quantitative compositional analysis by a wavelength dispersive spectrometer equipped electron probe micro-analyzer (WDS-EPMA) were sectioned from the Aluminum- $Ni_{43}Co_7Mn_{39}Sn_{11}$composite material consolidated at 400°C with a diamond saw rotating at 150rpm. These specimens were wrapped in tantalum foil and sealed in separate quartz tubes under ultra-high purity argon. One specimen was heat treated at 550°C for 20 minutes, while the other was heat treated at 550°C for 60 minutes. Both specimens were "air quenched" (removed from the furnace and allowed to cool to room temperature on a heat resistant surface) before extraction from the quartz tube. The specimens were mounted in bakelite and mechanically polished using various steps starting from 600 grit silicon carbide paper down to 0.10 µm diamond suspension at the platen speed of 150 rpm. The specimens were then vibratory polished in 50nm colloidal silica solution for 12 hours. A final polish on a polishing media free felt cloth and DI water was used to remove polishing media still adhered to the surface of the specimens.

One specimen for nanoindentation was sectioned from the Aluminum- $Ni_{43}Co_7Mn_{39}Sn_{11}$ composite material consolidated at 560°C with a diamond saw rotating at 150 rpm with dimensions of 8.75 x 7.25 x 3 mm. This specimen was then subject to

56

the same polishing treatments stated above, except the specimen was adhered to an appropriate mount for auto polishing and a Buehler Ecomet 3 Variable Speed Grinder-Polisher with an AutoMet2000 Power Head was used to auto polish the specimen for the steps preceding vibratory polishing. After polishing, the specimen was removed from the auto polishing mount before nanoindentation was performed. Auto polishing was chosen to better ensure parallelity between the base of the specimen and the indentation surface so as to not obfuscate the indentation results.

One specimen for resonant ultrasonic spectroscopy (RUS), with dimensions 12 x 14 x 2 mm, was electric discharge machined (EDM) from the compact containing only $Ni_{43}Co_7Mn_{39}Sn_{11}$ consolidated at 950°C. The specimen was wrapped in tantalum foil, sealed in a quartz tube under ultra-high purity argon atmosphere, heat treated for 28 hours at 950°C, and "air quenched" as previously stated. Both large planar surfaces were then mechanically auto polished using various steps starting from 600 grit silicon carbide paper down to 0.10 µm diamond suspension at the platen speed of 150 rpm, then the specimen was vibratory polished for 12 hours in a solution of colloidal silica. The edges of the specimen were gently and carefully polished with a high rpm, hand held abrasive polisher to remove EDM residue and as much surface roughness as possible without significantly changing the dimensions of the specimen (final dimensions of specimen were within 100µm of original dimensions).

3.2.2 Characterization Techniques

3.2.2.1 Quantitative Elemental and Diffusion Analysis

EPMA X-ray elemental maps were obtain using a five (5) detector equipped Cameca SXFive electron microprobe in the Materials Characterization Facility at Texas A&M Univeristy (USA) calibrated with pure elemental standards for the following X-ray elemental energies: Al (Kα), Ni (Kα), Mn (Kα), Co (Kα), and Sn (Lα). It should be noted there is some overlap in the Co (Kα) and Sn (Lα) energies, however it is not significant enough to have a detrimental impact on the results. Maps sizes were 670 x 503 pixels (dwell time: 40ms), and 428 x 569 pix (dwell time: 50ms) with a step size of 0.1µm. Maps show elemental distributions as atomic percentages (at.%). A back scatter electron (BSE) image of the location is given for reference as a very minor shift in positioning occurred when the system just before collecting the elemental distributions.

Thermodynamic equilibrium calculations were conducted using the CALPHAD approach [149, 150] as implemented in the Thermo-Calc software [151]. Aluminum was assumed to diffuse into $Ni_{43}Co_7Mn_{39}Sn_{11}$, and the considered concentrations ranged from 0-10 at.% solubility of aluminum in $Ni_{43}Co_7Mn_{39}Sn_{11}$, in increments of 0.1 at.% (in the case of aluminum substituting for cobalt, the range was set to 0-7 at.%). These calculations demonstrated no change in the $Ni_{43}Co_7Mn_{39}Sn_{11}$ alloy, nor any impurity phases, for any concentration of aluminum. As this was contradictory to the observed experimental results, this indicated that diffusion did not occur from aluminum matrix to $Ni_{43}Co_7Mn_{39}Sn_{11}$, but rather from the $Ni_{43}Co_7Mn_{39}Sn_{11}$ particle to the aluminum matrix. Given the more complex state of interaction an alternative approach was applied.

The flux of elemental species in a multicomponent alloy, based on unreduced diffusion coefficients, D_{ik} in an isothermal, and isobaric state is expressed as [152, 153]:

$$J_i = -\sum_k D_{ik} \frac{\partial c_k}{\partial x} = -D_{ii} \frac{\partial c_i}{\partial x} - \sum_S D_{iS} \frac{\partial c_S}{\partial x}$$

where J_i is the flux of species i with respect to the local lattice plane and the summation over k is over all atom species in the crystal, and c is the concentration of species, and should be noted the cross terms can have an appreciable effect on the atomic fluxes. The unreduced diffusivities are related to thermodynamic, and kinetic factors, and are expressed as [153]:

$$D_{ik} = -\sum_{i=1}^{n} L'_{ik} \frac{\partial \mu_i}{\partial c_k}$$

where L'_{ik}, is the proportionality factor and μ_i is the chemical potential. Diffusion coefficients for nickel, manganese, and cobalt were extracted from the MOBFE2 database within the DICTRA package [151, 154, 155]. For simplicity, only the coefficients in the aluminum-based binary systems were considered. The diffusion coefficient of tin in aluminum was obtained from [156].

3.2.2.2 Nanoindentation

Two sets of nanoindentation experiments were performed on the Aluminum-$Ni_{43}Co_7Mn_{39}Sn_{11}$ composite material consolidated at 560°C. The first experiment was a set of 20 7 x 7 indentation grids with an indent spacing of 9μm, loading at 500μNs[-1], hold for ten seconds, and unloading at 2500μNs[-1], with a diamond Berkovich tip on a Hysitron TI 950 Triboindenter in the Materials Characterization Facility at Texas A&M University. Elastic analysis followed the universal stiffness equation, which relates the contact stiffness, S, to the elastic modulus, E [123, 126, 131]:

$$S = \beta \frac{2}{\sqrt{\pi}} E_r \sqrt{A}$$

where β is a geometric constant that depends on the indenter geometry (taken as 1 in this work). The reduced modulus, E_r, is given as follows:

$$E_r = \left(\frac{1 - \nu_i}{E_i} + \frac{1 - \nu}{E} \right)^{-1}$$

where E_i and ν_i represent the elastic modulus and Poisson's ratio of the indenter, whereas E and ν represent the elastic modulus and Poisson's ratio of the indented sample.

The hardness was estimated from the contact area using the relation

$$H = \frac{P_{max}}{A}$$

Both the frame stiffness and the depth-area relationship were empirically determined using a six term fit, based upon the indentation response of a fused silica standard sample with depths ranging between 50 and 300 nm. Optical microscopy images were taken of the indentation grids to correlate indentation position with the force-displacement response.

The second experiment was a series of selective, singular indents on specific regions of the Aluminum-$Ni_{43}Co_7Mn_{39}Sn_{11}$ composite material consolidated at 560°C (same specimen as used in Hysitron experiments). The selective indents were performed using a Nanomechanics iMicro nanoindenter with an InForce 1000 actuator (maximum load capability of 1N) and a diamond Berkovich tip with a constant loading rate over load ($\frac{-\dot{P}}{P}$) of 0.2 s^{-1}. In addition to recording force and displacement, continuous stiffness measurements were also made at a target frequency of 110Hz and a RMS dynamic displacement of 2 nm [128, 129, 131, 134]. The use of continuous stiffness measurement allows observation of the depth-dependency of the measured properties. Elastic analysis, frame stiffness, and the depth-area relationship were determined using methods previously stated. The depth-area relationship was fit based upon a five term fit over depths ranging between 150 and 1000 nm in fused silica.

3.2.2.3 Resonant Ultrasonic Spectroscopy (RUS)

To confirm the Young's modulus measurements acquired during nanoindentation, resonant ultrasonic spectroscopy was performed on a parallelepiped specimen of sintered $Ni_{43}Co_7Mn_{39}Sn_{11}$ powder. Measurements were taken using a custom made high temperature resonant ultrasound spectroscope (HT-RUS) utilizing a commercially available RUS system (Magnaflux Quasar, Albuquerque, NM). The device was modified for high temperature measurements by using large single crystal sapphire extension rods to transmit ultrasound waves to transducers thereby protecting the transducers from the high temperature environment. The parallelepiped specimen was supported by three piezoelectric transducers, and high purity argon was used to purge and maintain an inert atmosphere to hinder specimen oxidation at elevated temperatures.

The specimen was heated at $10°C.min^{-1}$ and held isothermally for five minutes at each desired temperature before the device swept a 10-500kHz frequency range to cover the first 40 eigenfrequencies [137, 141, 143, 144, 146, 148]. Calculations for elastic constants and elastic moduli were determined from RUS spectra using a multidimensional algorithm (Magnaflux Quasar, Albuquerque, NM) that minimizes root-mean-square error between measured and calculated resonant peaks. Initial inputs were sample dimensions, mass, and estimated C_{11} and C_{44} elastic constants.

3.3.1 EPMA-WDS of Diffusion Regions Formed in 400°C Composite Subjected to Secondary Heat Treatment and Predicted Elemental Diffusivities

Figure 13 displays the EPMA-WDS maps for a $Ni_{43}Co_7Mn_{39}Sn_{11}$ particle in the aluminum matrix taken from the composite sintered at 400°C and subjected to 550°C for 20 minutes. Each elemental map was taken at the same location as the back scatter electron (BSE) image, and a diagonal shift in position as compared to the BSE image was noted. This shift was due to a minor error in the mechanism for position the stage from saved coordinates. The colored scale bars depict increasing concentration in atomic percent from black (bottom, lowest) to white (top, highest). Note that each scale bar was optimized to show the greatest change in concentration for each of their respective elements; therefore, aluminum has a concentration range from 0-100 at.%, while cobalt has a concentration range from 0-10.5 at.%. While this slowed direct comparison between each elemental map, it provided means by which finer and more distinct concentration changes over smaller regions were observed. The concentrations of each element within the core $Ni_{43}Co_7Mn_{39}Sn_{11}$ particles were homogeneous and in excellent agreement with the expected nominal concentration of the powder. This indicated no internal diffusion occurred within the particle during the secondary heat treatment to grow the diffusion region, maintaining the original composition.
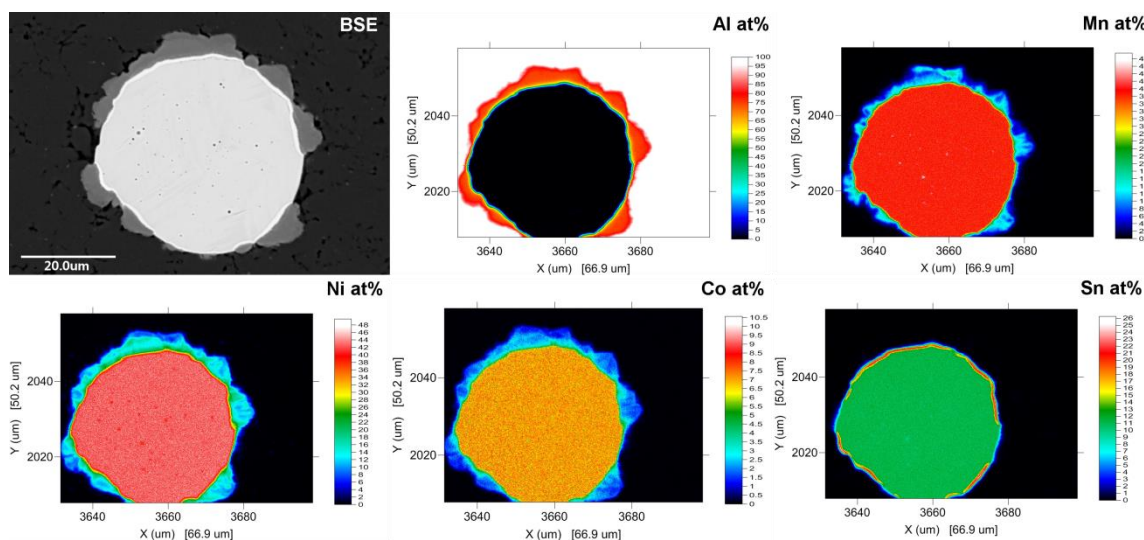
Figure 13. EPMA-WDS elemental concentration maps for a $Ni_{43}Co_7Mn_{39}Sn_{11}$ particle from the composite consolidated at 400°C then heat treated at 550°C for 20 minutes. The color bar to the right of each map has been optimized separately for each element. Elemental labels are given in the top right of each map. For reference and comparison, a back scatter electron image has been provided of the same region in which the maps were taken.

The shape of the diffusion region was noted to be comprised of flares, or fins, radiating away from the core $Ni_{43}Co_7Mn_{39}Sn_{11}$ particle. It was uncertain whether this was caused by the highly porous nature of the aluminum matrix restricting the directional diffusion of the elements in the system, or if this was an effect of rapid diffusion of a singular elements in a narrow cone.

Four distinct regions were observed in these maps. The first region, the matrix, contained 100 at.% aluminum; the second, the outer diffusion zone, contained 70-75 at.% aluminum, 4-24 at.% nickel, 8-24 at.% manganese, 1-3 at.% cobalt, while no tin was observed in this region; more specifically, three distinct phases were observed in the outer diffusion region. Phase I: 75 at.% aluminum, 13 at.% manganese, 10 at.% nickel, and 2 at.% cobalt; Phase II: 70 at.% aluminum, 22 at.% nickel, 5 at.% manganese, and

64

2.5 at.% cobalt; and Phase III: 71 at.% aluminum, 14 at.% nickel, 12 at.% manganese, and 3 at.% cobalt.

In the third region, the inner diffusion region, we observed concentrations were 24-29 at.% manganese, 5.25 at.% cobalt, and 15.5-21 at.% tin, and 0-20 at.% aluminum; specifically, two distinct phases were observed. Phase IV: 29 at.% nickel, 29 at.% manganese, 23 at.% tin, 14 at.% aluminum, and 5.25 at.% cobalt; and Phase V: 42 at.% nickel, 36 at.% manganese, 16 at.% tin, and 6 at.% cobalt. Finally, the fourth region, the $Ni_{43}Co_7Mn_{39}Sn_{11}$particle, comprised of 43 at.% nickel, 39 at.% manganese, 11 at.% tin, and 7 at % cobalt. Additionally, for the portions of the $Ni_{43}Co_7Mn_{39}Sn_{11}$particle not in contact with the aluminum matrix, changes in concentration were only observed for the very edges of the particle, likely caused by edge effects and diffraction of the electron beam, and interactions with the voids between materials. It was not expected this was due to actual changes in composition of the material.

Figure 14 displays the EPMA-WDS elemental maps for a $Ni_{43}Co_7Mn_{39}Sn_{11}$ particle in the aluminum matrix from the composite consolidated at 400°C and subjected to 550°C for 60 minutes. As before, each elemental map was taken in the same location as the BSE image and a diagonal shift in position was noted for the maps as compared to the BSE image; this was due to the minor positioning error as previously stated. The colored scale bars were also optimized for each individual element, as previously stated for the same reasons.
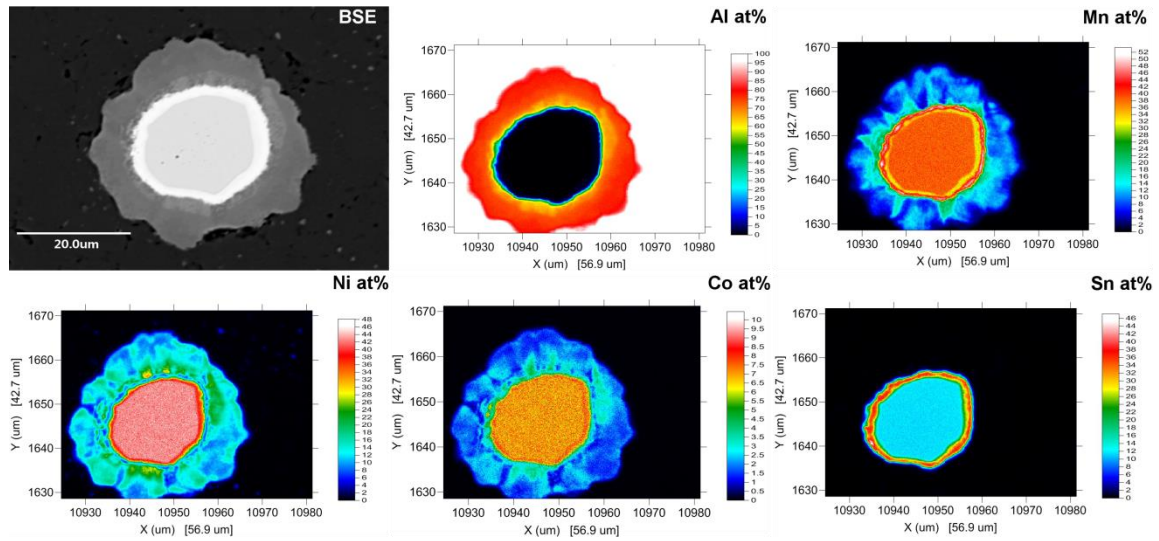
Figure 14. EPMA-WDS elemental concentration maps for a $Ni_{43}Co_7Mn_{39}Sn_{11}$ particle from the composite consolidated at 400°C then heat treated at 550°C for 60 minutes. The color bar to the right of each map has been optimized separately for each element. Elemental labels are given in the top right of each map. For reference and comparison, a back scatter electron image has been provided of the same region in which the maps were taken.

The maps here demonstrated the same four regions of general elemental segregation, but further delineation was observed within those regions. The matrix and core $Ni_{43}Co_7Mn_{39}Sn_{11}$ materials maintained the same concentrations as observed for **Figure 13**, but the inner and outer diffusion regions revealed a richer diversity of diffusional products than previously expected. The outer diffusion region displayed aluminum concentrations of 75-80 at.% at the outer most edge of the diffusion region, while closer to the inner diffusion region a distinct shift to 50-65 at.% was noted. According to the elemental maps, the sudden drop in aluminum concentration was countered by a sudden increase in nickel, manganese, cobalt. What was surprising, is that regions replete in nickel and cobalt appeared to be manganese poor, with the opposite being true as well.

Specifically, four distinct phases were observed in the outer diffusion region. Phase VI: 75 at.% aluminum, 13 at.% nickel, 9 at.% manganese, and 2.75 at.% cobalt; and Phase VII: 75 at.% aluminum, 13 at.% manganese, 10 at.% nickel, and 1.5 at.% cobalt; Phase VIII: 63 at.% aluminum, 25 at.% nickel, 8 at.% manganese, and 4 at.% cobalt. In particular, the right side of the outer diffusion region shows a region containing 65 at.% aluminum, 20-22 at.% nickel, 4-4.5 at.% cobalt, and only 8-10 at.% manganese; and Phase IX: 59 at.% aluminum, 26 at.% manganese, 10 at.% nickel, and 5 at.% cobalt. The geometries of the manganese rich regions were notably similar to the flare and fin shapes observed in the sample heat treated at 550°C for 20 minutes. The regions rich in nickel and cobalt displayed forms more akin to fans and delta formations, which indicated longer diffusion times (which was expected).

Three distinct phases were observed in the inner diffusion region. Phase X: 50 at.% manganese, 38 at.% tin, 10 at.% nickel, and 2 at.% cobalt; Phase XI: 40 at.% manganese, 29 at.% nickel 27 at.% tin, 4 at.% cobalt; Phases XII: 39 at.% nickel, 31 at.% manganese, 23 at.% tin, 7.25 at.% cobalt; and finally the fourth region, the $Ni_{43}Co_7Mn_{39}Sn_{11}$ particle, demonstrated the same concentrations of nickel, manganese, cobalt, and tin seen previously.

The greater diversity in diffusional products within both the inner and outer diffusion regions for the extended time at 550°C suggested the system had not achieved thermodynamic equilibrium after 60 minutes.

3.3.2 Structure and Phase Stability Analysis

A phase diagram based on the equilibria between $Ni_{43}Co_7Mn_{50}$ and Al was calculated and is illustrated in **Figure 15**. $Ni_{43}Co_7Mn_{50}$ system was taken as an approximation for the Heusler particle in this study, and the presence of Sn was neglected due to lack of sufficient data. The studied system is 1 mole, and confined to have 0.5 mole $Ni_{43}Co_7Mn_{50}$, and 0.5 mole Al. It is worthwhile to point out that Sn does not form compounds with Al according to the binary Al-Sn phase diagram, however ternary compounds may form in combination with other elements. Considering the isothermal state of 560 ℃, the diffusion path between $Ni_{43}Co_7Mn_{50}$ and Al passes through different one-, two-, and three-phase regions in which the intermetallic phases BCC_B2(2), FCC_L12, CUB-A13, Al_3Ni_2, Al_8Mn_5, $Al_{13}Co_4$, $Al_{11}Mn_4$ (LT: Low Temperature), Al_9Co_2, and $Al_{31}Mn_6Ni_2$ are thermodynamically stable. For instance, when x_Al=0.5, and T=560℃, the single point phase equilibria calculations indicate that only Al_3Ni_2, Al_8Mn_5, and BCC_B2(2) phases are present, and the mole fraction of these co-existing phases are 0.01324, 0.30332, and 0.68334 respectively.

Figure 15. The calculated phase diagram for Ni43Co7Mn50-Al system. The isothermal line at 560 °C passes through different multiple phase regions that include Cubic-A13, BCC_B2(2), Al_3Ni, Al_3Ni_2, Al_8Mn_5, $Al_{13}Co_4$, $Al_{31}Mn_6Ni_2$, $Al_{13}Co_4$, Al_9Co_2

Here, we limited the discussion to the phases that appear across the isothermal diffusion line at 560℃. Both BCC_B2, FCC_L12 are suffixes that are used to identify ordered BCC, and FCC phase structures with a three sublattice configuration, $A_mB_nC_o$. The site fraction configuration of BCC_B2 phase is $m = 0.5$, $n = 0.5$, and $o = 3$, and the site fraction of FCC_L12 phase is $m = 0.75$, $n = 0.25$, and $o = 1$. Since there are several possible composition sets for these phases, the number in between the parenthesis in front of the suffixes differentiates between these possible states in the phase diagram. CUB_A13 is a Mn-based disordered structure with a two sublattice configuration, A_mB_n where $m = 1$, and $n = 1$ are the site fractions. Al_3Ni_2 is a three sublattice structure with $m = 3$, $n = 2$, and $o=1$ as side fractions. In this configuration, Al always resides in the

69

first sublattice, Al and Ni both can reside in the second sublattice, and Ni, and vacancy interchange role in the third sublattice. Al_8Mn_5 is a three sublattice structure with $m = 12$, $n = 5$, and $o = 9$ as side fractions. $Al_{11}Mn_4$ (LT) , $Al_{13}Co_4$, $Al_{11}Mn_4$ (LT), and Al_9Co_2 are two sublattice structures with site fractions as indicated by their suffixes. $Al_{31}Mn_6Ni_2$ is an orthorhombic fixed stoichiometry ternary compound.

Sn-based thermodynamic data were investigated separately. While limited data is available for Sn-based systems such as Co-Ni-Sn (25℃) [157], and Sn-Ni-Al (25℃) [158], their respective binary phase diagrams indicated Ni_3Sn and/or Ni_3Sn_4 were likely to form. To rigorously define which phases are likely to appear during the evolution of the microstructure, other factors such as driving force for nucleation and kinetic contributions (rate of Al diffusion in NiCoMnSn particle, and/or rate of impurity diffusion in Al) should be carefully investigated. In this respect, **Table 4** summarizes the calculated diffusivities for each of the elements in the $Ni_{43}Co_7Mn_{39}Sn_{11}$ particle within a hosting aluminum matrix. The fastest diffusive elements are tin, cobalt, nickel, and manganese, respectively. However, given the relatively low concentration of cobalt in the system, and immiscibility of Sn in Al, it may be inferred that the impurity phases containing Ni, and Mn are more likely to be observed than those containing Co or Sn.

Table 4. Calculated diffusivities for each element in the $Ni_{43}Co_7Mn_{39}Sn_{11}$within an aluminum matrix at 560°C.

Temperature (°C)	Nickel Diffusivity (m^2s^{-1})	Manganese Diffusivity (m^2s^{-1})	Cobalt Diffusivity (m^2s^{-1})	Tin Diffusivity (m^2s^{-1})	Matrix Element
560	3.12452×10^{-13}	5.77008×10^{-16}	5.07776×10^{-13}	1.6512×10^{-12}	Aluminum

3.3.3 Micro-mechanical Material Response of $Ni_{43}Co_7Mn_{39}Sn_{11}$ and the Diffusion Region via Nanoindentation

3.3.3.1 Indentations Performed with Hysitron

Figure 16 displays a representative set of 7 x 7 grid nanoindentations performed with the Hysitron nanoindentation machine (optical microscopy image on the left) on the composite sample consolidated at 560°C. The corresponding force-displacement curves for each indent in the set are given on the right, with indents of the different regions (matrix, particle, diffusion zone) differentiated by color; orange for the indents performed on the diffusion region, teal for the $Ni_{43}Co_7Mn_{39}Sn_{11}$sensory particle, and blue for the matrix. Indents marked in dark red indicate indents that occurred at boundary regions between the different phases and yielded mixed material responses, and were not used in the analysis of the material properties.

Distinct clustering of material responses was observed in the nanoindentation results and indicated notably different moduli and hardness between the three major phases observed (matrix, diffusion region, aluminum matrix). The diffusion region demonstrated the smallest indentation depth for the maximum load applied, and was

expected given its composition and likely intermetallic phases. Indent depth ranged from 100 nm to 140 nm at peak load. With such small indentation depths, compositional differences between inner and outer regions of the diffusion zone may contribute to the scatter in the corresponding load-depth curves gathered for grid indentation. Due to the quasistatic nature of these indents and lack of knowledge regarding thickness of the diffusion zone directly beneath each indent, the possibility of measurement contamination by the matrix or particulate cannot be discarded for indents in the diffusion region. Inspection of the unloading portion of the curve for the diffusion region demonstrated a highly linear region with a small amount of elastic recovery and indicated a very brittle material with low ductility. This further confirmed the intermetallic nature of the diffusion region.

Indentations on the $Ni_{43}Co_7Mn_{39}Sn_{11}$ particles yielded a tighter cluster of material responses and indicated a uniform material response within the particle. This further supported the observation of the homogenous nature for solution heat treat particles, and confirmed that significant diffusion within the core regions of the $Ni_{43}Co_7Mn_{39}Sn_{11}$ particles did not occur during processing. Indentation depths ranged from 160 nm to 180 nm at peak load, and analysis of the unloading curve demonstrated a highly linear response, with a slight increase in the amount of elastic recovery as compared to the diffusion region. This indicated a softer, more ductile material response than that of the diffusion region.

Indents performed on the aluminum matrix yielded a broad range of indentation depths spanning 540 nm to 640 nm. Analysis of the unloading portion demonstrated

almost no elastic recovery and indicated a soft, highly ductile material (expected of pure aluminum). The broad range in indentation depths was believed to be largely influenced by the distance between indents in the matrix. In an effort to acquire as much information about the mechanical properties of the diffusion region and the $Ni_{43}Co_7Mn_{39}Sn_{11}$ particles, the indentation spacing within the grid was reduced; the cost for this was indents in the matrix being too close together for their size. Furthermore, closer inspection of the indents themselves displayed "pile up" along the outer edges of the indents; this caused further over estimation of material response as the device was not properly calculating contact area with respect to depth. For these reasons, analysis of the indents for the aluminum matrix were not performed for results from the Hysitron.
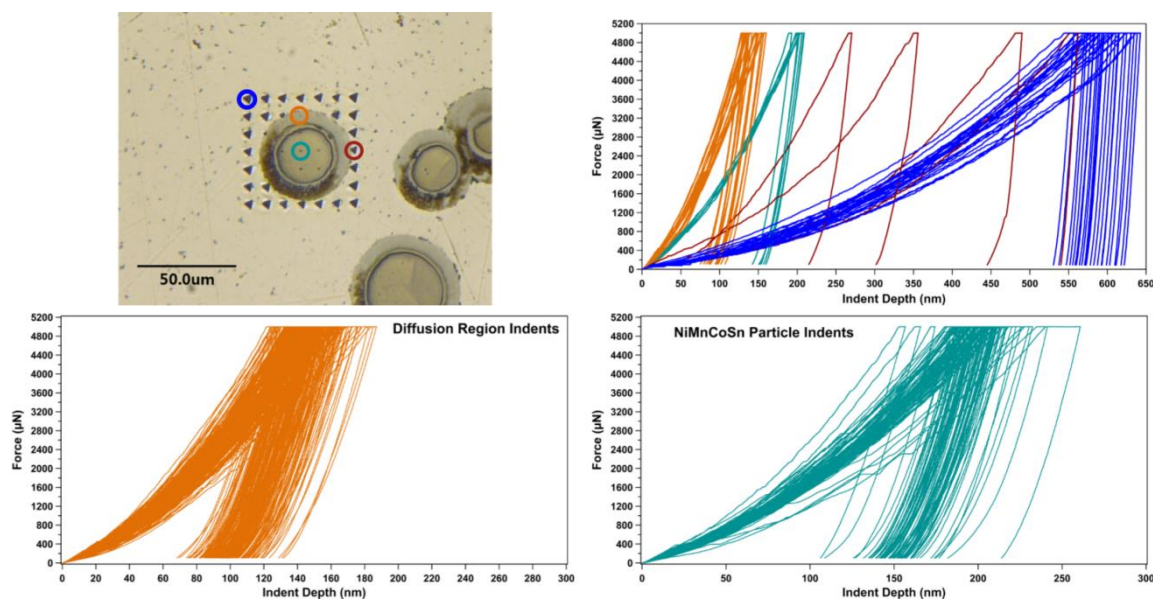
Figure 16. Optical image of a representative nanoindentation grid performed with the Hysitron, the corresponding for force-displacement curves for indents seen in the optical image, and the combined force-displacement curves for the diffusion region and $Ni_{43}Co_7Mn_{39}Sn_{11}$ particles from all 20 sets of 7x7 indentation grids.

3.3.3.2 Indentations Performed with iMicro

Figure 17 displays representative scanning electron microscopy images of indentations performed on the $Ni_{43}Co_7Mn_{39}Sn_{11}$ particles embedded within the aluminum matrix for the composite consolidated at 560°C. The type of image, secondary versus back scatter electron, is indicated in the lower left hand corner of the images. The corresponding force-displacement curves for the four observed indentations are given directly below the micrographs. The inset within the force-displacement plot indicates the hardness and modulus as a function of depth for the curve indicated in black. This same indent is highlighted in the micrographs with a white dashed line. Image analysis of the SEM micrographs confirmed indentation spacing to be greater than or equal to the commonly recommended 2.5 times indentation width.

Indentation depths reached 500 nm (2.5 times the depth for Hysitron data) and peak loads of 22,000 μN (4.4 times that for indents with the Hysitron). The force-displacement curves demonstrated similar shapes to those observed with the Hysitron, largely the highly linear unloading portion with some elastic recovery at the end. All four indents demonstrate acceptable uniformity in the loading and unloading portion of the force-displacement curve, with dissimilarities likely due to indents performed on martensite versus austenite within the particle. The inset plotting hardness and modulus as a function of depth revealed stable material response after a depth of 210 nm was achieved, and the micrographs of the indents do not reveal pile up at the indentation site. The variation of observed material properties is within the expected range for differences between austenite and martensite. Due to the minor differences in material responses

74

between the phases and to simplify the discussion in this paper, analysis of the material properties for the $Ni_{43}Co_7Mn_{39}Sn_{11}$particles will treat each phase (austenite and martensite) as the same rather than differentiating between them.
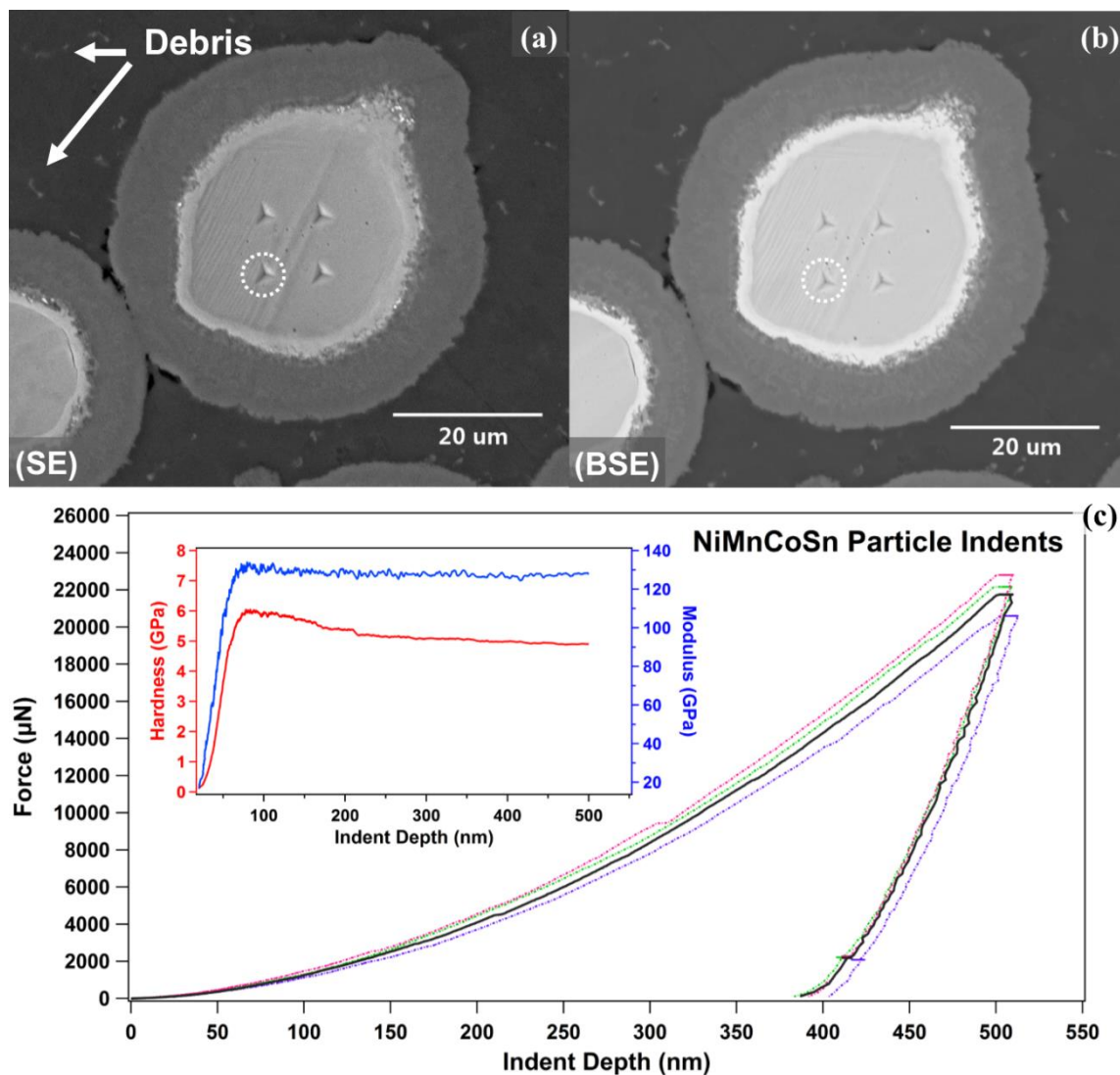
Figure 17. SEM images of representative indentations made on the $Ni_{43}Co_7Mn_{39}Sn_{11}$ particles and their subsequent Force-displacement curves. White dashed circles indicate the indent relating to the dark line in the force-displacement curve, and the insert depicts the hardness and modulus as a function of depth for the same indent.

Figure 18 shows the scanning electron microscopy images for the indentations performed on the diffusion region observed in the composite consolidated at 560°C. Back scatter versus secondary electron is indicated in the lower right of each image with the force-displacement curves for the observed indentations given directly below the micrographs. As before, the inset within the force-displacement plot gives modulus and hardness as functions of indentation depth for the indent marked with a black line (force-displacement plot), with the actual indent highlighted with a white dashed line in the micrograph. Image analysis of the SEM micrographs confirmed the spacing between indents to be greater than or equal to the recommended 2.5 times the indentation width. After the indentation reaches depths in the range of 100-200 nm, the stress field reaches self-similarity. Should a substrate effect contaminate the data, the elastic modulus would decrease or increase as a function of depth. However, because the elastic modulus is constant as a function of depth once elastic-plastic contact has developed, the measurements in the diffusion region do not indicate any contamination from the $Ni_{43}Co_7Mn_{39}Sn_{11}$ or the aluminum matrix.
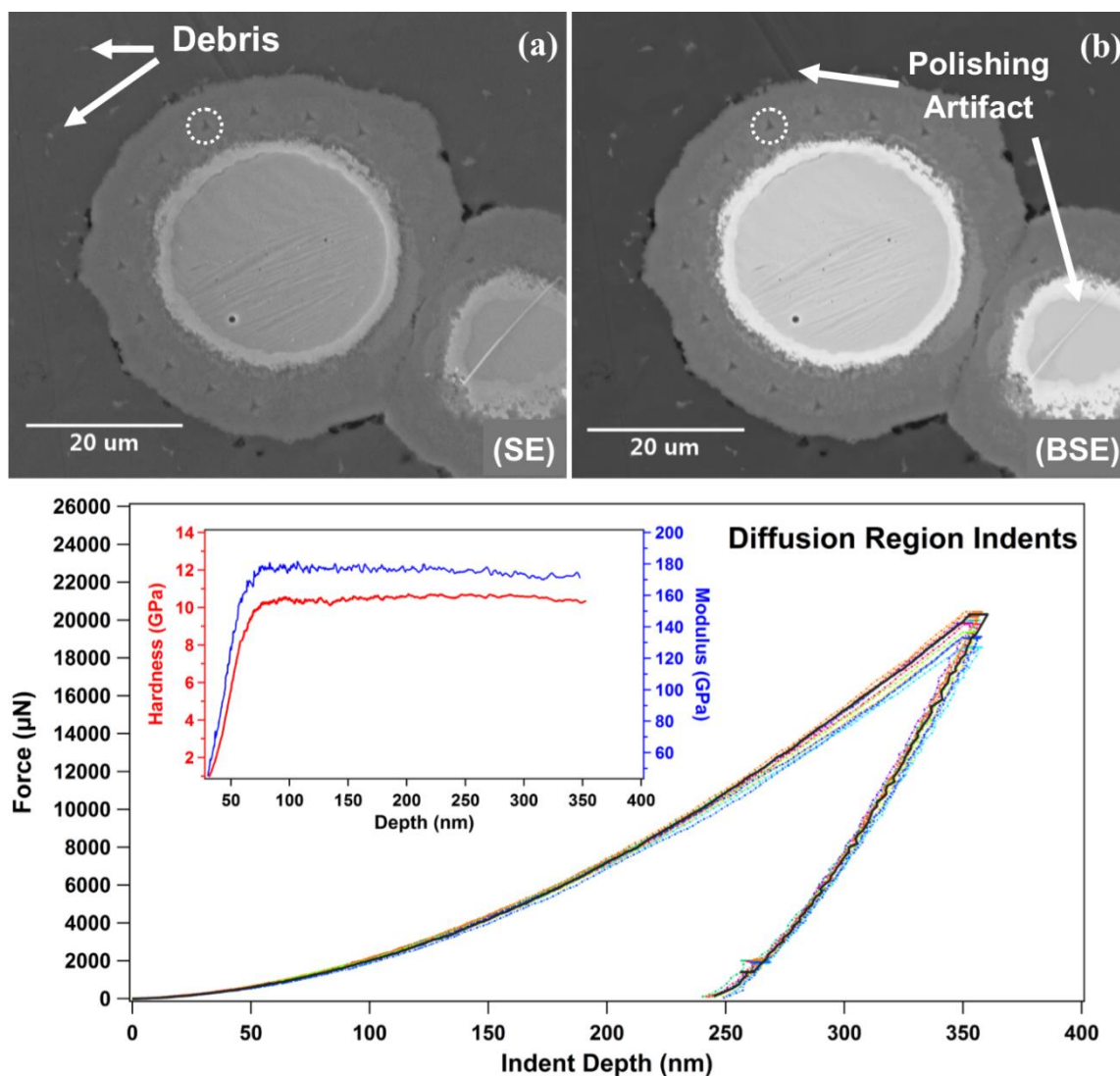
Figure 18. SEM images of the indentations made on the diffusion region. White dashed circles indicate the indent for which the dark line of the force-displacment curves indicates. The insert depicts the modulus and hardness as a function of depth for the same indent.

Comparison of the BSE image with those in **Figure 14** and **Figure 18** indicated the majority of the indents performed here were on in the region predominately containing aluminum-nickel-cobalt and aluminum-manganese phases. Indentations achieved a depth of 350 nm and peak loads 20,000 to 22,000 μN, and the inset of the

force-displacement curves showed a stable material response at a minimum depth of 110 nm. The portions of the force-displacement curves that indicated loading and unloading displayed high uniformity, with the unloading portion indicated a highly linear response with a small degree of elastic recovery at the end. All eleven indents demonstrated high uniformity in material response despite the dissimilarities observed in the microstructure of the region. While no indents were performed within the inner diffusion region (which demonstrated a significant shift in composition), the mean values for hardness and modulus for the diffusion region were determined using this data.

Indentation on the aluminum matrix resulted in residual indent impressions with significant pile up. Using a Keyance VH-Z500 microscope at 5000x magnification, the ultimate contact area at 2 μm indentation depth was measured optically. This ultimate contact area was used for the calculation of both modulus and hardness. For a set of nine indents, the measured elastic modulus and hardness of the Al matrix were 67 ± 1 and 402 ± 20 MPa, respectively. This elastic modulus value agrees well with the values from literature (67 GPa). Pure aluminum samples in literature have yield strengths near 10-20 MPa, or hardnesses near 30-50 MPa (assuming a Tabor constraint factor of 2.8) [159, 160]. However, these hardness values have been observed to increase to 300-400 MPa with cold working [161, 162].

Table 5 summarizes the material properties calculated from the nanoindentation performed by the Hysitron and the iMicro. Comparison of the results from both devices demonstrated that the calculated values lay within a standard deviation of each other. This indicated the observed material properties for the $Ni_{43}Co_7Mn_{39}Sn_{11}$ particles and

diffusion region were accurate. It should be noted that the majority of indents occurred in the outer diffusion region of the diffusion zone, and the mechanical properties reported are indicative of only that region. Further work would need to be done to specifically probe the inner diffusion region and determine if the mechanical properties were similar to that of the outer diffusion region, given that the two demonstrated significantly different compositions.

Table 5. Table summarizing the calculated material properties for $Ni_{43}Co_7Mn_{39}Sn_{11}$ and the diffusion interface with aluminum through nanoindentation.

Device	Region Tested	Number of Indents	Modulus (Mean) (GPa ± σ)	Hardness (Mean) (GPa ± σ)
Hysitron	$Ni_7Mn_{39}Co_7Sn_{11}$	81	129 ± 11	4.9 ±0.7
	Diffusion Region	219	175 ± 15	9 ± 1
iMicro	$Ni_7Mn_{39}Co_7Sn_{11}$	13	127 ± 6	4.5 ± 0.4
	Diffusion Region	11	163 ± 5	10.0 ± 0.3

3.3.4 Microstructure of SPS $Ni_{43}Co_7Mn_{39}Sn_{11}$ and RUS Material Property Determinations

Figure 19 exhibits the microstructure of the $Ni_{43}Co_7Mn_{39}Sn_{11}$ powder sintered at 950°C and solution heat treated for 28 hours at 950°C. Surface deformations were observed, likely remnants form the polishing process, but the general microstructure appeared homogeneous. A few pores and some martensite was noted in a few of the grains and

grain boundaries, however no phase separation or secondary phases were observed. This indicated the material was highly dense and uniform after the sintered and heat treatment processes. Thus it was expected the derived material properties from the RUS experiments would yield material properties for the polycrystalline pure $Ni_{43}Co_7Mn_{39}Sn_{11}$.
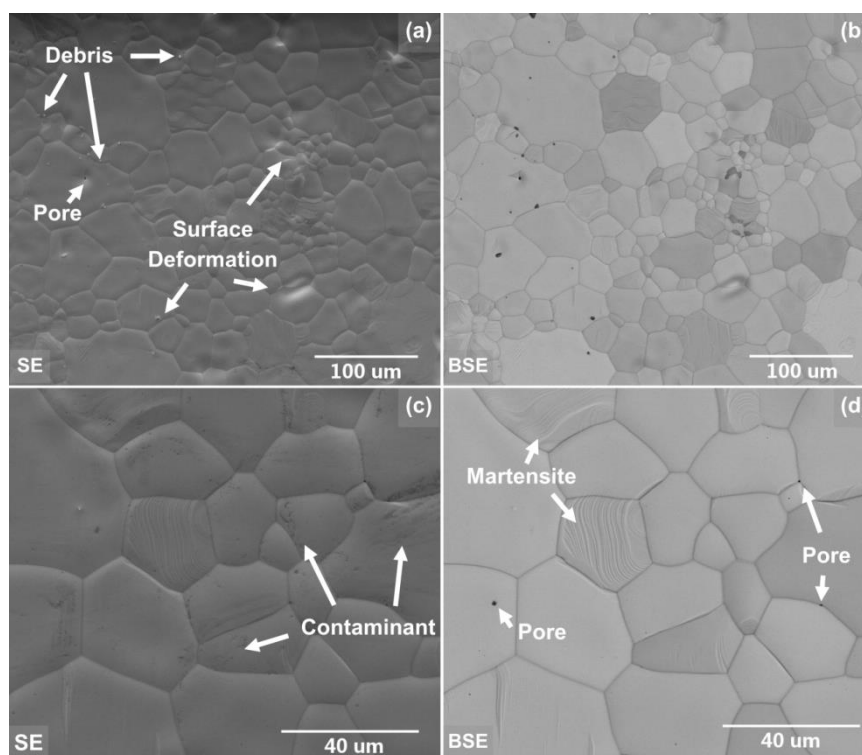
Figure 19. Scanning electron micrographs of the sintered $Ni_{43}Co_7Mn_{39}Sn_{11}$powder at 950°C.

Figure 20 exhibits the cooling and heating thermograms acquired from the differential scanning calorimetry performed on a portion of the $Ni_{43}Co_7Mn_{39}Sn_{11}$powder sintered at 950°C and heat treat for 28 hours at 950°C. Transformation temperatures are

indicated at the intersection of the tangents, and are summarized in the inset table. The colored circles overlaid on the heating curve indicate the temperatures at which the RUS experiments were performed. The martensite finish and austenite start temperatures presented some difficulty in their determination as the transformation regions were elongated and diffuse.
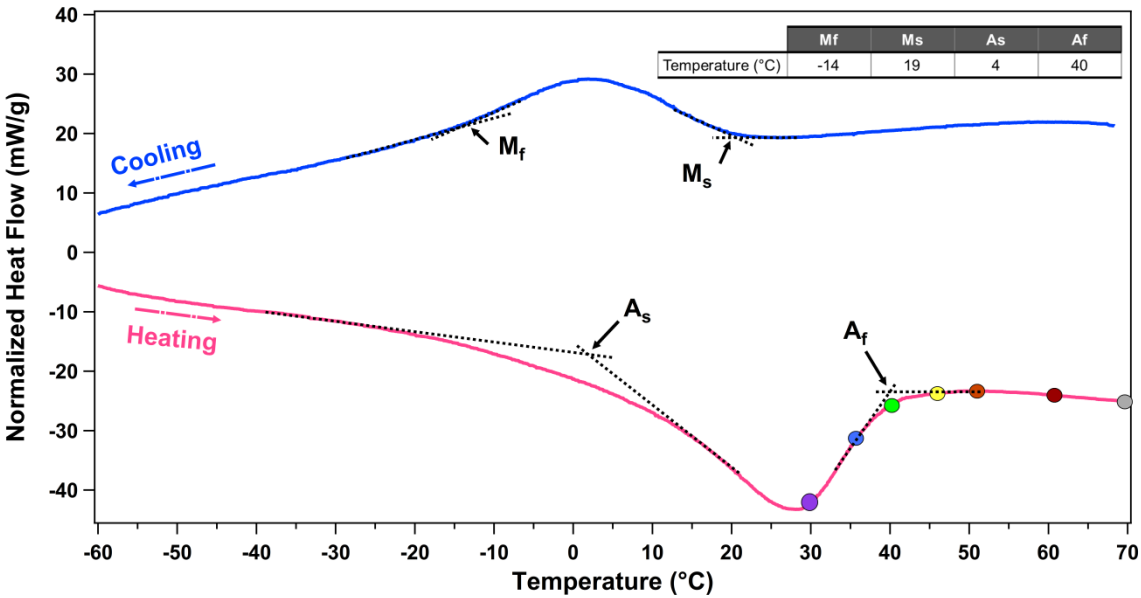
Figure 20. Differential scanning calorimetry thermogram for SPS sintered $Ni_{43}Co_7Mn_{39}Sn_{11}$ material. The inset table summarizes the transformation temperatures determined by intersecting tangent method (denoted by black dashed lines). The colored circles overlaid on the heating curve correlate to the colors and temperatures given in table 6.

Table 6 summarizes the material constants determined or the SPS $Ni_{43}Co_7Mn_{39}Sn_{11}$ powder used in the RUS experiment. The colored cells in the left hand column of the table correlate with the same colored circles overlaid on the heating DSC thermogram of **Figure 20**. Very little change is noted in the material constants across the

temperature range tested. The RMS error, presented in the last column on the right, was consistently less than 0.5% which indicated excellent fit of the peak positions of the sonogram, and indicated good fit between the model and peak position within the spectra.

Table 6. Summary of material properties determined buy RUS on the sintered $Ni_{43}Co_7Mn_{39}Sn_{11}$ material

Temperature (°C)	Bulk Modulus (GPa)	Shear Modulus (GPa)	Young's Modulus (GPa)	Poisson's Ratio	$C_{11,22,33}$ (GPa)	$C_{23,13,12}$ (GPa)	$C_{44,55,66}$ (GPa)	RMS error (%)
30	144.34	52.20	139.75	0.34	213.94	109.54	52.20	0.386
36	145.34	52.15	139.73	0.34	214.87	110.57	52.15	0.346
40	145.73	52.00	139.43	0.34	215.07	111.06	52.00	0.400
45	146.00	51.89	139.18	0.34	215.19	111.41	51.89	0.384
50	145.58	51.88	139.11	0.34	214.75	110.10	51.88	0.378
60	144.58	51.79	138.80	0.34	213.63	110.05	51.79	0.380
70	145.29	51.58	138.36	0.34	214.06	110.91	51.58	0.370

3.4 Discussion

Consolidation of the pure aluminum and $Ni_{43}Co_7Mn_{39}Sn_{11}$ powders at 400°C yielded a composite with a highly porous matrix, yet no diffusion occurred between the two materials (as desired). This meant that controlled growth of a diffusion region between the $Ni_{43}Co_7Mn_{39}Sn_{11}$ and pure aluminum could be achieved with secondary heat treatments, and permitted observation of the diffusional products at different time

intervals. This was important to better understand how the diffusion region grew and developed. As the intended use of these $Ni_{43}Co_7Mn_{39}Sn_{11}$particles focused on embedding them in aluminum based alloys, the evolution of the diffusion products here would lend insight into the expected phases to be observed in the diffusion region between the $Ni_{43}Co_7Mn_{39}Sn_{11}$ particles and the aerospace grade aluminum.

3.4.1 Effect of Consolidation Temperature and Secondary Heat Treatments on the Microstructure of Consolidates

As predicted by the diffusion modeling from DICTRA, atoms from the $Ni_{43}Co_7Mn_{39}Sn_{11}$particle were observed to migrate into the aluminum matrix as demonstrated by the concentration gradient seen in the WDS maps for nickel and manganese of **Figure 13**. Furthermore, the insolubility of tin in aluminum caused tin to diffuse toward the center of the $Ni_{43}Co_7Mn_{39}Sn_{11}$particle, and created a tin rich ring at the boundary of the particle.

3.4.1.1 400°C Consolidated Composite Exposed to Secondary Heat Treatments

Exposing the sample for the consolidation at 400°C to 550°C for 20 minutes, yielded three distinct phases in the outer diffusion region, and two in the inner. Comparison of the atomic percentages of aluminum, nickel, and manganese to the phases present in their ternary phase diagram (600°C) [95] indicated the presence of $NiAl_3$, $Mn_{53.3}Al_{230.8}$ and $Al_{31}Mn_6Ni_2$. These compounds are also among the suggested stable phases by our calculated phase diagram. Further comparison of the binary Ni-Al and Ni-Mn [96, 163]

phases via the concentrations determined by WDS confirmed the presence of $NiAl_3$

(Phase II), as it is also shown as an stable phase in the calculated phase diagram. $MnAl_6$

is yet another likely candidate which was both indicated by the phase-diagram and WDS

results, and given the similarity in atomic sizes between cobalt and manganese, and

noting the comparatively low concentration of cobalt, it was likely the cobalt substituted

for the manganese rather than forming a new phase. Adding the atomic percentage of

cobalt to that of manganese yielded a concentration only 0.5 at.% greater than the

concentration determined for the line compound $Mn_{53.3}Al_{230.8}$. Therefore, we believed

the more likely phase present was $Mn_{53.3}Al_{230.8}$ (Phase I) as stated by the ternary phase

diagram. Converting the molar concentrations of aluminum, manganese, and nickel in

the $Al_{31}Mn_6Ni_2$ compound, to atomic percentages yielded values of 79.50 at.%

aluminum, 15.38 at.% manganese, and 5.13 at.% nickel. It was initially thought Phase III

to be the $Al_{31}Mn_6Ni_2$, but the measured concentrations of nickel were significantly

higher than was expected for the $Al_{31}Mn_6Ni_2$ compound. However, as the $Al_{31}Mn_6Ni_2$ is

a solid solution, it is possible a supersaturated version containing extra nickel was

present and lead to the precipitation of the $NiAl_3$ intermetallic; it is also possible that

Phase III was merely the result of concentration gradients between the Al-Ni and Al-Mn

intermetallics and the resolution of the map was not sufficiently fine to distinguish the

small scale variations, subsequently showing the differences as a new phase. As no

distinct regions with the appropriate concentrations of aluminum, nickel, and manganese

for $Al_{31}Mn_6Ni_2$ solid solution were observed, its presence was not confirmed. However,

given the other intermetallic species, its presence of the ternary solid solution was suggested.

Confirmation of the $NiAl_3$ intermetallic and the suggested presence of $Al_{31}Mn_6Ni_2$ was in agreement with the predictions made by the calculated phase-diagram. The obtained phase-diagram also predicted other intermetallic compounds depending on the Al enrichment in the diffusion zone. The presence of these other compounds was dependent on kinetic factors and, their stability with regard to other predicted phases, and was not confirmed by the WDS-EPMA results.

Phase IV and Phase V of the inner diffusion region presented more difficulty in their identification. As each of the five elements were in Phase IV, different scenarios were considered. As tin and aluminum are insoluble [99], it was not expected that intermetallics containing both tin and aluminum would form; this was confirmed through analysis of the ternary phase diagram for Al-Ni-Sn (25°C) [158] which yielded possible phases as NiAl, Ni_3Sn_4 and elemental Sn (no phase diagram was available for Al-Mn-Sn). Analysis of the Mn-Ni-Sn ternary (400°C) [164] for the measured atomic percentages suggested a three phase region consisting of Ni_3Sn_4 $MnSn_2$ and liquid Sn. Noting the cobalt concentration of this phase was 5 at.%, consideration of the Ni-Mn-Co ternary diagram (25°C) [165] shows a combination of two single phase regions: Ni-Mn solid solution, and a Ni-Mn-Co high temperature phase solid solution. Finally, the binary phase diagrams for Mn-Sn and Ni-Sn [166, 167] both demonstrated solid solutions at 25 at.% tin, forming Mn3Sn and Ni3Sn solid solutions. As no evidence for liquid tin was observed in the microstructure, and both cobalt and aluminum are soluble in manganese

and nickel, we believed that Phase IV was a solid solution of Ni-Mn-Co-Sn-Al, with very slight segregation between the aluminum and tin (aluminum preferring the nickel, and tin preferring the manganese).

Phase V was determined to be a Ni-Mn-Co-Sn solid solution, given the analysis of the appropriate phase diagrams previously stated. The intermetallic Co_3Sn_2, while suggested as a possible phase from the Co-Sn binary given the concentrations, no distinct phases with concentrations of cobalt higher than the parent $Ni_{43}Co_7Mn_{39}Sn_{11}$ were observed. Therefore, it was believed only the solid solution was present. Comparing the identified phases to the phases predicted by the thermodynamic stability analysis showed minor dissimilarity. This is likely due to the non-equilibrium condition of the physical system as is evidenced by the solid solution containing both tin and aluminum. The steep concentration gradients, and short diffusion times, likely provided sufficient driving force to stabilize the observed metastable regions.

Extending the heat treatment time to 60 minutes at 550°C grew the diffusion region larger as compared to the sample exposed for only 20 minutes. In addition to the size, more distinct phases were observed within the inner and outer diffusion regions. In the outer diffusion region, 4 distinct phases were observed (Phases VI-IX), and three phases in the inner diffusion region (Phases X-XII). Comparison to the phase diagrams as above determined that Phase VI and Phase II were likely the same observed phase (Ni_3Al solid solution); Phase VII and Phase I were likely the same observed phase ($Mn_{53.3}Al_{230.8}$); Phase VIII was determined to be $NiAl_3$; Phase IX was determined to be $Mn_{11}Al_{15}$ solid solution; Phase X was determined to be Mn_3Sn_2. Given the relative

concentrations of manganese, and tin, it was likely that the Mn_2Sn solid solution formed at 550°C [166]. Upon cooling the majority of this material then transformed into the Mn_3Sn_2 intermetallic. Noting that the nickel concentration was not insignificant, analysis of the Mn-Sn and Ni-Sn [167] phase diagrams revealed that for 25 at.% Sn, manganese and nickel formed an intermetallic and solid solution, respectively, with identical crystal structures. Therefore we believed the resulting intermetallic was based on the Mn_3Sn_2 crystal structure, but contained notable substitutions by cobalt and nickel. Phase XI was determined to most likely consist of a nickel-manganese-tin solid solution with minor substitutions by cobalt; and finally Phase XII was determined to be very similar to Phase V (nickel-manganese-cobalt solid solution with substitutions by tin). The core $Ni_{43}Co_7Mn_{39}Sn_{11}$ particle demonstrated no change in composition as compared to the nominal composition and the composition of the core $Ni_{43}Co_7Mn_{39}Sn_{11}$ particle after 20 minutes at 550°C.

A number of important points should be made about this system. First, despite the calculated diffusivity coefficient of manganese exhibiting a value three orders of magnitude smaller than the values for cobalt and nickel, manganese had a significant impact on the diffusional products of the system. Second, alternative approaches such as Density Functional theory for studying the mechanism of diffusion in the Huseler structure should be considered in future modeling. Third, the interaction between the five elements of the system provided more complex thermodynamic states and kinetic mechanisms than was expected, and emphasized that the simple assumptions for diffusion through aluminum were largely inaccurate. Fourth, given the diffusivity for tin

being the highest of the system, intermetallics between it, cobalt, manganese, or nickel were only observed for the extended time at 550°C due to stability of Mn or Ni based compounds comparing to that of Sn compounds. And finally, it is worthwhile to point out that the thermodynamic state of the observed quaternary solid-solutions are not yet assessed.

Noting the differences between the calculated phases determined through the ThermoCalc calculations and those determined from the WDS maps, indicated that the $Ni_{43}Co_7Mn_{39}Sn_{11}$-Al system had not achieved equilibrium after 60 minutes at 550°C, and that further times at elevated temperature would likely continue to evolve the system.

3.4.1.2 560°C Consolidated Composite compared to 400°C Consolidated + 550°C

for 60 minutes

Comparing the BSE images of **Figure 8** to that of **Figure 18** demonstrated significant similarities in the diffusion regions. In the outer diffusion region of both, at least two distinct phases were observed (as seen by contrast differences), and closer inspection of the BSE image in **Figure 18** showed almost identical features as seen in the BSE image of **Figure 14**. Further comparison of the EDS maps shown in **Figure 12** to the WDS maps in **Figure 18** demonstrated remarkably similar segregation of the elements, including the nickel depleted ring at the boundary of the inner and outer diffusion regions. The similarities in the BSE images, the EDS maps and WDS maps, and the 10°C difference in consolidation temperature (560°C) and secondary heat treatment

temperature (550°C) for each compact respectively, we believe the diffusion regions observed in both composites to be reasonably similar. While the different phase fractions and sizes of the intermetallics would vary, we expected the diffusion regions to possess largely similar mechanical responses. Therefore, it was believed the mechanical properties determined through nanoindentation would be representative of the mechanical properties of the diffusion zone created by exposing the specimen from the 400°C consolidated composite to 550°C for 60 minutes.

3.4.2 Micro-mechanical Properties of $Ni_{43}Co_7Mn_{39}Sn_{11}$ and the Diffusion Region

Comparison of the material properties determined through nanoindentation between the machines showed that the Hysitron over estimated both the modulus and hardness of the diffusion region and $Ni_{43}Co_7Mn_{39}Sn_{11}$ particle. This was likely due to the depth to which the indents penetrated for the indents made in the Hysitron. While the iMicro demonstrated that a depth of 150 nm yielded a stable material response within the $Ni_{43}Co_7Mn_{39}Sn_{11}$particle as seen by the modulus versus depth plot (with only three Hysitorn indents that did not meet that criteria), only seven indents surpassed the depth of 200 nm. It seemed reasonable then the shallower indents would overestimate the modulus and hardness of the material.

The same trend was observed for the indents taken in the diffusion region. With a minimum depth of 125 nm being sufficient for stable material response, as seen in the modulus versus depth plot for the diffusion region indents of the iMicro, eight indents were insufficiently deep and only ten surpassed 160 nm (less than half of the maximum

depth for the iMicro). Then as before it was sensible that the shallower indents made with the Hysitron overestimated the material properties. Despite these differences, however, reasonable agreement was achieved between the two different methods.

3.4.3 Material Properties of Sintered $Ni_{43}Co_7Mn_{39}Sn_{11}$ via RUS

The transformation temperatures of the sintered $Ni_{43}Co_7Mn_{39}Sn_{11}$ powder through analysis of thermograms obtained from the DSC demonstrated significantly lower transformation temperatures than that reported in literature for powders of the same composition. Kainuma *et al* report 36°C, -23°C, 27°C, and 62°C for M_s M_f, A_s, A_f, respectively, and Monroe *et al* report 42°C, 26°C, 46°C, 60°C for M_s M_f, A_s, A_f, respectively (versus 19°C, -14°C, 4°C, and 40°C for M_s M_f, A_s, A_f, respectively, in this work). While differences in transformation temperature reported here versus literature are significant, care must be made before making direct comparisons.

The transformation temperatures Ito *et al* reports were determined from thermo-magnetization plots at 500 Oe (0.05T). While this is commonly acceptable as comparable to zero magnetic field, the specimens for those type of tests are typically less than one gram of material; furthermore, Kainuma *et al* show DSC thermograms with significantly higher temperatures than those determine using the thermo-magnetization plots [73]. They addressed this discrepancy in their data by stating the sample for DSC was significantly larger containing larger columnar grains that spanned the specimen's microstructure, whereas the samples for magnetization experiments only contain a few grains. As grain boundaries restrict the transformation from austenite to martensite,

90

suppressing transformation temperatures due to the stored elastic energy the transformation causes, specimens with larger grains and fewer grain boundaries would express higher transformation temperatures [68, 168, 169].

Direct comparison to Monroe *et al*'s data proved difficult for the same reasons. In their work, they manufacture a highly porous metallic foam using the same composition and particle size of $Ni_{43}Co_7Mn_{39}Sn_{11}$ as the present work. Due to the large pores in the microstructure creating significant amounts of free surface to relieve the elastic energy caused by martensitic transformation, they report significantly higher transformation temperatures than the present work as well (the authors would like to note that both Ito *et al* and Monroe *et al* cited the same papers as here to explain the deviations from expected materials response). Therefore, it is not possible to make direct comparisons to the stated transformation temperatures given in literature. Comparison to alloys of similar composition is further complicated by the well-known effect of composition on transformation temperatures and transformation ranges [105, 170-172].

Given the fact the microstructures seen in the micrographs of **Figure 19** did not reveal any inhomogeneity of composition or second phases (as variations in contrast of the BSE images would be expected), we believed the discrepancy in transformation temperatures arose for the same causes as given by Ito *et al* and Monroe *et al*, but for the opposite reason. Where they had large free surfaces to relieve the elastic stress induced by transformation, the high number of grain boundaries and large number of grains within our test specimen (given the starting particle size) suppressed the transformation from austenite to martensite and required further undercooling for a high driving force to

overcome the barriers to transformation. The stored elastic stress would then encourage

transformation back into austenite at a temperature far lower than anticipated (what was

observed here). Therefore, we believed the sintered $Ni_{43}Co_7Mn_{39}Sn_{11}$powder acted as a

good representation for the expected mechanical properties of the individual

$Ni_{43}Co_7Mn_{39}Sn_{11}$powder particles.

The modulus values determined from the RUS analysis were in reasonable

agreement with the values obtained in the mechanical nanoindentation tests. The

discrepancy was likely due to the grainsize of the specimens tested. Review of the

micrograph of the starting powders and embedded particles showed each particle

typically containing 1-4 grains. As each particle then acts as a single or oligo-crystalline

material, orientation has a significant effect on mechanical properties. As the individual

particles were not large enough to acquire a sufficient sample size of indents, multiple

particles needed to be tested, sampling the various possible orientations each

$Ni_{43}Co_7Mn_{39}Sn_{11}$particle obtained. As polycrystalline FCC based materials (like

$Ni_{43}Co_7Mn_{39}Sn_{11}$) generally demonstrate mechanical properties closer to the <110>

orientation, slightly higher or lower material properties would be expected until the

sample population size (number of indents) achieved a minimum value.

3.5 Conclusions

In summary, we predicted the diffusional products between $Ni_{43}Co_7Mn_{39}Sn_{11}$ and pure

aluminum through the use of a thermodynamic model developed in the Thermo-Calc

software, and confirmed their existence through quantitative elemental mapping. The

diffusion region was found to contain a complex array of aluminum-nickel and aluminum-manganese intermetallics, aluminum-nickel-manganese solid solution, manganese-tin intermetallics, and nickel-manganese-tin solid solutions. The mechanical properties of the both the diffusion region and the $Ni_{43}Co_7Mn_{39}Sn_{11}$ particles were investigated; the diffusion region was determined to have a modulus and hardness of 163 $\pm$ 5 and 10.0 $\pm$ 0.3, respectively, while the $Ni_{43}Co_7Mn_{39}Sn_{11}$ particles possessed 127 $\pm$ 6 and 4.5 $\pm$ 0.4 for modulus and hardness, respectively. The modulus of the $Ni_{43}Co_7Mn_{39}Sn_{11}$ material was confirmed through the use of resonant ultrasonic spectroscopy, which also yielded elastic constants, bulk and shear moduli, and Poisson's ration for the polycrystalline $Ni_{43}Co_7Mn_{39}Sn_{11}$ material.

Here the fourth benchmark for successful integration of magnetic SMAs as sensory particles was achieved. The resulting diffusion products between the magnetic SMA particle and the host matrix were identified and characterized.

Based on these results, use of the $Ni_{43}Co_7Mn_{39}Sn_{11}$ as a sensory material will require tailored processing conditions to ensure sufficient control over the growth of the diffusion region between the $Ni_{43}Co_7Mn_{39}Sn_{11}$ magnetic SMA and aluminum matrix material.

4. OPTIMIZING ALUMINUM 7075 MATRIX CONSOLIDATION FOR COMPOSITE FABRICATION

4.1 Introduction

4.1.1 Motivation

In the previous section we demonstrated the diffusion products that occur between $Ni_{43}Co_7Mn_{39}Sn_{11}$ consisted of multiphase regions comprised solid solutions and intermetallics. Due to their brittle nature, uncontrolled growth lead to incompatibility between the ductile matrix and the brittle diffusion region (as seen in section two), and a subsequent reduction in the material properties of the composite as compared to aluminum consolidated similarly. However, we also confirmed the hypothesis proposed by Leser et al [84] that a diffusion region was necessary to ensure stress transfer from the matrix to SMA material. Finally, we demonstrated the need for a matrix that demonstrated similar compatibility with the magnetic SMA material during deformation, that would tolerate the higher stresses needed to induce martensitic transformation in the magnetic SMA material through the diffusion region. These observations provided key insight into the what processing parameters required exploration and determination to yield a final material sufficiently capable of demonstrating a change in magnetization when exposed to plastic deformation.

As the previous experiments revealed that matrix possessing greater deformation compatibility with the magnetic SMA, it was decided to transition from pure aluminum to an aluminum alloy, specifically aluminum 7075. This particular alloy is commonly

used in critical structural aerospace components, where fatigue cracking is particularly dangerous early detection is most beneficial. Additionally, naturally occurring aluminum-iron intermetallic second phases act as fatigue crack initiation sites within this alloy [173], further supporting the usage of this alloy in composite manufacturing experiments.

Exploratory experiments revealed consolidation of the aluminum 7075-$Ni_{43}Co_7Mn_{39}Sn_{11}$ powder mixture at temperatures exceeding 450°C yielded uncontrolled diffusion between the magnetic SMA and the aluminum 7075 matrix. As this temperature is relatively low for metallic powder consolidations [174], optimum processing of the matrix must first be determined to ensure high quality manufacturing of the subsequent composite materials. Ideally, processing conditions that yield a compact manufactured solely from the aluminum 7075 powders will achieve the following requirements:

1. No pre-compaction or greenbody processing may be used to manufacture the final compact.

2. Consolidation of the powder will occur at sufficiently high temperatures to promote densification and interparticle bonding, but not exceeding 450°C.

3. Sintered compacts must demonstrate material properties (specifically Young's modulus, yield stress, ultimate tensile strength, and elongation at failure) similar to those of commercially available plate materials.

95

The following section will discuss aluminum alloy powders and the issues present in their consolidation; common methods for their consolidation and how SPS provides an excellent means for powder consolidation given our processing requirements; and finally, propose two methods for powder consolidation to achieve the three requirements listed above in the final consolidate.

4.1.2 Background

4.1.2.1 Aluminum Powder and Its Consolidation

Aerospace grade aluminum alloy powders are typically created through atomization of a melt. Given aluminum's high reactivity with oxygen, inert gasses are generally used for this process, and if the stream of gas is pulsed ultrasonically, then powders are produced on the order of 59 μm with few satellites on the particles that other common methods [174]. If the aluminum alloy powder is to be handled safely in non-inert environments, the surface must be stabilized through the formation of an oxide layer; this layer can be either amorphous or crystalline (forming γ-Al_2O_3), depending on the orientation of the crystallites within the powder particle [175-177]. As the stable form of amorphous state of the oxide can only exist up to 7 nm, depending on orientation, inert gas atomized powders are more likely to possess amorphous oxide shells [176]. Crystallized alumina is preferred to the amorphous state, as the crystallized state possesses a 20% higher density than its amorphous counterpart, and crystallization begins in the temperature range of 300-350°C [177, 178]. Because of this, transformation of an amorphous oxide layer to crystalline likely causes rupture of the oxide (assuming no oxygen is present to

96

heal the oxide layer), permitting metal to metal contact of the powder particles for solid state diffusion [179]. As such, the oxide layer must be crystallized and disrupted, mechanically or chemically, to ensure effective sintering of the powder.

Commonly, two methods are used to ensure oxide rupture on the particle surfaces. The first is compaction of the particles into a green body form. Compaction of the powder fractures the oxide surface at the junctions of the particles forming metal-to-metal contacts through which diffusion can occur [180-182]. Despite its demonstrated effectiveness, this processing method is not feasible; compaction of the aluminum 7075-$Ni_{43}Co_7Mn_{39}Sn_{11}$ is likely to induce martensitic transformation of the magnetic SMA particles, negatively affecting the sintering of the powders.

The second method to promote oxide rupture on the particle surfaces is to incorporate a small amount of magnesium. Presence of this element acts as a reducing agent to rupture the oxide layer of the particles and as an oxygen getter significantly lowering the oxygen concentration in the local sintering atmosphere [183-186]. While the aluminum 7075 alloy can contain up to 2.9% Mg, this is required to form η' precipitates along grain boundaries granting the alloy's superior strength [187-192]. Further magnesium cannot be added, as it is unclear how it will affect the magnetic SMA and the sintering process for the powder mixture. Therefore, common processing methods are not able to satisfy the consolidation requirements set forth in Section 4.1.1 and alternative methods must be sought out.

4.1.2.2 Spark Plasma Sintering

Spark plasma sintering demonstrates the ability to shorten times required for powder consolidation and a reduction in temperature required to do so [179]. Similar in processing to a hot press, the sample is heated in the die through the high-intensity current passing through the specimen rather than being heated by a furnace. The current is commonly applied in pulses (direct or alternating current), and is said to "clean" the particle surfaces and increase neck formation [193]. However, the exact role pulsing current plays in the sintering process, and the limited information on this subject is contradictory requiring further work [179, 194]. This gap in information provides an excellent opportunity for the current work. As the restrictions on upper sintering temperature and pre-compaction of the starting powders do not permit the application of common processing methods, modification of the on:off DC pulses used in spark plasma sintering might provide the required control over sintering desired for this system. Additionally, it will provide additional data to aid in understanding the role pulsed current plays in the sintering of conductive powders.

4.1.3 Proposed Areas of Investigation for Al7075 Powder Consolidation

Review of the (limited) literature on consolidation of aluminum 7075 powders revealed on:off pulse length ratios ranging from 30:5 to 100:100 ms [195-198]. As direct comparison is difficult between these times, we propose to hold the ratio of on:off pulse the same over different length scales. Three ratios of on:off pulse lengths (4.5, 6, 10) will be explored at shorter and longer intervals through the consolidation of aluminum 7075

powders. The mechanical responses of the sintered compacts will be compared to commercially available aluminum 7075 plate material to determine whether or not sintering produced satisfactory results. To ensure differences in material responses are due to the different pulse lengths explored, consolidation will occur at $0.95T_m$ to better observe the effectiveness the pulse lengths demonstrate on oxide rupture. Successful consolidations will then be tested at lower temperature within the confines of sintering the aluminum 7075 with $Ni_{43}Co_7Mn_{39}Sn_{11}$.

In addition to exploring the effect of pulse length on powder consolidation, the effect of cold work of the aluminum 7075 powder via ball milling, and the effect of off-gassing the powder inside the spark plasma system will be investigated. It is hoped that these methods will provide an alternative to created sintered compacts with satisfactory material properties within boundaries of the processing restrictions set forth in Section 4.1.1.

4.2 Experimental Methods

4.2.1 Starting Materials and Powder Consolidation

Aluminum 7075-T651 plate material (152 x 305 x 25 mm; 12 x 6 x 1 in) was purchased from Midwest Steel and Aluminum (Lot#: 70633, Cast#: 01/0062572/4). Gas atomized aluminum 7075 powder, sieved to size range of 15-53 μm, with an average particle size of 17 μm was purchased from Valimet (Item: AA7075, Batch#: 12-3001S). **Table 7** summarizes the composition for the aluminum 7075-T651 plate, and the aluminum 7075 powder as given by the certification sheets obtained from manufacturers; they fall within

the acceptable ranges as given by ASTM Standards and B918/B918M-17a [199]. **Figure 21** displays the particles size range for the aluminum 7075 powder.
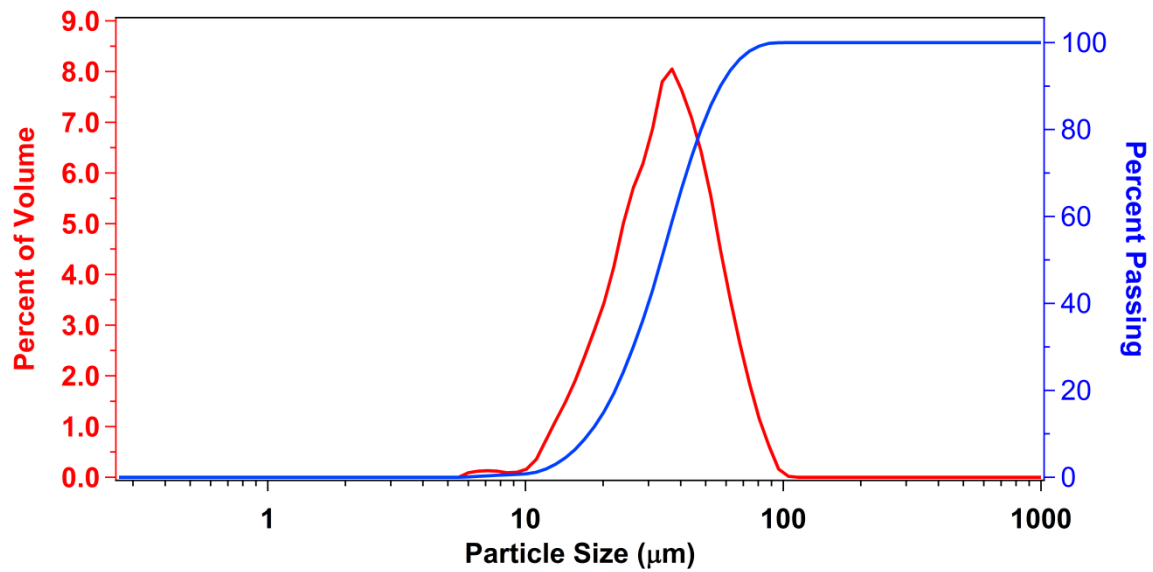
Figure 21. The as received particle size distribution for the Al7075 powder purchased from Valimet. The right axis shows the percentage of the powder that passed screening for a particular size (bottom axis), while the left shows the distribution of particles sizes as a percentage of the volume of powder tested (particle size analysis was performed using a Microtrac-S3000 as stated by the manufacturers certification sheets).

Table 7. Summary of the chemical composition of the aluminum 7075 plate and starting powder materials as compared to the ASTM Standards B918/B918M-17a [199].

Type	Alloy		Si	Fe	Cu (min-max)	Mn	Mg (min-max)	Cr (min-max)	Zn (min-max)	Ti	Other Each	Other Total	Al
Plate	Aluminum 7075-T651	Nominal*	0.40	0.50	1.2-2.0	0.3	2.1-2.9	0.18-0.28	5.1-6.1	0.2	0.05	0.15	Bal
		Actual** (OES)	0.09	0.13	1.4	0.05	2.5	0.19	5.6	0.03	0.02	0.03	Bal
Powder	Aluminum 7075	Actual** (ICP-OES)	0.13	0.17	1.54	0.02	2.25	0.19	5.40	<0.01	<0.05	<0.15	Bal

Ten compacts were manufactured from the powder using spark plasma sintering in a high vacuum environment in a 40 mm graphite die. Sufficient powder was used to yield a specimen with final thickness of 8 mm. For each consolidation process, the following sintering procedure was repeated: powder was poured into the graphite die in open atmosphere (without compaction to form a green body), the die was placed in the SPS and a stress of 5 MPa was applied to the powder (the lowest stress the SPS was able to register). High vacuum atmosphere was then applied to the SPS chamber (10^{-5} Torr). The die and powder were heated with pulsed DC current (20V, 200A; required pulse length on/off ratio) at a rate of 100°C/min to the required sintering temperature, stress was increased on the die at the required rate to the sintering pressure, and was maintained until the ram of the SPS registered zero change in position for 60 seconds. **Table 8** summarizes the main processing parameters used during each sintering process.

Table 8. Processing details for the compacts manufactured through consolidation of the aluminum 7075 powder.

Processing	Detail	Heating Rate	Max Temp	Loading Rate	Max Stress
Varying Pulse Length on/off	20/2 ms on/off	100°C/min	530°C	20 MPa/min	45 MPa
	30/5 ms on/off		530°C	25 MPa/min	
	36/8 ms on/off		530°C	20 MPa/min	
	50/5 ms on/off		530°C	25 MPa/min	
	60/10 ms on/off		530°C	20 MPa/min	
	72/16 ms on/off		530°C	25 MPa/min	
Ball Mill and Off Gassing	Ball Mill		530°C	20 MPa/min	
	Off-gas		430°C	25 MPa/min	100 MPa
	Off-gas		530°C	20 MPa/min	45 MPa
	Ball Mill & Off Gas		430°C	25 MPa/min	100 MPa

For specimens denoted with "off-gas" in the name, an additional step was added to the manufacturing process. Before heating the powder to the final consolidation temperature after application of 5 MPa, it was first heated with pulsed DC current (20V, 200A; 20/2 ms on/off) at a rate of 100°C/min to 400°C and held there for one hour before continuing with the consolidation process as given above.

For the specimens manufactured from ball milled Al7075 powder, the following procedure was applied to the as received Al7075 before pouring into the SPS die. Sufficient powder to yield a final compact with a thickness of 8 mm was charged into a polypropylene container along with stainless steel balls in a 15:1 (ball:powder) by weight (approximately 200 – 6.35 mm diameter and 10 – 9.53 mm diameter balls). The container was sealed under the inert ultra-high purity atmosphere of a glovebox, using electrical tape to seal the seam of the screw-on lid of the polypropylene container. The container was then loaded into the drum of a low energy ball mill (open atmosphere), lined with insulation to fill the extra space, and subsequently low-energy ball milled for 10 hours at 100 rpm. The vial was checked every 2-4 hours for sign of reaction (odor, excessive heat, significant discoloration of the polypropylene container). After completing the 10 hour ball milling process, the polypropylene container was removed from the ball milling drum and transferred back into the glovebox, where the stainless steel balls were extracted via a sieve, and the powder was reclaimed and stored in a glass vial. A small portion was reserved to determine reactivity with open atmosphere, and ensure it was safe for handling while being added to the graphite die of the SPS.

4.2.2 Specimen Fabrication and Mechanical Tensile Testing

Small dog-bone-shaped tension samples with a gauge section of 1.5 mm $\times$ 3 mm $\times$ 8 mm were cut from the aluminum 7075-T651 plate material in the long transvers orientation as dictated by ASTM Standard B557M-15 [200], and from the compacts listed in Table 2, using wire electrical-discharge machining (EDM). Machining residue was not removed from the specimens before heat treatment or testing in an effort to maintain as similar sample geometries as possible to ensure ease of comparison between sample sets. Mechanical experiments were conducted on an MTS 810 servohydraulic test frame (same as previously stated) and an extensometer, directly attached to the gauge section of the samples, with the help of ceramic extension rods, was used to record the axial strain. Specimens were loaded at a strain rate of $4.75 \times 10^{-4}(s^{-1})$ until they fractured. **Figure 22** gives a schematic of where the tensile specimens were taken from within the consolidated powder compacts and the plate material.
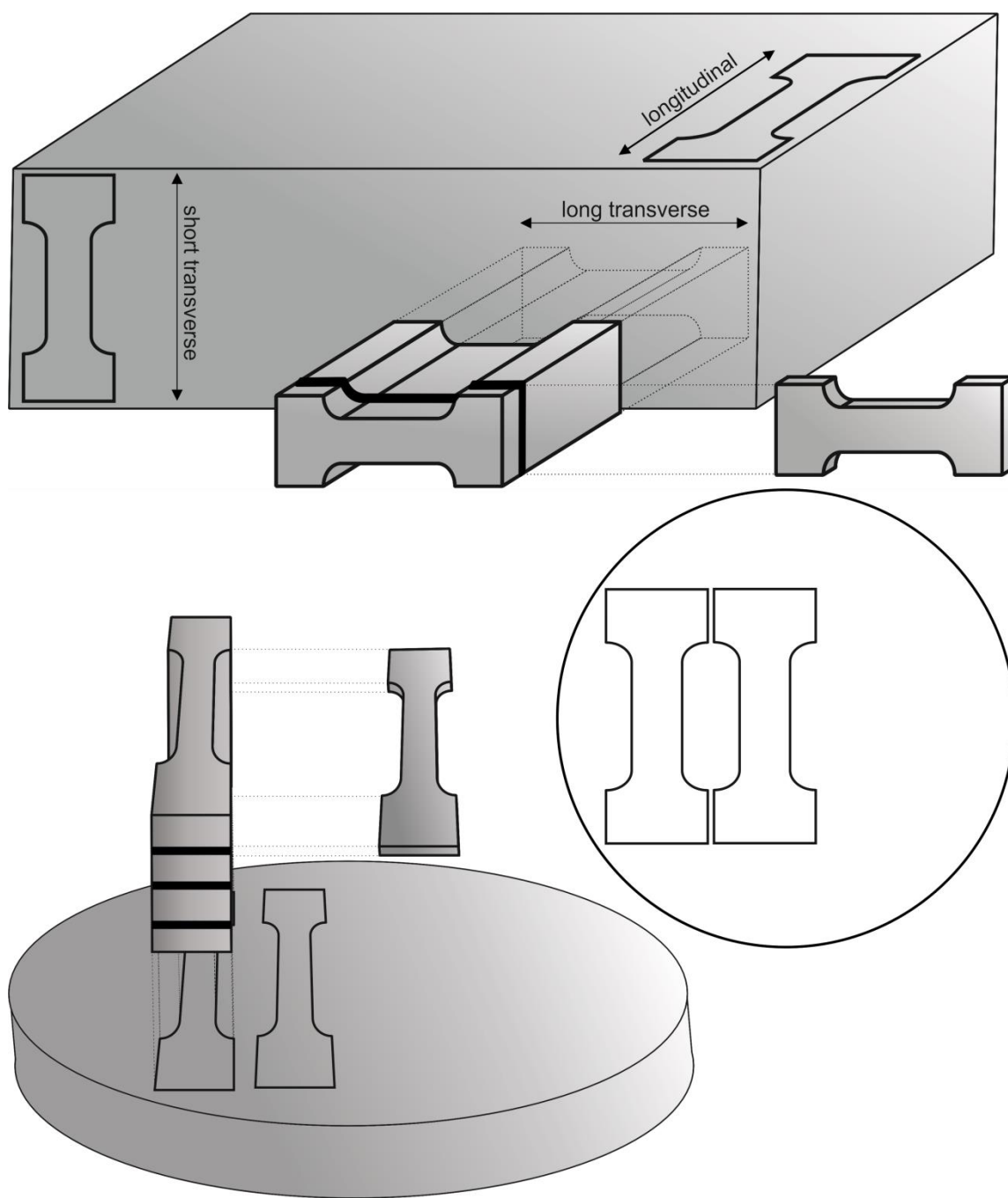
Figure 22. Schematic depicting tensile sample location and orientation for specimens cut from the commercially available plate material, and the round, sintered powder compacts.

All specimens were wrapped in tantalum foil, sealed in a quartz tube under inert ultra-high purity argon atmosphere, heat treated for 60 minutes between 485-490°C [114], and quenched in room temperature water (ensuring to fracture the quartz tube as contact was made with the water). As Al7075 is well known to naturally age in the solution heat treated state at room temperature [114], specimens were heat treated in 3 groups of six specimens, testing began within 15 minutes of quenching, and all specimens from each condition were tested within 120 minutes. Specimens not currently undergoing testing were maintained at ~0°C to halt/slow the aging process. Given the number of specimens tested, it was not possible to heat treat and age all specimens simultaneously to the T6/T651 condition, ensuring uniform heat treating history; therefore, the solution heat treated state was chosen for testing as the expected time for aging is ~54 hours [114]. We were certain that all specimens within a group could be tested within 3 hours (3.7% of the expected aging time), which we believed permitted a more accurate comparison of material responses given the different processing parameters.

4.2.3 Microstructural Characterization and Fracture Surface Observation

A small amount of the as received Al7075 powder was mounted to adhesive carbon tape for imaging with an electron microscope.

Small specimens were cut from each SPS sintered compact using a diamond saw rotating at a speed of 125 rpm. These, as well as another small portion of the as received powder, were mounted in epoxy and polished and mechanically polished using various

steps from 600 grit silicon carbide, to 0.25 μm diamond suspension at a platen speed ranging from 100-150 rpm. The mounted specimens were then vibratory polished in solution of 0.05 μm colloidal silica for 12 hours. A final polish on a polishing media felt cloth and DI water was used to remove polishing media still adhered to the surface of the specimens. As it was difficult to achieve a high quality polish for SEM imaging on the specimens directly after solution heat treatment, only specimens from the as consolidated compacts were for microstructural observation. Given the well-known processing conditions for Al7075 to achieve a solution heat treated condition, we believed it satisfactory to only image the as consolidated state. Micrographs were taken using the same electron microscope as stated in section one.

Fractured tensile specimens from selected specimens within each testing condition were mounted to adhesive carbon tape for imaging with an electron microscope.

4.3 Results

4.3.1 Starting Aluminum 7075 Powders

Figure 23 displays the morphology and microstructure of the as received Al7075 powder. Overall, the general shape of the powder was a mixture of highly spherical and globule like particles. Closer inspection of the surface revealed small protrusions and a rough exterior. Observation of the internal microstructure demonstrated a highly dendritic structure in all observed particles, in excellent agreement with the microstructures observed by Rokni *et al* [201].

107
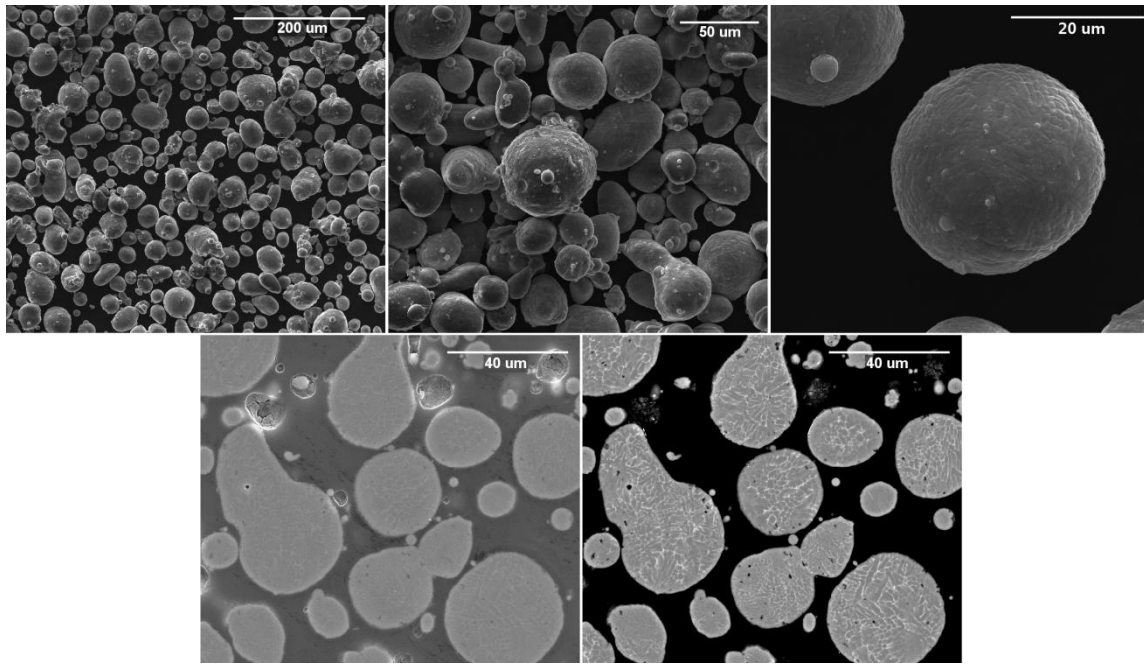
Figure 23. Secondary and back scatter electron micrographs of the starting Al7075 powder. The particle showed a highly spherical geometry and a dendritic, phase separated microstructure.

Figure 24 shows the as received Al7075 powder after 10 hours of ball milling. The general size of the particles remained similar to that of the starting powder, with a slight preferences for the lower particles sizes. The general shape transitioned from highly spherical and globule, to flatter edges and more cubic shapes. The presence of flatter faces and lack of flakes indicated the powder had been cold worked by the ball milling, however significant amounts of grinding had not taken place (as was desired).
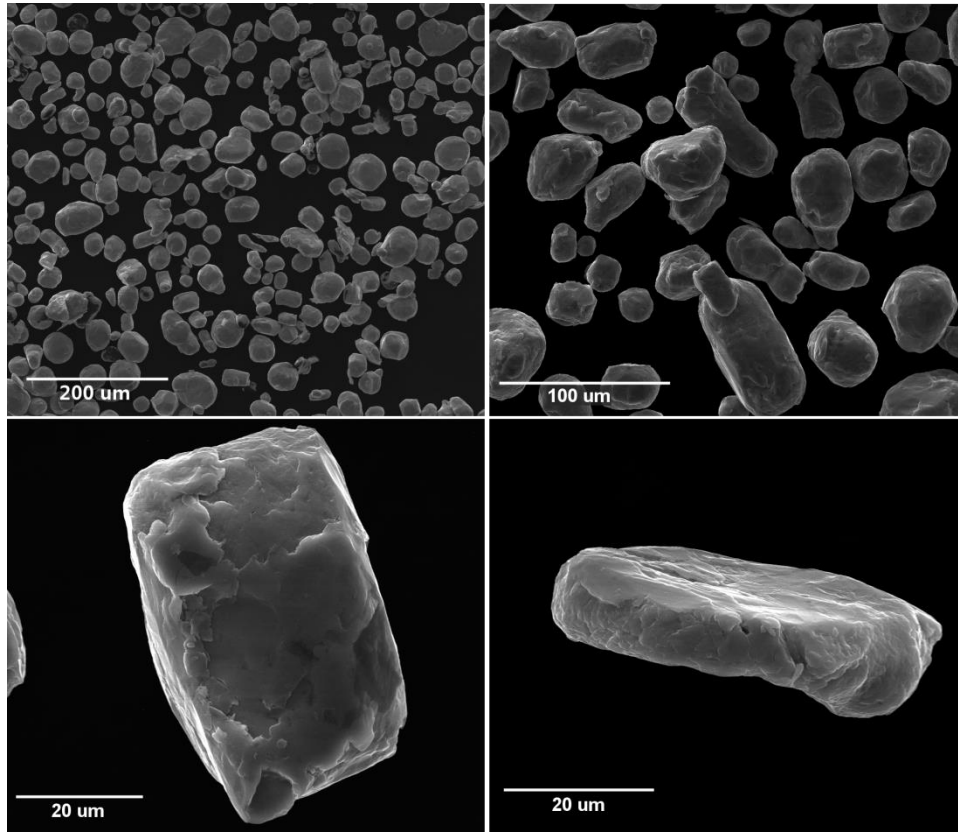
Figure 24. Secondary electron micrograph of the aluminum 7075 aluminum powder after ball milling for 10 hours. Note the flatter faces, and more rectangular geometries.

4.3.2 Sintered Aluminum 7075 Powder Compacts

Figure 25 shows the general processing methods employed for fabrication of the SPS compacts. Only the processing data for varied pulse length (a) (50/5 ms on/off), and off gassing (b) (off gassed 1 hour, 400°C) are displayed as representatives of the two different processing procedures (with and without off-gassing). The beginning of the heating curve in (a) shows a slight deviation from the 100°C.min^{-1} parameter initially set, but resumed the desired rate after the compact reached 80°C. A slight overshoot was observed once the desired processing temperature of 530°C was achieved, and stabilized

within 60 seconds. A two order of magnitude change in the vacuum level was also observed during the heating portion, and indicated off-gassing and desorption of the surface contaminants from the aluminum 7075 powder. The vacuum level began to decrease 270 seconds after initial heating began. A similar response was observed in the specimens that were off-gassed before application of stress (b). Initial heating of the powder revealed no deviation from the desired $100°C.min^{-1}$ parameter initially set, but significant change in vacuum level was observed as seen in (a). Vacuum pressure began to decrease 220 seconds after initial heating. Temperature maintained a steady set point during the initial hold for off-gassing, and only a slight increase in vacuum pressure was observed for the secondary heating for consolidation. This may have been due to small volumes of gas caught in the tortuous internal paths of the powders being forcibly ejected as the material was sintered into a compact.
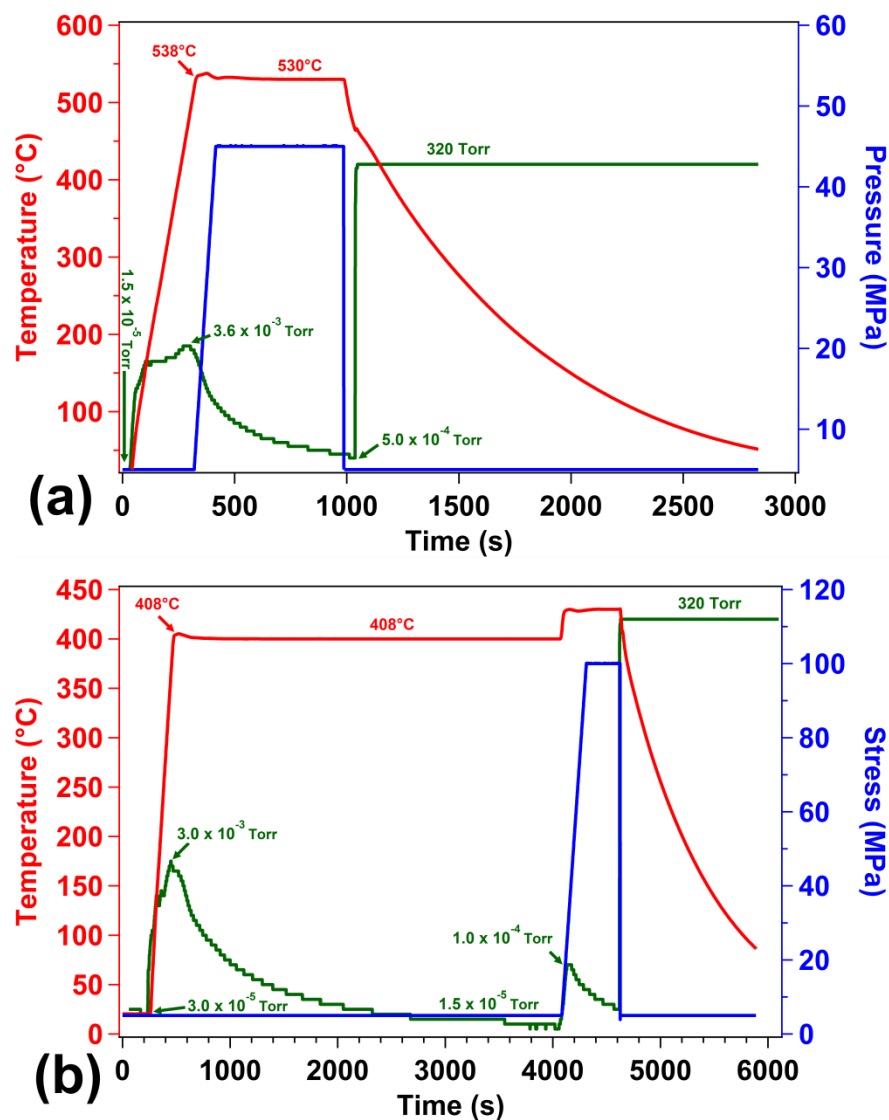
Figure 25. Processing temperatures, pressures, and vacuum levels for aluminum 7075 powders consolidated by various processing conditions. The temperature, pressure, and vacuum as a function of time in (a) are representative of the sintered compacts manufactured by varying pulse length and for the ball milled sample consolidated at 530°C. The same parameters observed in (b) are for specimens consolidated using the off-gassing parameter during processing.

111

4.3.3 Mechanical Tensile Response of Aluminum 7075 Plate and Sintered Powder Compacts

Figure 26 displays the stress strain response of the Al7075 plate material in the –T651 and –W heat treated conditions (peak aged and solution heat treated, respectively). All six specimens for the –T651 conditions demonstrated highly uniform yield stress, ultimate tensile strength, and elongation to failure with yields stress and UTS values that exceed the minimum threshold as stated by ASTM Standard B557-15 [200]. The six specimens tested in the –W condition demonstrated increasing yield stress and ultimate tensile strength with increasing time. However the elongation to failure was observed to be highly uniform as was seen in the –T651 condition. Additionally, serrations and instabilities in the stress-strain response of the –W condition were noted. The onset strain of the serrations and instabilities also increased with time.
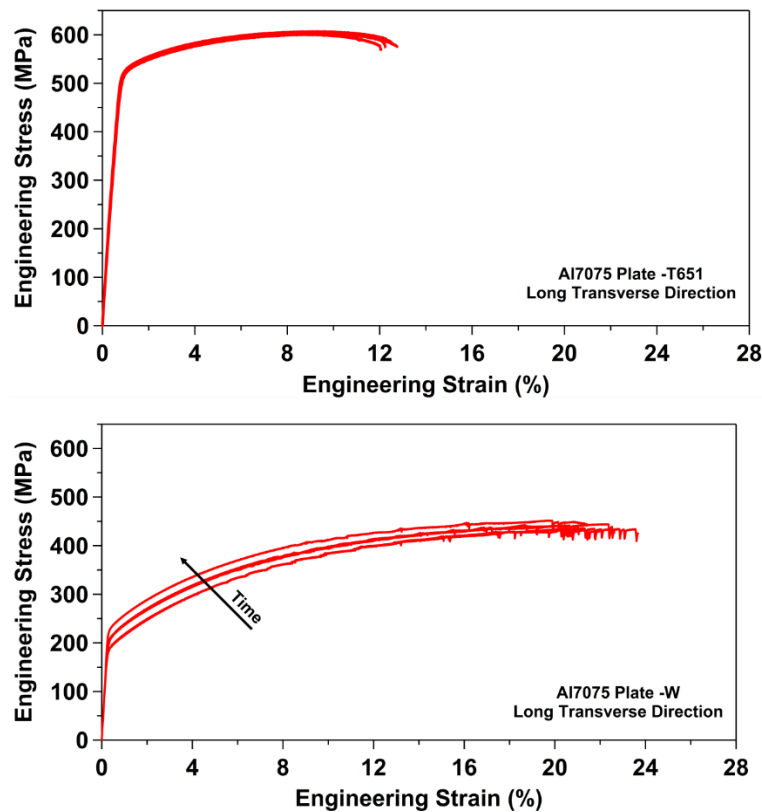
Figure 26. Engineering stress-strain response for the commercially available aluminum 7075 plate in the –T651 and –W tempers.

Figure 27 exhibits the stress strain response for the compacts manufactured by varying the pulse length on/off lengths. All materials were tested in the –W (solution heat treated) condition. All specimens displayed increasing yield stresses and ultimate tensile strengths with increasing time. For the specimens that were able to achieve greater than 12% engineering strain, instabilities in the shape of "fins" were noted as well. Six specimens were tested in each condition to verify material properties, except in the case of the 30/5 ms on/off pulse length test where only five specimens are reported. Improper extensometer placement did not leave sufficient space for the elongation the

specimen experienced, and full strain to failure was not acquired. Therefore, the data of the specimen is not reported, but the value of its yield stress was incorporated into the calculations for the mean yield stress of the sample set.
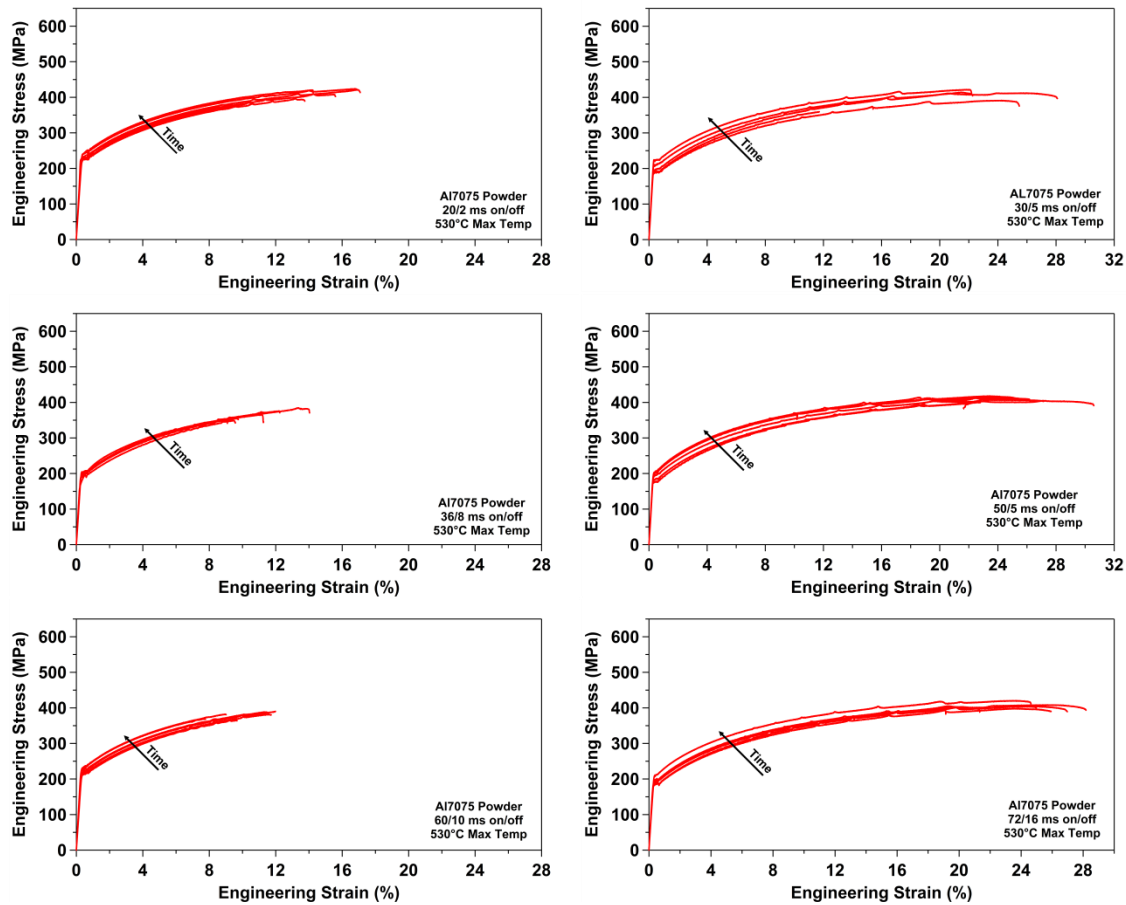
Figure 27. Engineering stress-strain response for the aluminum 7075 powder sintered at 530°C under varying pulse length. All specimens were in the solution heat treated condition, and increasing time is marked by the black arrow. Six specimens from each condition were tested to confirm material properties, except for the 30/5 ms on/off condition in which five specimens were tested. Note the x-axis for 30/5 and 72/16 ms extends to 32% engineering strain.

Figure 28 displays the stress strain response of the off gassed and ball milled specimens in the –W condition. As with the other materials tested, increases in ultimate tensile strength and yield stress were observed for increasing time at room temperature. Fin-like serrations were observed on all specimens that achieved a strain of 8% or greater, except those tested from the sintered compact manufactured using the ball milled powder and sintered at 530°C. Mechanical properties for all tested tensile specimens are summarized in **Table 9**.
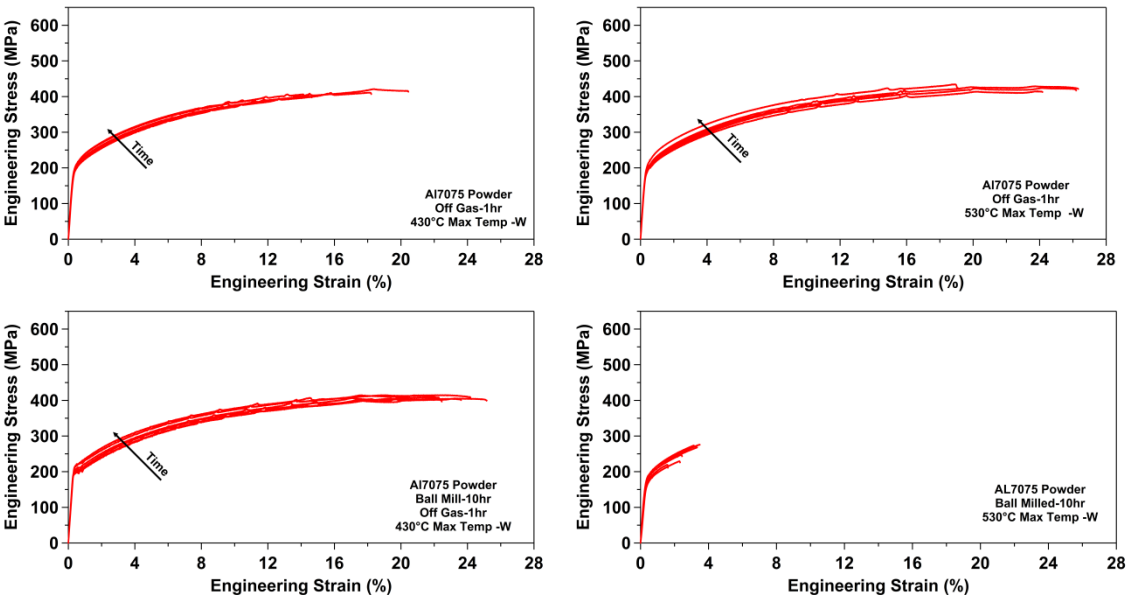
Figure 28. The tensile mechanical responses of the off-gassed, pre ball-milled, and pre ball-milled and off-gassed Al7075 powder. Each consolidation used the 20/2 ms on/off pulse length to heat to the desired temperatures. Six specimens from each case were tested to confirm material response.

Table 9. Summary of the mechanical tensile properties of the commercially available plate material (-T651 and -W heat treated conditions) [200], and the compacts manufactured using SPS (-W heat treated condition). Values given are the means obtained from averaging the data for the six specimens in each fabrication method. Error is stated as plus/minus one standard deviation for the same six specimens. The values for "Plate" marked with a star (*) indicate the values reported on the specification sheet obtained from the manufacturer.

	Fabrication	Temper	Tested	Young's Modulus	σ_y (MPa ± std)	UTS (MPa ± std)	Elongation at Failure (% ± std)
Plate		-T651*	6*	--	489.0*	556.5*	11.5*
	Plate	-T651	6	76 ± 2	511 ± 3	604 ± 2	12 ± 0.6
		-W	6	78 ± 2	212 ± 15	442 ± 7	22 ± 1
Powder	20/2 ms on/off, 530°C	-W	6	73 ± 4	235 ± 9	409 ± 17	15 ± 3
	30/5 ms on/off, 530°	-W	5	70 ± 3	202 ± 15	400 ± 25	22 ± 6
	36/8 ms on/off, 530°C	-W	6	75 ± 5	198 ± 6	364 ± 14	11 ± 2
	50/5 ms on/off, 530°C	-W	6	70 ± 3	195 ± 12	410 ± 6	26 ± 3
	60/10 ms on/off, 530°C	-W	6	75 ± 6	225 ± 8	380 ± 10	10 ± 2
	72/16 ms on/off, 530°C	-W	6	71 ± 4	195 ± 10	407 ± 8	25 ± 2
	Offgas 20/2 ms on/off, 430°C	-W	6	72 ± 3	204 ± 5	401 ± 18	15 ± 4
	Offgas 20/2 ms on/off, 530°C	-W	6	71 ± 3	202 ± 8	420 ± 12	21 ± 5
	Ball Mill 10 hr, 20/2 ms on/off, 530°C	-W	6	62 ± 6	184 ± 7	252 ± 24	3 ± 0.7
	Ball Mill 10hr, Offgas 20/2 ms on/off, 430°C	-W	6	69 ± 3	208 ± 9	409 ± 5	23 ± 1

4.3.4 Electron Microscopy of Fracture Surfaces for Select Tensile Specimens

Figure 29 exhibits the fracture surfaces for some tensile specimens manufactured by varying on/off pulse lengths. Strong granular texture was noted, and heavy deformation along the boundaries of the individual grains were observed. Higher magnification levels revealed strong indication of highly plastic deformation and signs of large deformation along what was believed to be grain boundaries. Pock marks and divots also noted on a number of the surfaces of the grains and were likely pores formed by trapped gasses during consolidation. Closer inspection did not reveal large, flat, faceted surfaces which would have indicated poor joining of the powder particles. Comparison between the three sets of images revealed that with increasing pulse length, a slight change in the fracture surface occurred from "flatter" fracture surfaces, to ridged surfaces intersecting at 45 degrees.
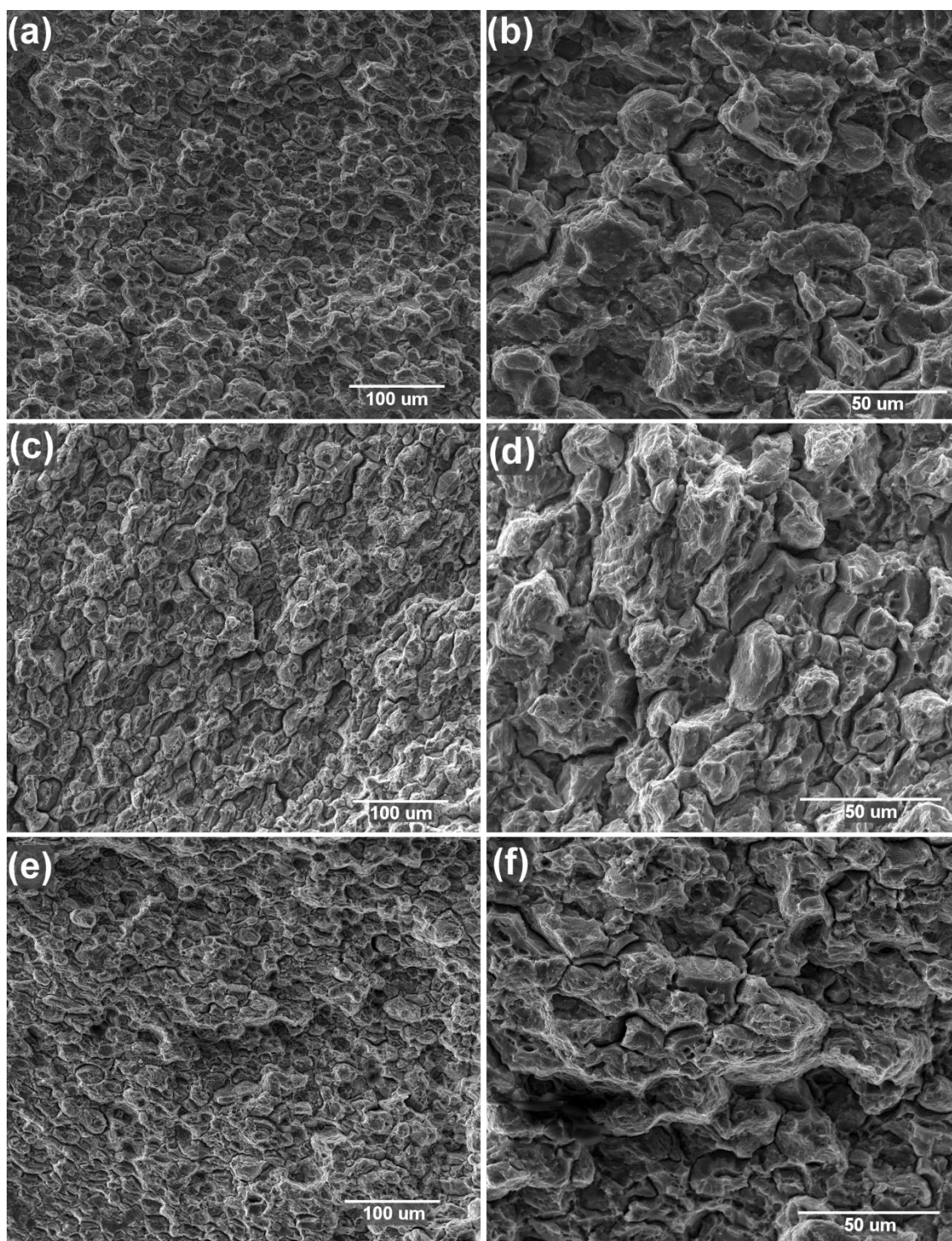
Figure 29. Secondary electron scanning electron microscopy images of fracture surfaces for select tensile specimens manufactured with varying on/off pulse lengths. (a,b) 20/2 ms on/off, (c,d) 50/5 ms on/off, (e,f) 72/16 ms on/off.

118

Figure 30 exhibits the fracture surfaces for a selection of the ball milled, and ball milled and off-gassed powders. The ball milled only powder demonstrated a more faceted fracture surface than the other surfaces investigated. It also demonstrated a higher concentration of the pock marks and divots. The fracture surface of the off-gassed specimen sintered at 530°C demonstrated great similarity to the 50/5 and 72/16 pulse length specimens. It showed plastically deformed surface with large degrees of strain along what was believed to be grain boundaries. It also revealed the pock marks at the very tips of the fracture surfaces for some of the grains. The specimen fabricated from ball milled powders that were off-gassed and then sintered at 430°C also demonstrated significant similarity to the 50/5 and 72/16 pulse length specimens. It did not present the divots and pock marks the other ball milled specimen displayed, and exhibited the large degree of strain along the grain boundaries.
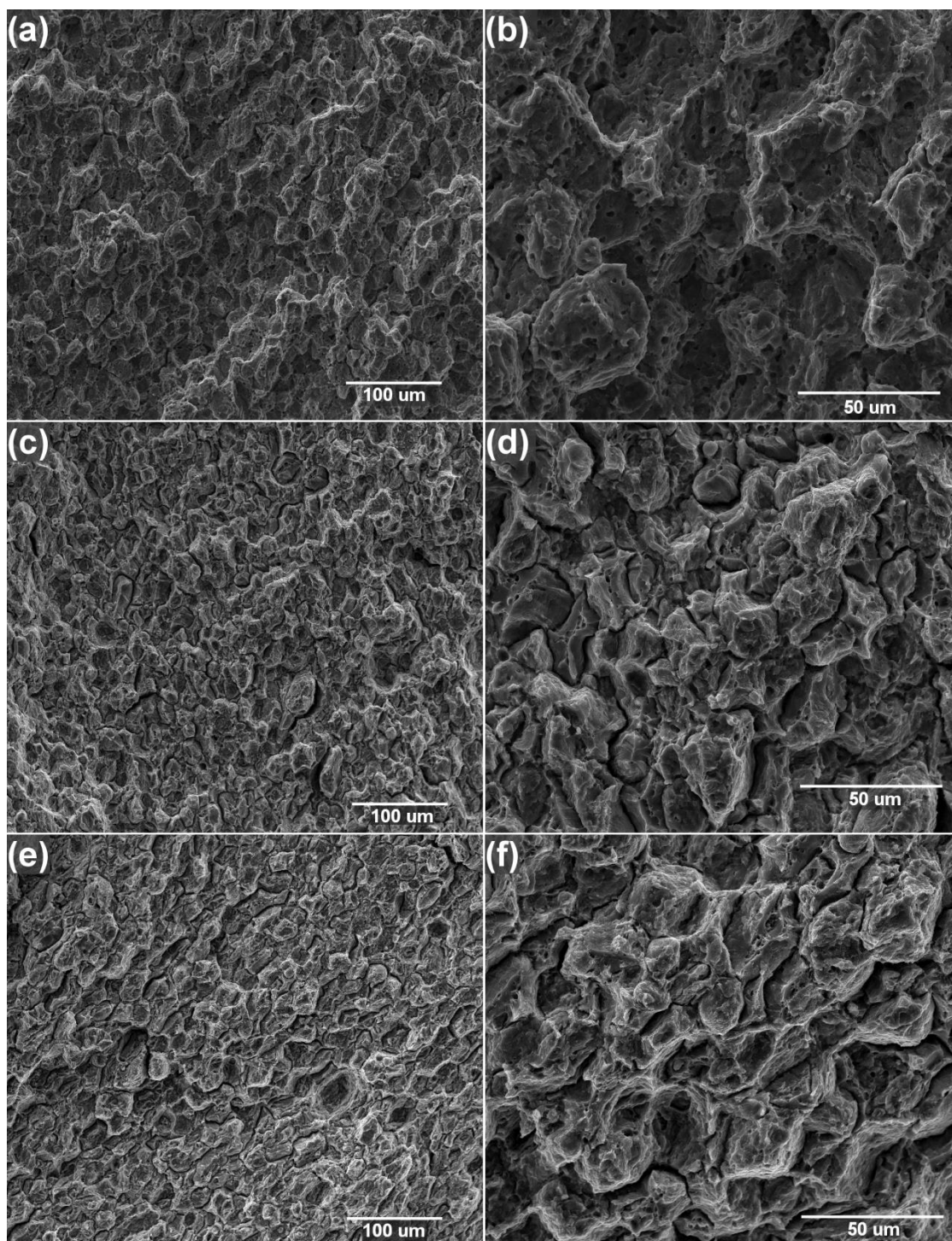
Figure 30. Secondary electron scanning electron microscopy images of fracture surfaces from the specimens manufactured using ball milling and off-gassing. (a,b) off-gassing then sintered at 530°C, (c,d) ball milling then sintering at 530°C, (e,f) ball milling and off-gassing then sintering at 430°C.

4.4 Discussion

Here we have demonstrated mechanical properties similar to commercially available aluminum 7075 plate material were achieved from SPS consolidates by varying on/off pulse lengths, without pre-compaction, in the solution heat treated temper.

4.4.1 Effect of SPS Pulse Length on Tensile Properties

Based upon the results in **Figure 27**, for each on:off pulse ratio, an increase in the "on" pulse length (longer "on" time) yielded an increase in elongation at failure, and a slight increase in ultimate tensile strength. A slight decrease in yield stress was noted for on:off pulse length ratios of 10 and 6; almost no change was observed in yield stress for on:off pulse length ratio of 4.5. Interestingly, the ratios of 50/5 and 72/16 ms on/off produced elongation to failures and yield stresses very similar to the solution heat treated plate material. Additionally, the yield stresses of both were within 10% of the solution heat treated plate material. The ratio of 30/5 ms on/off also produced values notably close to the plate material, however, the sample to sample variation was considerably higher than either the 50/5 or 72/16 ms on/off ratios. We would like to also note that damage to the punches used in consolidation was observed for the extended pulse lengths.

The serrations observed in all cases indicated PLC type matrix instabilities and were expected given the ability of aluminum 7075 to age at room temperature [202-206].

Comparison of the results to literature was difficult as most did not test within the first 30 minutes of solution heat treating, or list time between quench and testing [203].

One group exploring ultrafine grained aluminum alloys show aluminum 7075 ingots with a "coarse grain structure" to have a yield stress of approximately 160 MPa, and an elongation to failure of approximately 18% [207].

4.4.2 Effect of Ball Milling, and Off-gassing on Tensile Properties

Comparing for the same temperature of consolidation and pulse length, off gassing demonstrated a significant increase in elongation at failure of the consolidated powders. For 20/2 ms on/of, off gassing increased failure strain from 15 to 21%.

Consolidation of the off-gassed powder at a lower temperature (430°C) demonstrated very similar properties to the powder consolidated at 530°C for the same pulse length on/off (20/2), except the 430°C demonstrated a slightly lower yield stress.

As compared to the solution heat treated plate material, the off-gassed powder consolidated at 530°C demonstrated a very similar mechanical response. This was unsurprising as 530°C is 95% the melting temperature for aluminum 7075. It was interesting to note, though, the values were achieved in a powder that was not rolled, extruded, or pre-compacted.

Ball milling the powder yielded a surprising decrease in both ultimate tensile strength and elongation at failure. It was expected that the added dislocations induced by ball milling would have added in diffusion, increasing the quality of the consolidate. Further investigations into the reasons for its poor mechanical properties were needed.

Of particular interest, was the combination of ball milling, off-gassing, and consolidation at 430°C demonstrating yield stress and elongation at failure nearly

identical to that of the solution heat treated plate material. It also demonstrated an ultimate tensile strength with 10% that of the solution heat treated plate as well.

4.4.3 Observation of the fracture surfaces

Comparison of the fracture surfaces revealed notable similarity between the samples that demonstrated high elongations at failure. In the case of the ball mill specimen, the divots and pock marks are likely due to gasses trapped during the heating process of consolidation. What was surprising was the notable difference in mechanical properties just ball milling demonstrated. Both varying pulse length and off-gassing the powders in the SPS were generally sufficient to achieve strains of 10-12%. However, even with one hour of off-gassing in a high vacuum environment, divots and pock marks were observed in all specimens.

Of particular interest to the authors was the high degree of similarity in mechanical response between the solution heat treated plate material and the ball milled, then off-gassed powder, sintered at 430°C. While high degree of densification and sintering were expected, as 430°C is 0.77 T_m, the similarity in yield stresses and elongation to failures were not.

4.5 Conclusions

Aluminum 7075 powders were consolidated in an SPS without pre-compaction. Appropriate selection of processing conditions yielded mechanical responses, in the solution heat treated state, similar to solution heat treated, commercially available,

aluminum 7075 plate material. In addition, processing parameters were determined that met the 430°C maximum temperature requirement for use with magnetic SMA particles, and still yielded acceptable yield stress and elongation at failure.

5. COMPOSITE CONSISTING OF ALUMINUM 7075 AND NI$_{43}$CO$_7$MN$_{39}$SN$_{11}$

5.1 Introduction

The previous sections have been devoted to achieving benchmarks one, two and four set forth in section 5.1. However, it still has yet to be demonstrated that the magnetic SMA particles embedded into a matrix undergo martensitic transformation due to stress when plastic strain is applied to the composite in which they reside.

To accomplish this, a composite of aluminum 7075 and Ni$_{43}$Co$_7$Mn$_{39}$Sn$_{11}$ must be fabricated. To investigate the magnetic response of the material in regards to applied plastic strain, the base magnetic response with respect to field intensity will first need to be observed. As seen in the previous sections, the SQUID provides a method by which the magnetization of an entire portion of the composite material can be measured. Since this method measures the magnetic response of a volume of material, care must be taken to ensure the identical volumes are being measured before and after the application of plastic deformation to guarantee the accuracy of conclusions drawn from differences in magnetization. Because of this stipulation compression specimens should be used, and subsequently, the initial investigation in the strain-magnetization relationship should employ compression testing of the composite.

This section will focus on the fabrication of a composite consisting of aluminum 7075 and Ni$_{43}$Co$_7$Mn$_{39}$Sn$_{11}$ magnetic SMA consolidated from powder precursors. The mechanical response of the composite will be investigated under compression testing, and the effect of compressive plastic strain on the magnetization of the composite will be

determined through iterative and incremental straining of the composite material followed by measurement of magnetization induced by a ramping magnetic field.

<p style="text-align: center;">*5.2 Materials and Experimental Methods*</p>

5.2.1 Powder Consolidation and Secondary Heat Treatments

The staring aluminum 7075 powders from section four, and the solution heat treated $Ni_{43}Co_7Mn_{39}Sn_{11}$ from section one were used to manufacture a composite material with a ratio of 2 vol% $Ni_{43}Co_7Mn_{39}Sn_{11}$. Sufficient amounts of both powders were used to create a final consolidate 40 mm in diameter and 8 mm thick. The aluminum 7075 powder was ball milled for 10 hours (as in section four) and was extracted, mixed with the $Ni_{43}Co_7Mn_{39}Sn_{11}$ powder, and mixed via ball milled for 30 minutes (as in section 2). The balls were extracted from the powder mixture via sieve, and the powder mix was poured into a 40 mm graphite die and placed in an SPS. The powder was then processed in the same manner as the consolidate off-gassed and sintered at 703 K in section 4.

Five 5 mm diameter x 1mm thick specimens, along with four other small specimens for microscopy, were cut via wire EDM from the composite. Each microscopy specimen was paired with a 5mm diameter specimen, each was wrapped in tantalum foil, and both the microscopy and 5 mm diameter specimen sealed in a quartz tube under UHP argon. One pair, each, was subjected to 753 K for 10, 20, 30, and 60 minutes, then water quenched into room temperature water.

Two 3 x 3 x 6 mm compression specimens were EDM cut from the composite material. The compression specimens were manufactured to ensure no burs would need

to be removed, post machining, from the parallel surfaces in contact with the compression grips. These sample dimensions were chosen as a compromise between the maximum specimen size the SQUID is capable of testing and ensuring the entire specimen volume is measured.

All specimens were allowed to age at room temperature for ≥ 7 days.

5.2.2 Microstructural Characterization of Composite

The microscopy specimens were mounted in epoxy, mixed with conductive filler, then polished using various steps starting from 600 grit silicon carbide paper down to 0.25 µm diamond suspension at the platen speed of 90 rpm. The specimens were then vibratory polished in 50nm colloidal silica solution for 10 hours. Optical images were taken with a Keyence optical microscrope as stated previously.

5.2.3 Magnetization Characterization of Composite

The thermo-magnetic responses of the as consolidated and heat treated 5mm diameter specimens were carried out using a Quantum Design SQUID-VSM magnetometer with a heating-cooling rate of $10K.min^{-1}$ for the temperature range of 400-100-400 K under constant magnetic fields ranging from 0.05- 7 Tesla.

The specimen from the as consolidated condition (no secondary heat treatment) was also subjected to a ramped magnetic field from 0-7T at 200, 300, and 340 Kelvin with a ramping field rate of 25×10^{-4} $T.s^{-1}$ to determine the pure martensite, mixed, and austenite magnetic responses to increasing field intensity.

The first compression specimen was cooled to 200 K (inside the SQUID), heated to 300 K (inside the SQUID), then subjected to increasing magnetic field from 0-7T with a ramping field rate of 25×10^{-4} T.s^{-1}. This cycle was repeated after the compression specimen was subjected to compressive plastic deformation.

The second compression specimen was placed directly into the SQUID (300 K) and subjected to an increasing magnetic field, from 0-7 Tesla, at a ramped field rate of 25×10^{-4} T.s^{-1} to measure the specimen's room temperature magnetization with increasing field. The specimen was exposed to increasing incremental plastic strains, and after each loading, the magnetization measurements were repeated at 300 K (without prior cooling to 200 K) applying the same field ramping rate as previously stated.

All magnetization values were normalized to the estimated mass of the magnetic particles within the composite. The mass of the magnetic particles was determined using the weight fraction of starting powders required to formulate the composite, assuming homogeneous distribution of the magnetic SMA particles within the composite, and the specimen weight prior testing. In the case of the magnetization experiments on the secondary heat treated specimens, sample mass was used instead.

5.2.3 Mechanical Characterization

Mechanical experiments were conducted on an MTS Insight 30 SL electromechanical test frame at room temperature and an extensometer, attached to the grips with the help of ceramic extension rods, was used to record the axial strain. Specimens were loaded and unloaded at a strain rate of $4.75 \times 10^{-4} (\text{s}^{-1})$ to compressive engineering strains of 7%

for the first specimen, and to 12% (incrementally) for the second. Compression to fracture could not be achieved due to the starting sample dimensions and the compressive strain limit the extensometer was able to measure.

5.3 Experimental Results

5.3.1 Optical Observation of Sintered Compact and Specimens Subjected to Secondary Heat Treatments

Figure 31 displays optical microscope images for the as consolidated composite (a) and the specimens exposed to 753 K for 10-60 minutes (b-e). The presence of a diffusion region between the matrix and the magnetic SMA particle was observed after 10 minutes at the elevated temperature, with the thickness increasing as the length of the heat treatment was extended. Small dark points and clusters, especially noted on (d) and (e) at the boundary between the diffusion region and matrix, were noted to be residual polishing media rather than voids or pores.
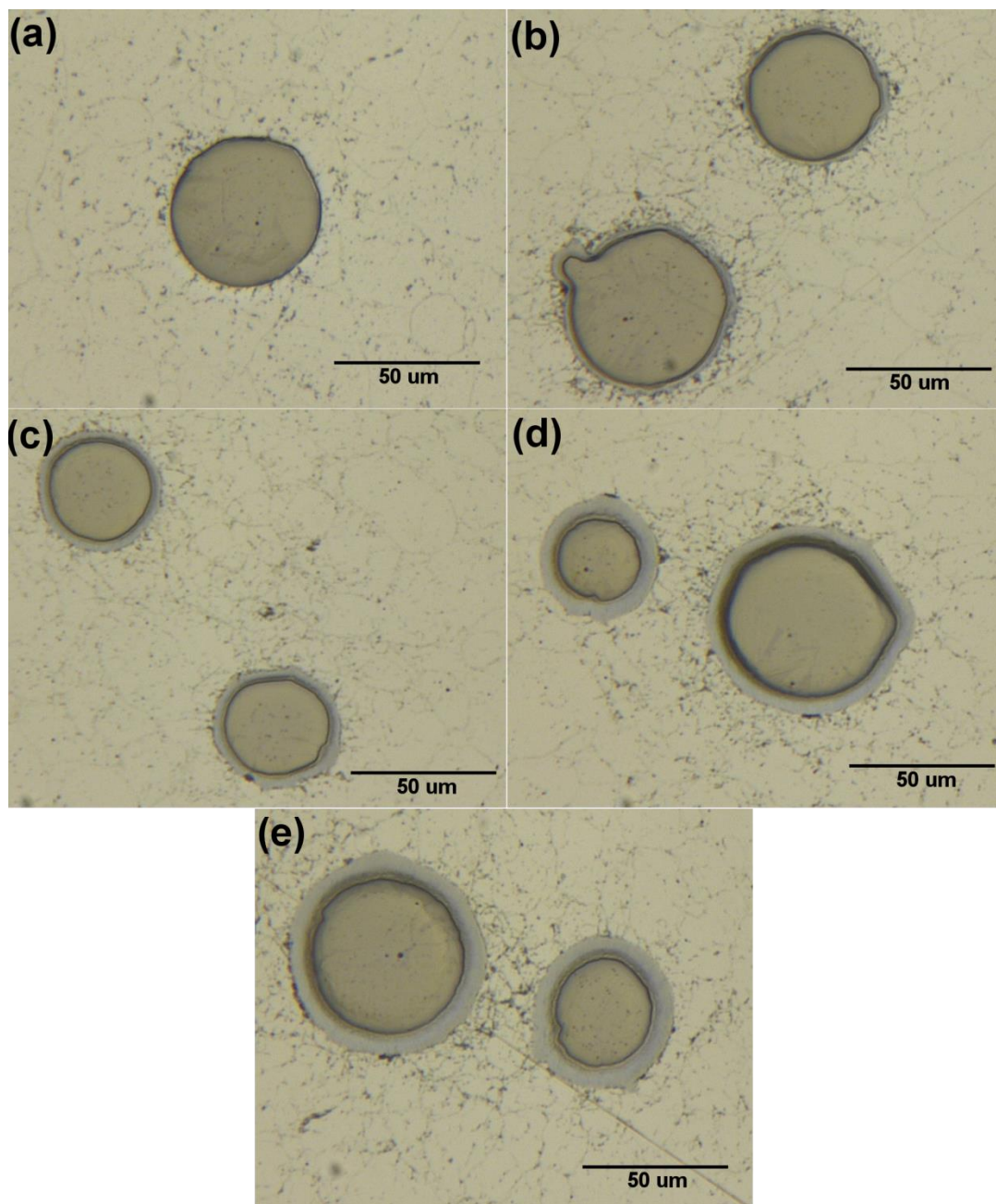
Figure 31. Optical microscopy images of the $Ni_{43}Co_7Mn_{39}Sn_{11}$ particles embedded in the aluminum 7075 matrix. (a) the as consolidated composite, (b) 10 minutes , (c) 20 minutes, (d) 30 minutes, and (e) 60 minutes at 753 K.

5.3.3 Mechanical Response of Sintered Composite via Compression

Figure 32 shows the compressive stress-strain response of the as consolidated composite at room temperature. A maximum compressive stress of 424 MPa was achieved at a compressive engineering strain of 7.2%. Failure was not achieved in this specimen due to the limitation of the extensometer used to measure the strain and the starting sample dimensions.
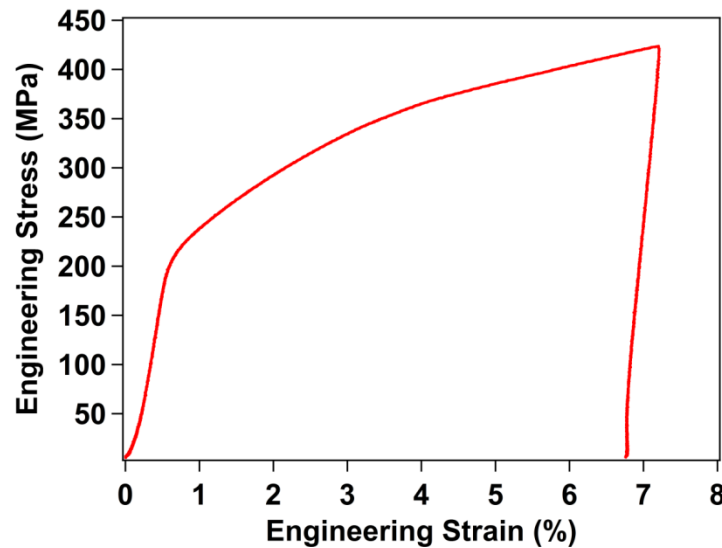
Figure 32. Engineering stress-strain response for the as consolidated composite tested at room temperature under compressive loading conditions. The final strain reported here (6.7%) corresponds to the strain level represented in Figure 36.

Figure 33 displays the incremental, room temperature, compressive stress-strain response of the as consolidated aluminum 7075- $Ni_{43}Co_7Mn_{39}Sn_{11}$ composite. A maximum engineering compressive stress of 581 MPa and engineering strain of 12.2%

131

was achieved. The magnetic scans after each loading sequence did not yield any observable effect on the mechanical response of the composite material.
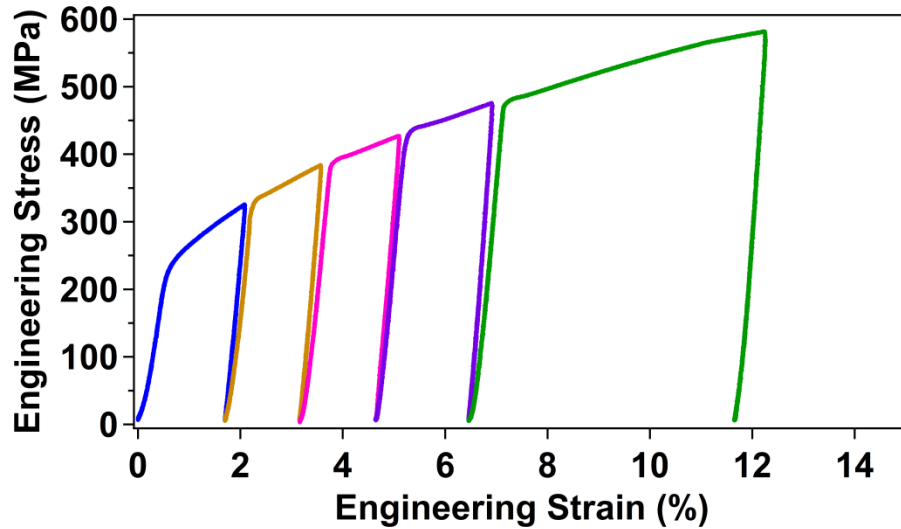
Figure 33. Incremental compressive engineering stress-strain response of the as consolidate aluminum 7075- $Ni_{43}Co_7Mn_{39}Sn_{11}$ composite tested at room temperature. The colors for each curve correspond to the curves of magnetization vs magnetic field in Figure 37 of the same colors.

5.3.2 Magnetization Response of Sintered Compact Specimens

Figure 34 shows the thermo-magnetic response of the as consolidated composite under 0.05, 1, and 7 T. The following transformation temperatures for each field level were determined using the slope intercept method: $0.05T-M_s = 317$ K, $M_f = 255$ K, $A_s = 292$ K, $A_f = 333$ K; $1T-M_s = 319$ K, $M_f = 269$ K, $A_s = 297$ K, $A_f = 334$; $7T-M_s = 297$ K, $M_f = 238$ K, $A_s = 274$ K, $A_f = 313$ K. Comparison to the transformation temperatures of the

parent powder demonstrated a 9 K increase in M_s, a 25 K decrease in M_f, a 13 K decrease in A_s, and a 6 K increase in A_f.
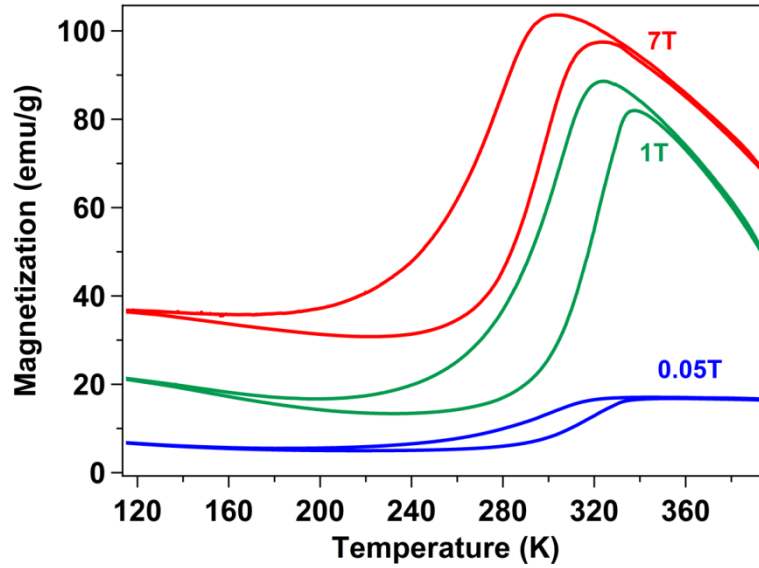
Figure 34. Thermo-magnetic response of the as consolidated composite under increasing bias magnetic field.

Figure 35 demonstrates the magnetization of the as consolidated composite material as a function magnetic field. Temperatures for the fully martensitic and austenitic phases were determined using the data from Figure 34. The magnetization values of the composite material under 7 T magnetic field are nearly identical to those obtained from the thermo-magnetization curves displayed in Figure 34. The hysteresis of the curve measured at 300 K was indicative of magnetic field induce martensitic transformation within the magnetic SMA particles.

Figure 36 displays the magnetization as a function of magnetic field for the first compression specimen, before and after loading to 6.7% plastic engineering strain. The magnetization value obtained at 7 T was in agreement with the value noted at 300 K in **Figure 35**, however the hysteresis observed in the specimen was notably lower. The magnetic response of the composite post compressive deformation demonstrated a magnetic response similar to that of the fully martensitic state of the magnetic SMA particles observed in **Figure 35** which indicated that the magnetic SMA particles were in the martensitic state. The magnetization values for the martensite and austenite phases under a bias magnetic field of 7 T (from **Figure 35**) are indicated by the black dashed lines and labeled accordingly.
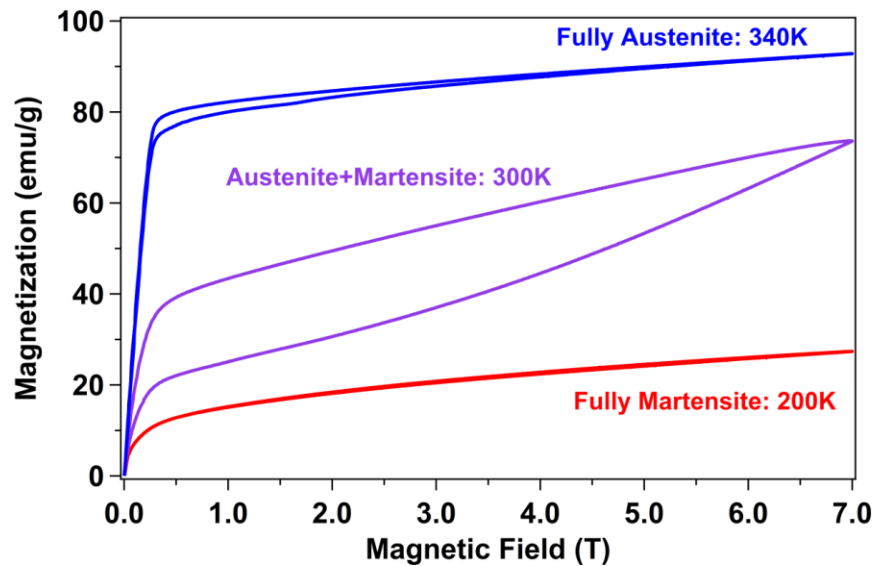
Figure 35. Magnetization as function of increasing magnetic field for the as consolidated composite. Note that the magnetization values at 7T determined for the fully martensitic and austenitic phases are in good agreement with the values demonstrated in figure 34.
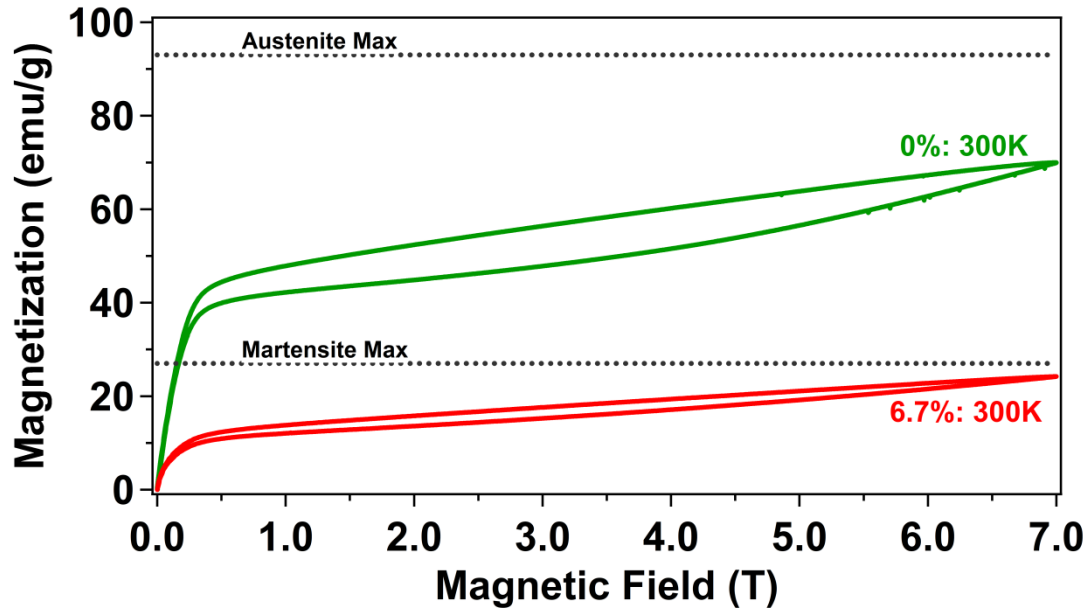
Figure 36. Magnetization vs applied magnetic field for the compression specimen cut from the composite, before and after application of 6.7% plastic strain. The dashed lines indicate the magnetization of the composite under 7T for austenitic and martensitic states of the magnetic SMA particles within the composite as determined in Figure 35.

Figure 37 shows the magnetic response of the as consolidated composite at 300 K after increasing incremental compressive strains (at 300 K). The degree of deformation is indicated by the number above each curve or with an arrow. Black dashed lines indicate the maximum magnetization for the austenitic and martensitic phases as determined in **Figure 35**. Compressive strains beyond 4.7% engineering strain reduced the magnetization of the composite below that of the maximum magnetization observed for the martensitic phase.

Figure 38 gives the magnetization values under 7 T, from Figure 37, plotted as a function of the applied compressive plastic strains (from **Figure 33**).
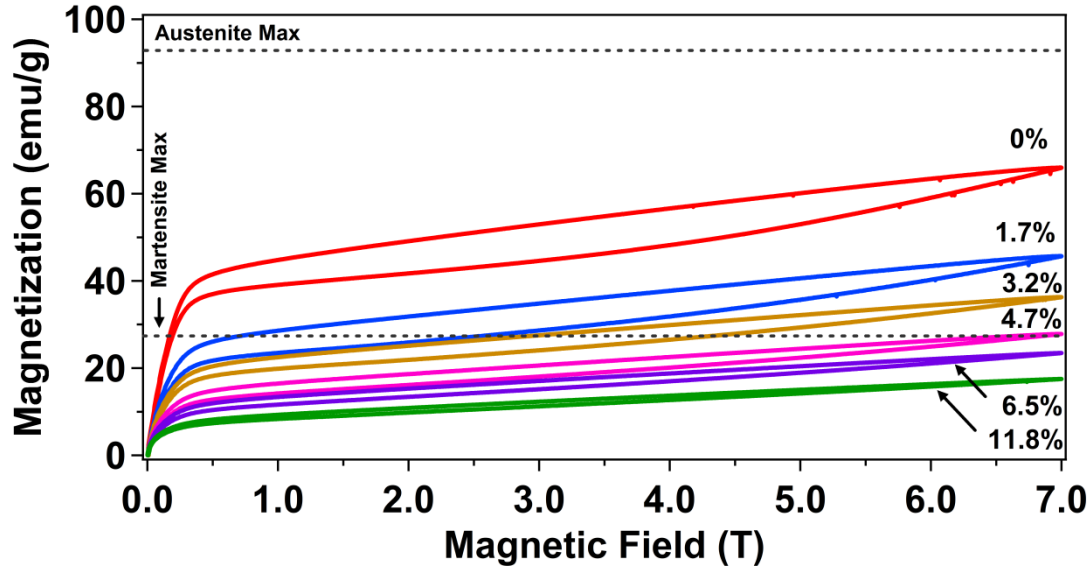
Figure 37. Magnetic response of the composite under increasing magnetic field after exposure to incrementally increasing compressive strains. The colors for each curve refer to the corresponding compression test given in Figure 33.
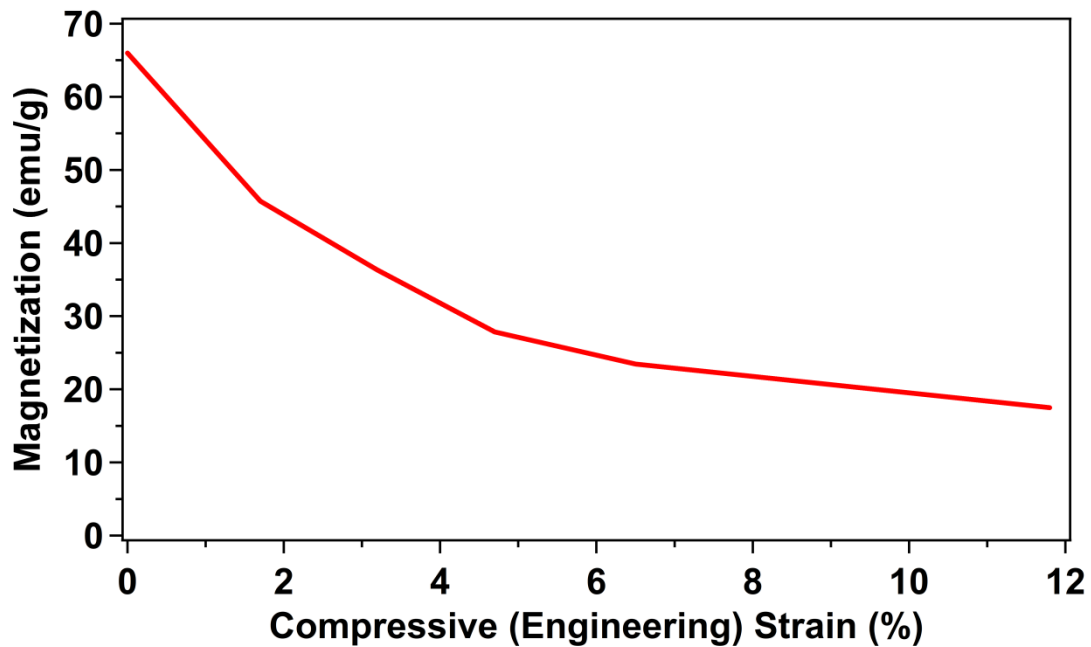
Figure 38. Magnetization of the composite at 7 T plotted as a function of applied compressive plastic strain.

5.3.3 Effect of Secondary Heat Treatments on the Magnetization of the Composite

Figure 39 shows the evolution of the magnetic response of the composite as exposure time to 753 K is increased from 10-60 minutes. An overall reduction in magnetization was observed (similar to the pure aluminum specimens), and a small upward shift in transformation temperatures was noted as compared to the as consolidated state (also in agreement with the pure aluminum experiments).
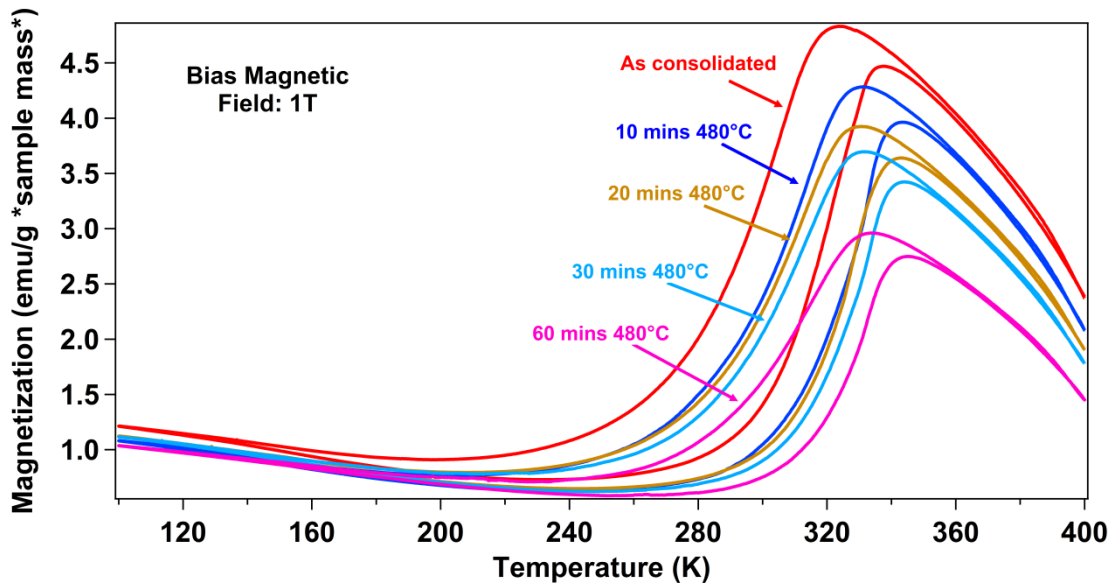
Figure 39. The magnetic response of the composite subjected to increasing times exposed to 753 K.

5.4 Discussion

We have shown that $Ni_{43}Co_7Mn_{39}Sn_{11}$ magnetic SMA powders can successfully be embedded into aluminum 7075 matrix through the consolidation of powder precursors. Consolidation of the powders led to a composite with no optically observable pores in

the matrix, and no observable diffusion between the magnetic SMA particles and aluminum 7075 matrix. Subsequent thermo-magnetic characterization of the as consolidated composite revealed similar magnetic responses to the parent magnetic SMA powder, and application of plastic strain to the composite demonstrated a notable reduction in magnetization at 300 K. Attempts to initiate and grow a diffusion region between the magnetic SMA particles and matrix were successful at 753 K, demonstrating an increase in diffusion region thickness with increasing time.

5.4.1 Magnetic Response of Aluminum 7075- $Ni_{43}Co_7Mn_{39}Sn_{11}$ Composite

As with the specimens prepared using pure aluminum, the composite manufactured using aluminum 7075 still maintain the magnetic signature of the parent $Ni_{43}Co_7Mn_{39}Sn_{11}$ powder particles, and demonstrated the downward shift in Ms and As. This is attributed to the stresses induced by the two materials' differing coefficients of thermal expansion. In the same manner the sintered $Ni_{43}Co_7Mn_{39}Sn_{11}$ demonstrated lower transformation temperatures than the loose powders, the interface between the particle and the matrix increases the amount of energy required to finish martensitic transformation. The further required undercooling was exhibited as a lower Mf temperature. Since the interface stores elastic energy, the As temperature would also be decreased, as the stored elastic energy encourages the transformation back to martensite.

In regards to the magnetic response with increasing field, 7T was sufficient field strength to partially induce transformation to austenite at room temperature. While the mixed state did not fully finish transformation, yielding similar to the fully austenitic

138

state, the level of magnetization under 7T was significantly higher than the purely martensitic state. This indicated that the particles partially in the martensitic state could be transformed back into austenite, and that the particles still in austenite registered the same signal.

5.4.2 Effect of Compressive Strain on the Magnetic Response of Aluminum 7075-$Ni_{43}Co_7Mn_{39}Sn_{11}$ Composite

Straining the composite material demonstrated a significant change in the magnetization of the composite, with the compressed composite yielding a magnetization level three times lower at 7T than the unstrained material. This suggested the plastic deformation within the aluminum 7075 matrix imposed sufficiently high stresses to transform the $Ni_{43}Co_7Mn_{39}Sn_{11}$ particle fully into martensite, or prohibit its transformation back to austenite. The observed reduction in magnetization level for the specimen measured at 300 K as compared to the specimen measured at 200 K was likely a result of the difference in temperatures at which the specimens were measured. As magnetic susceptibility is a power law function of temperature (approaching T_c from the left), it is expected that the magnetization measured for the same level of imposed magnetic field would decrease as the temperature at which the specimen is measured approached the Curie temperature.

Comparison of the magnetic responses for the two compression specimens at similar levels of plastic strain yielded good agreement in magnetization values.

5.4.3 Effect of Secondary Heat Treatments on the Magnetic Response of Aluminum 7075- $Ni_{43}Co_7Mn_{39}Sn_{11}$ Composite

As with the pure aluminum composite, the aluminum 7075 composite demonstrated a reduction in magnetization with increasing diffusion region thickness. It was believed the drop in magnetization was due to material loss from the $Ni_{43}Co_7Mn_{39}Sn_{11}$ particle and slight shifts in composition of the particle at the boundary with the diffusion region (as seen in section 3).

5.5 Conclusions

A composite consisting of aluminum 7075 and $Ni_{43}Co_7Mn_{39}Sn_{11}$ magnetic SMA materials was successfully manufactured without observable diffusion between the $Ni_{43}Co_7Mn_{39}Sn_{11}$ particle and the aluminum 7075 matrix. Characterization of its thermomagnetic properties demonstrated a similar response to parent magnetic SMA particles. Application of compressive strain to the composite demonstrated a significant reduction in the magnetization under 7T, while also demonstrating a stress of 581 MPa at 12.2% strain. Further microstructural characterization is needed to confirm the observations produced through mechanical and magnetic measurements. In addition, investigations into how the magnetic SMA particles behave in the presence of cracks should also be initiated.

Here the last benchmark for successful integration of magnetic SMAs as sensory materials has been achieved. The aluminum 7075-$Ni_{43}Co_7Mn_{39}Sn_{11}$ composite demonstrated a notable change in magnetization after undergoing plastic deformation.

6. CONCLUSIONS

In this body of work, we have demonstrated a number of achievements. First, $Ni_{43}Co_7Mn_{39}Sn_{11}$ magnetic SMA particles can be successfully embedded in a matrix through the use of powder precursors. Second, chemical bonding between the matrix and particle is necessary to ensure stress transfer from the matrix to the particle, and to minimize debonding.

Third, careful control of the diffusion between the particle and matrix is necessary to minimize the negative impact the diffusion region has on the mechanical properties of the matrix. Fourth, a highly ductile matrix is not suitable for $Ni_{43}Co_7Mn_{39}Sn_{11}$ particles with large diffusion regions, as the incompatibilities between the matrix and diffusion region promote fracture and debonding. Fifth, for an aluminum matrix, the diffusion region is divided into two parts. The outer is comprised of Al-Ni, Al-Mn, and Al-Ni-Mn intermetallics and solid solutions, while the inner is comprised of Mn-Sn intermetallics, and Ni-Mn-Sn solid solutions. Sixth, through the modification of pulse length, and through ball milling and off-gassing, aluminum 7075 powder can be consolidated in an SPS, without pre-compaction, and yield mechanical responses similar to that of aluminum 7075 (all materials in the solution heat treated condition).

Seventh, the same processing parameters used to achieve high quality powder consolidations in aluminum 7075 powder can be applied to a $Ni_{43}Co_7Mn_{39}Sn_{11}$ and aluminum 7075 powders yielding a composite with no diffusion between the magnetic SMA particle and the matrix. Finally, we have shown that compression of the composite

material leads to a significant reduction in the magnetization of the composite material under 7T.

From these, five major conclusions may be drawn. First, embedding the particles into a metallic matrix was not as simple as previously hoped. Restrictions placed on the processing conditions to limit diffusion between the metallic matrices and the magnetic SMA particles, increase the difficulty in achieving highly dense matrices with acceptable mechanical properties. This was further exacerbated in the case of aluminum 7075 as secondary heat treatments are required to achieve peak strength in the matrix alloy, and were sufficiently high to promote diffusion between the matrix and magnetic SMA particle. Therefore, non-magnetic metallic matrices that do not exhibit precipitation hardening, and can be acquired in powder form, are likely to have greater success with incorporation of the magnetic SMA sensory material.

Second, chemical bonding between the sensory particle and the matrix is required to guarantee transfer of stress from the matrix to the sensory particle. Without a bond of sufficient strength, transformation of the particle is not guaranteed, and may instead debond from the matrix. In conjunction with the already presented difficulties for processing, this indicates that until further progress is made with the technique, it is likely to only have niche applications. Processing methods that grant greater control over, or severely limits, diffusion will provide a necessary means to expand usage of this technique. One possible method might be coating the magnetic SMA particles with a material that strongly bonds to the matrix and sensory particle during powder consolidation, but inhibits diffusion between matrix and the magnetic SMA particle.

Third, large differences in coefficients of thermal expansion between the embedded sensory material and the matrix may have an undesired effect on the fatigue response of the composite. The residual compressive stresses induced within the sensory particles, and subsequent tensile stresses in the matrix, of the composites investigated above will draw the fatigue cracks towards the sensory particles. Coupled with the difficulties in processing, it is likely then the composite will demonstrate a reduced fatigue response if processing is not optimized and carefully controlled. It might also be possible to use the induced stresses from largely different coefficients of thermal expansion as a design tool to "channel" fatigue cracks into specific directions of component by employing a sequence of particles situated in a manner that encourages fatigue crack growth in a specific and predetermined direction.

Fourth, mechanical tensile tests should be more regularly included to characterize the mechanical properties of the SPS consolidated metallic alloys. Determining density, and characterizing the mechanical response under compression may not be sufficient to determine success or failure of an SPS consolidate.

Lastly, magnetization measurement methods that scan volumes are sufficient to demonstrate the change in magnetization of the magnetic SMA particles due to plastic deformation in the matrix, but are not sufficient to quantify localized damage. Successful application of this non-destructive testing method will require the development of new magnetic scanning techniques, capable of penetrating surfaces, and quantifying magnetization.

REFERENCES

1. Farrar, C.R. and Worden, K., *An introduction to structural health monitoring.* Philosophical Transactions of the Royal Society A: Mathematical, Physical and Engineering Sciences, 2007. **365**(1851): p. 303-315.

2. Balageas, D., Fritzen, C.-P., and Güemes, A., *Structural health monitoring*. Vol. 90. 2010: John Wiley & Sons.

3. Chang, F.-K., *Structural health monitoring: current status and perspectives*. 1998: CRC Press.

4. Barke, D. and Chiu, W., *Structural health monitoring in the railway industry: a review.* Structural Health Monitoring, 2005. **4**(1): p. 81-93.

5. Mancini, S., Tumino, G., and Gaudenzi, P., *Structural Health Monitoring for Future Space Vehicles.* Journal of Intelligent Material Systems and Structures, 2006. **17**(7): p. 577-585.

6. Chawla, K.K. and Meyers, M., *Mechanical behavior of materials*. 1999: Prentice Hall Upper Saddle River.

7. Worden, K. and Dulieu-Barton, J.M., *An overview of intelligent fault detection in systems and structures.* Structural Health Monitoring, 2004. **3**(1): p. 85-98.

8. Farrar, C.R., Sohn, H., Hemez, F.M., Anderson, M.C., Bement, M.T., Cornwell, P.J., Doebling, S.W., Schultze, J., Lieven, N., and Robertson, A., *Damage prognosis: current status and future needs.* Los Alamos National Laboratory, LA, 2003. **176**: p. 177-178.

9.   Giurgiutiu, V., Redmond, J.M., Roach, D.P., and Rackow, K. *Active sensors for health monitoring of aging aerospace structures*. in *SPIE's 7th Annual International Symposium on Smart Structures and Materials*. 2000. SPIE.

10.   Mal, A., Banerjee, S., and Ricci, F., *An automated damage identification technique based on vibration and wave propagation data.* Philosophical Transactions of the Royal Society of London A: Mathematical, Physical and Engineering Sciences, 2007. **365**(1851): p. 479-491.

11.   Staszewski, W., Boller, C., and Tomlinson, G.R., *Health monitoring of aerospace structures: smart sensor technologies and signal processing*. 2004: John Wiley & Sons.

12.   Derriso, M., Pratt, D., Homan, D., Schroeder, J., and Bortner, R., *Integrated vehicle health management: the key to future aerospace systems.* Structural Health Monitoring, 2003: p. 3-11.

13.   Goranson, U., *Jet transport structures performance monitoring.* Structural Health Monitoring Current Status and Perspectives, 1997: p. 3-17.

14.   Lopez, I. and Sarigul-Klijn, N., *A review of uncertainty in flight vehicle structural damage monitoring, diagnosis and control: Challenges and opportunities.* Progress in Aerospace Sciences, 2010. **46**(7): p. 247-273.

15.   Mickens, T., Schulz, M., Sundaresan, M., Ghoshal, A., Naser, A., and Reichmeider, R., *Structural health monitoring of an aircraft joint.* Mechanical Systems and Signal Processing, 2003. **17**(2): p. 285-303.

16.   Leblanc, B., Niezrecki, C., and Avitabile, P. *Structural health monitoring of helicopter hard landing using 3D digital image correlation.* in *SPIE Smart Structures and Materials+ Nondestructive Evaluation and Health Monitoring.* 2010. International Society for Optics and Photonics.

17.   Swait, T.J., Jones, F.R., and Hayes, S.A., *A practical structural health monitoring system for carbon fibre reinforced composite based on electrical resistance.* Composites Science and Technology, 2012. **72**(13): p. 1515-1523.

18.   Doebling, S.W., Farrar, C.R., Prime, M.B., and Shevitz, D.W., *Damage identification and health monitoring of structural and mechanical systems from changes in their vibration characteristics: a literature review.* 1996.

19.   Rytter, A., *Vibrational based inspection of civil engineering structures.* 1993, Dept. of Building Technology and Structural Engineering, Aalborg University.

20.   Sohn, H., Farrar, C.R., Hemez, F.M., Shunk, D.D., Stinemates, D.W., Nadler, B.R., and Czarnecki, J.J., *A review of structural health monitoring literature: 1996–2001.* Los Alamos National Laboratory, USA, 2003.

21.   Staszewski, W.J., Mahzan, S., and Traynor, R., *Health monitoring of aerospace composite structures – Active and passive approach.* Composites Science and Technology, 2009. **69**(11): p. 1678-1685.

22.   Mcmaster, R.C., *Nondestructive testing handbook. Volume 3-Liquid Penetrant Tests.* 2nd ed. 1982, Columbus, OH.

23.   Shull, P.J., *Nondestructive evaluation: theory, techniques, and applications.* 2002: CRC press.

24. Nguyen, T.H., Venugopala, T., Chen, S., Sun, T., Grattan, K.T.V., Taylor, S.E., Basheer, P.a.M., and Long, A.E., *Fluorescence based fibre optic pH sensor for the pH 10–13 range suitable for corrosion monitoring in concrete structures.* Sensors and Actuators B: Chemical, 2014. **191**: p. 498-507.

25. Fritzen, C.P., *Vibration-Based Techniques for Structural Health Monitoring.* Structural Health Monitoring, 2006: p. 45-224.

26. Finlayson, R.D., Friesel, M., Carlos, M., Cole, P., and Lenain, J.C., *Health Monitoring of Aerospace Structures with Acoustic Emicssion and Acousto-ultrasonics.* Insight, 2001. **43**(3).

27. Guo, H., Xiao, G., Mrad, N., and Yao, J., *Fiber optic sensors for structural health monitoring of air platforms.* Sensors, 2011. **11**(4): p. 3687-3705.

28. Chan, T.H., Yu, L., Tam, H.-Y., Ni, Y.-Q., Liu, S., Chung, W., and Cheng, L., *Fiber Bragg grating sensors for structural health monitoring of Tsing Ma bridge: Background and experimental observation.* Engineering structures, 2006. **28**(5): p. 648-659.

29. López-Higuera, J.M., Cobo, L.R., Incera, A.Q., and Cobo, A., *Fiber optic sensors in structural health monitoring.* Journal of lightwave technology, 2011. **29**(4): p. 587-608.

30. Tennyson, R., Mufti, A., Rizkalla, S., Tadros, G., and Benmokrane, B., *Structural health monitoring of innovative bridges in Canada with fiber optic sensors.* Smart materials and Structures, 2001. **10**(3): p. 560.

31.   Ken, P.C., Nicholas, J.C., and Glenn, W., *Health monitoring of civil infrastructures.* Smart Materials and Structures, 2003. **12**(3): p. 483.

32.   Li, H.-N., Li, D.-S., and Song, G.-B., *Recent applications of fiber optic sensors to health monitoring in civil engineering.* Engineering Structures, 2004. **26**(11): p. 1647-1657.

33.   Brownjohn, J.M.W., *Structural health monitoring of civil infrastructure.* Philosophical Transactions of the Royal Society A: Mathematical, Physical and Engineering Sciences, 2007. **365**(1851): p. 589-622.

34.   Tapanes, E. *Fibre optic sensing solutions for real-time pipeline integrity monitoring*. in *Australian Pipeline Industry Association National Convention*. 2001.

35.   Fernandez, M., Tapanes, E., and Zelitskaya, P. *Pipeline hydrocarbon transportation: some operating concerns and R&D trends*. in *1996 1st International Pipeline Conference*. 1996. American Society of Mechanical Engineers.

36.   Claus, R.O., Holton, C.E., and Zhao, W. *Performance of optical fiber sensors embedded in polymer matrix composites for 15 years*. in *Smart Structures and Materials 1998: Sensory Phenomena and Measurement Instrumentation for Smart Structures and Materials*. 1998. International Society for Optics and Photonics.

37.   Ono, K., *Review on Structural Health Evaluation with Acoustic Emission.* Applied Sciences, 2018. **8**(6): p. 958.

38.   Heiple, C. and Carpenter, S., *Acoustic emission produced by deformation of metals and alloys-A review*. Journal of Acoustic Emission, 1987. **6**: p. 177-204.

39.   Nair, A. and Cai, C., *Acoustic emission monitoring of bridges: Review and case studies*. Engineering structures, 2010. **32**(6): p. 1704-1714.

40.   Morton, T., Harrington, R., and Bjeletich, J., *Acoustic emissions of fatigue crack growth*. Engineering fracture mechanics, 1973. **5**(3): p. 691-697.

41.   Berkovits, A. and Fang, D., *Study of fatigue crack characteristics by acoustic emission*. Engineering Fracture Mechanics, 1995. **51**(3): p. 401-416.

42.   Huang, M., Jiang, L., Liaw, P.K., Brooks, C.R., Seeley, R., and Klarstrom, D.L., *Using acoustic emission in fatigue and fracture materials research*. JOM, 1998. **50**(11): p. 1-14.

43.   Carpinteri, A., Lacidogna, G., and Pugno, N., *Structural damage diagnosis and life-time assessment by acoustic emission monitoring*. Engineering Fracture Mechanics, 2007. **74**(1-2): p. 273-289.

44.   Lindley, T., Palmer, I., and Richards, C., *Acoustic emission monitoring of fatigue crack growth*. Materials Science and Engineering, 1978. **32**(1): p. 1-15.

45.   Roberts, T. and Talebzadeh, M., *Acoustic emission monitoring of fatigue crack propagation*. Journal of Constructional Steel Research, 2003. **59**(6): p. 695-712.

46.   Dunegan, H. and Harris, D., *Acoustic emission-a new nondestructive testing tool*. Ultrasonics, 1969. **7**(3): p. 160-166.

47.   Scruby, C.B., *An introduction to acoustic emission*. Journal of Physics E: Scientific Instruments, 1987. **20**(8): p. 946.

48.   Guy, P. and Monnier, T., *Structural Health Monitoring with Piezoelectric Sensors*, in *Structural Health Monitoring*. 2006, ISTE. p. 287-377.

49.   Fritzen, C.-P., *Vibration-Based Techniques for Structural Health Monitoring*, in *Structural Health Monitoring*. 2006, ISTE. p. 45-224.

50.   Rogers, C.A., *Active vibration and structural acoustic control of shape memory alloy hybrid composites: experimental results.* The Journal of the Acoustical Society of America, 1990. **88**(6): p. 2803-2811.

51.   Cornell, S.R., Leser, W.P., Hochhalter, J.D., Newman, J.A., and Hartl, D.J. *Development and Characterization of Embedded Sensory Particles Using Multi-Scale 3D Digital Image Correlation*. in *ASME 2014 Conference on Smart Materials, Adaptive Structures and Intelligent Systems*. 2014. American Society of Mechanical Engineers.

52.   Wei, Z., Sandstroröm, R., and Miyazaki, S., *Shape-memory materials and hybrid composites for smart systems: Part I Shape-memory materials.* Journal of Materials Science, 1998. **33**(15): p. 3743-3762.

53.   Wallace, T.A., Smith, S.W., Piascik, R.S., Horne, M.R., Messick, P.L., Alexa, J.A., Glaessgen, E.H., and Hailer, B.T., *Strain-detecting composite materials*. 2016, Google Patents.

54.   Yamada, Y., Taya, M., and Watanabe, R., *Strengthening of metal matrix composite by shape memory effect.* Materials Transactions, JIM, 1993. **34**(3): p. 254-260.

55.   Otsuka, K. and Shimizu, K., *Pseudoelasticity and shape memory effects in alloys.* International Metals Reviews, 1986. **31**(1): p. 93-114.

56.   Miyazaki, S. and Otsuka, K., *Development of Shape Memory Alloys.* ISIJ International, 1989. **29**(5): p. 353-377.

57.   Otsuka, K. and Wayman, C.M., *Shape memory materials*. 1999: Cambridge university press.

58.   Karaca, H.E., Karaman, I., Basaran, B., Ren, Y., Chumlyakov, Y.I., and Maier, H.J., *Magnetic Field-induced Phase Transformation in NiMnColn Magnetic Shape-Memory Alloys-A New Actuation Mechanism with Large Work Output.* Advanced Functional Materials, 2009. **19**(7): p. 983-998.

59.   Karaman, I., Basaran, B., Karaca, H., Karsilayan, A., and Chumlyakov, Y., *Energy harvesting using martensite variant reorientation mechanism in a NiMnGa magnetic shape memory alloy.* Applied Physics Letters, 2007. **90**(17): p. 172505.

60.   Ullakko, K., Yakovenko, P.G., and Gavriljuk, V.G. *New developments in actuator materials as reflected in magnetically controlled shape memory alloys and high-strength shape memory steels*. 1996.

61.   Karaca, H.E., Karaman, I., Brewer, A., Basaran, B., Chumlyakov, Y.I., and Maier, H.J., *Shape memory and pseudoelasticity response of NiMnCoIn magnetic shape memory alloy single crystals.* Scripta Materialia, 2008. **58**(10): p. 815-818.

62.   Karaca, H., Karaman, I., Basaran, B., Chumlyakov, Y.I., and Maier, H., *Magnetic field and stress induced martensite reorientation in NiMnGa*

151

ferromagnetic shape memory alloy single crystals. Acta Materialia, 2006. **54**(1): p. 233-245.

63. Guiza-Arguello, V.R., Monroe, J.A., Karaman, I., and Hahn, M.S., *Cytocompatibility evaluation of NiMnSn meta-magnetic shape memory alloys for biomedical applications.* Journal of Biomedical Materials Research Part B: Applied Biomaterials, 2016. **104B**: p. 853-863.

64. Bruno, N.M., *The Magnetocaloric and Elastocaloric Effects in Magnetic Shape Memory Alloys*, in *Doctoral Dissertation*. 2015: Texas A&M University.

65. Kiefer, B., Karaca, H., Lagoudas, D., and Karaman, I., *Characterization and modeling of the magnetic field-induced strain and work output in Ni2MnGa magnetic shape memory alloys.* Journal of Magnetism and Magnetic Materials, 2007. **312**(1): p. 164-175.

66. Emre, B., Bruno, N.M., Emre, S.Y., and Karaman, I., *Effect of niobium addition on the martensitic transformation and magnetocaloric effect in low hysteresis NiCoMnSn magnetic shape memory alloys.* Applied Physics Letters, 2014. **105**(23): p. 231910.

67. Sozinov, A., Likhachev, A.A., Lanska, N., and Ullakko, K., *Giant magnetic-field-induced strain in NiMnGa seven-layered martensitic phase.* Applied Physics Letters, 2002. **80**(10): p. 1746-1748.

68. Bruno, N.M., Yegin, C., Karaman, I., Chen, J.H., Ross, J.H., Liu, J., and Li, J.G., *The effect of heat treatments on Ni43Mn42Co4Sn11 meta-magnetic shape memory alloys for magnetic refrigeration.* Acta Materialia, 2014. **74**: p. 66-84.

69.   Karaca, H.E., Karaman, I., Basaran, B., Chumlyakov, Y.J., and Maier, H.J., *Magnetic field and stress induced martensite reorientation in NiMnGa ferromagnetic shape memory alloy single crystals.* Acta Materialia, 2006. **54**(1): p. 233-245.

70.   Koyama, K., Watanabe, K., Kanomata, T., Kainuma, R., Oikawa, K., and Ishida, K., *Observation of field-induced reverse transformation in ferromagnetic shape memory alloy Ni50Mn36Sn14.* Applied Physics Letters, 2006. **88**(13).

71.   Oikawa, K., Ito, W., Imano, Y., Sutou, Y., Kainuma, R., Ishida, K., Okamoto, S., Kitakami, O., and Kanomata, T., *Effect of magnetic field on martensitic transition of Ni46Mn41In13 Heusler alloy.* Applied Physics Letters, 2006. **88**(12).

72.   Brown, P.J., Gandy, A.P., Ishida, K., Kainuma, R., Kanomata, T., Neumann, K.U., Oikawa, K., Ouladdiaf, B., and Ziebeck, K.R.A., *The magnetic and structural properties of the magnetic shape memory compound Ni2Mn1.44Sn0.56.* Journal of Physics-Condensed Matter, 2006. **18**(7): p. 2249-2259.

73.   Kainuma, R., Imano, Y., Ito, W., Morito, H., Sutou, Y., Oikawa, K., Fujita, A., Ishida, K., Okamoto, S., and Kitakami, O., *Metamagnetic shape memory effect in a Heusler-type Ni43Co7Mn39Sn11 polycrystalline alloy.* Applied Physics Letters, 2006. **88**(19).

74. Tickle, R. and James, R.D., *Magnetic and magnetomechanical properties of Ni2MnGa.* Journal of Magnetism and Magnetic Materials, 1999. **195**(3): p. 627-638.

75. Kainuma, R., Ito, K., Ito, W., Umetsu, R., Kanomata, T., and Ishida, K., *NiMn-Based Metamagnetic Shape Memory Alloys*, in *Ferromagnetic Shape Memory Alloys Ii*, V.A. Chernenko and J.M. Barandiaran, Editors. 2010, Trans Tech Publications Ltd: Stafa-Zurich. p. 23-31.

76. Kainuma, R., Oikawa, K., Ito, W., Sutou, Y., Kanomata, T., and Ishida, K., *Metamagnetic shape memory effect in NiMn-based Heusler-type alloys.* Journal of Materials Chemistry, 2008. **18**(16): p. 1837-1842.

77. Monroe, J., Cruz-Perez, J., Yegin, C., Karaman, I., Geltmacher, A., Everett, R., and Kainuma, R., *Magnetic response of porous NiCoMnSn metamagnetic shape memory alloys fabricated using solid-state replication.* Scripta Materialia, 2012. **67**(1): p. 116-119.

78. Kanomata, T., Fukushima, K., Nishihara, H., Kainuma, R., Itoh, W., Oikawa, K., Ishida, K., Neumann, K., and Ziebeck, K., *Magnetic and crystallographic properites of shape memory alloys Ni2Mn1+xSn1-x.* Materials Science Forum, 2008. **583**: p. 10.

79. R. Kainuma, K.I., W. Ito, R. Y. Umetsu, T. Kanomata and K. Ishida, *NiMn-based metamagnetic shape memory alloys.* Materials Science Forum, 2010. **635**: p. 8.

80. Karaca, H.E., Karaman, I., Basaran, B., Ren, Y., Chumlyakov, Y.I., and Maier, H.J., *Magnetic Field-induced Phase Transformation in NiMnCoIn Magnetic Shape-Memory Alloys-A New Actuations Mechanism with Large Work Output.* Advanced Functional Materials, 2009. **19**: p. 983-998.

81. Porter, G., Liaw, P., Tiegs, T., and Wu, K., *Fatigue and fracture behavior of nickel–titanium shape-memory alloy reinforced aluminum composites.* Materials Science and Engineering: A, 2001. **314**(1-2): p. 186-193.

82. Yi, S. and Gao, S., *Fracture toughening mechanism of shape memory alloys due to martensite transformation.* International journal of solids and structures, 2000. **37**(38): p. 5315-5327.

83. Liu, Y., Al-Matar, B., and Newaz, G., *An investigation on the interface in a NiTi short-fiber-reinforced 6061 aluminum composite by transmission electron microscope.* Metallurgical and Materials Transactions A, 2008. **39**(11): p. 2749-2759.

84. Leser, W., Newman, J., Hochhalter, J., Gupta, V., and Yuan, F., *Embedded Ni–Ti particles for the detection of fatigue crack growth in AA7050.* Fatigue & Fracture of Engineering Materials & Structures, 2016.

85. Craciunescu, C., Kishi, Y., Saraf, L., Ramesh, R., and Wuttig, M., *Ferromagnetic NiMnGa and CoNiGa Shape Memory Alloy Films.* Materials Research Society, 2002. **687**: p. 3.1-3.6.

86. Tseng, L., Ma, J., Hornbuckle, B., Karaman, I., Thompson, G., Luo, Z., and Chumlyakov, Y., *The effect of precipitates on the superelastic response of [100]*

oriented FeMnAlNi single crystals under compression. Acta Materialia, 2015. **97**: p. 234-244.

87.   Sutou, Y., Imano, Y., Koeda, N., Omori, T., Kainuma, R., Ishida, K., and Oikawa, K., *Magnetic and martensitic transformations of NiMnX (X= In, Sn, Sb) ferromagnetic shape memory alloys.* Applied Physics Letters, 2004. **85**(19): p. 4358-4360.

88.   K. Ito, W.I., R.Y. Umetsu, S. Tajuma, H. Kawaura, R. Kainuma, and K. Ishida, *Metamagnetic shape memory effect in polycrystalline NiCoMnSn alloy fabricated by spark plasma sintering.* Scripta Materialia, 2009. **61**: p. 3.

89.   Monroe, J., Raymond, J., Xu, X., Nagasako, M., Kainuma, R., Chumlyakov, Y., Arroyave, R., and Karaman, I., *Multiple ferroic glasses via ordering.* Acta Materialia, 2015. **101**: p. 107-115.

90.   Wang, Y., Salas, D., Medasani, B., Entel, P., Karaman, I., Arróyave, R., and Duong, T.C., *First-Principles Characterization of Equilibrium Vacancy Concentration in Metamagnetic Shape Memory Alloys: An Example of Ni2MnGa.* physica status solidi (b), 2018. **255**(2): p. 1700523.

91.   Pérez-Sierra, A., Bruno, N., Pons, J., Cesari, E., and Karaman, I., *Atomic order and martensitic transformation entropy change in Ni–Co–Mn–In metamagnetic shape memory alloys.* Scripta Materialia, 2016. **110**: p. 61-64.

92.   Stonaha, P.J., Karaman, I., Arroyave, R., Salas, D., Bruno, N.M., Wang, Y., Chisholm, M.F., Chi, S., Abernathy, D.L., Chumlyakov, Y.I., and Manley, M.E.,

Glassy Phonon Heralds a Strain Glass State in a Shape Memory Alloy. Physical Review Letters, 2018. **120**(24): p. 245701.

93.   Twite, R. and Bierwagen, G., *Review of alternatives to chromate for corrosion protection of aluminum aerospace alloys.* Progress in organic coatings, 1998. **33**(2): p. 91-100.

94.   Ito, K., Ito, W., Umetsu, R.Y., Nagasako, M., Kainuma, R., Fujita, A., Oikawa, K., and Ishida, K., *Martensitic transformation in NiCoMnSn metamagnetic shape memory alloy powders.* Materials transactions, 2008. **49**(8): p. 1915-1918.

95.   Suzuki, T., *Aluminium Manganese Nickel.* Ternary Alloys, VCH Verlagsgesellschaft, Weinheim, Germany, 1993. **7**: p. 84.

96.   Ohtani, H., Yamano, M., and Hasebe, M., *Thermodynamic analysis of the Co–Al–C and Ni–Al–C systems by incorporating ab initio energetic calculations into the CALPHAD approach.* Calphad, 2004. **28**(2): p. 177-190.

97.   Du, Y., Wang, J., Zhao, J., Schuster, J.C., Weitzer, F., Schmid-Fetzer, R., Ohno, M., Xu, H., Liu, Z.-K., and Shang, S., *Reassessment of the Al–Mn system and a thermodynamic description of the Al–Mg–Mn system.* International journal of materials research, 2007. **98**(9): p. 855-871.

98.   Raghavan, V., *Al-Mn-Ni (aluminum-manganese-nickel).* Journal of Phase Equilibria and Diffusion, 2006. **27**(5): p. 493-496.

99.   Kang, Y.-B. and Pelton, A.D., *Modeling short-range ordering in liquids: the Mg–Al–Sn system.* Calphad, 2010. **34**(2): p. 180-188.

100.   Dehoff, R., *Thermodynamics in materials science.* 2006: CRC Press.

101.   Xie, G., Ohashi, O., Yoshioka, T., Song, M., Mitsuishi, K., Yasuda, H., Furuya, K., and Noda, T., *Effect of interface behavior between particles on properties of pure Al powder compacts by spark plasma sintering.* Materials transactions, 2001. **42**(9): p. 1846-1849.

102.   Lindholm, U.S. and Yeakley, L.M., *High strain-rate testing: Tension and compression.* Experimental Mechanics, 1968. **8**(1): p. 1-9.

103.   Chmielus, M., Zhang, X., Witherspoon, C., Dunand, D., and Müllner, P., *Giant magnetic-field-induced strains in polycrystalline Ni–Mn–Ga foams.* Nature Materials, 2009. **8**(11): p. 863.

104.   Liu, Y., Karaman, I., Wang, H., and Zhang, X., *Two Types of Martensitic Phase Transformations in Magnetic Shape Memory Alloys by In-Situ Nanoindentation Studies.* Advanced Materials, 2014. **26**(23): p. 3893-3898.

105.   Frenzel, J., George, E.P., Dlouhy, A., Somsen, C., Wagner, M.F.X., and Eggeler, G., *Influence of Ni on martensitic phase transformations in NiTi shape memory alloys.* Acta Materialia, 2010. **58**(9): p. 3444-3458.

106.   Otsuka, K. and Ren, X., *Physical metallurgy of Ti–Ni-based shape memory alloys.* Progress in Materials Science, 2005. **50**(5): p. 511-678.

107.   Alvarez, K., Kim, H., and Miyazaki, S., *Effect of Alloying Elements on Microstructure, Martensitic Transformation and Mechanical Properties of Ni-Mn Based Alloys.* Journal of Materials Science and Technology, 2009. **25**(5).

108. Potapov, P., Shelyakov, A., Gulyaev, A., Svistunov, E., Matveeva, N., and Hodgson, D., *Effect of Hf on the Structure of Ni-Ti martensitic alloys.* Materials Letters, 1997. **32**: p. 247-250.

109. Evirgen, A., Ma, J., Karaman, I., Luo, Z.P., and Chumlyakov, Y.I., *Effect of aging on the superelastic response of a single crystalline FeNiCoAlTa shape memory alloy.* Scripta Materialia, 2012. **67**(5): p. 475-478.

110. Wu, D., Xue, S., Frenzel, J., Eggeler, G., Zhai, Q., and Zheng, H., *Atomic ordering effect in Ni50Mn37Sn13 magnetocaloric ribbons.* Materials Science and Engineering: A, 2012. **534**: p. 568-572.

111. Santamarta, R., Cesari, E., Font, J., Muntasell, J., Pons, J., and Dutkiewicz, J., *Effect of atomic order on the martensitic transformation of Ni–Fe–Ga alloys.* Scripta Materialia, 2006. **54**(12): p. 1985-1989.

112. Omori, T., Kamiya, N., Sutou, Y., Oikawa, K., Kainuma, R., and Ishida, K., *Phase transformations in Ni–Ga–Fe ferromagnetic shape memory alloys.* Materials Science and Engineering: A, 2004. **378**(1): p. 403-408.

113. Bruno, N.M., Salas, D., Wang, S., Roshchin, I.V., Santamarta, R., Arroyave, R., Duong, T., Chumlyakov, Y.I., and Karaman, I., *On the microstructural origins of martensitic transformation arrest in a NiCoMnIn magnetic shape memory alloy.* Acta Materialia, 2018. **142**: p. 95-106.

114. Wessel, J.K., *The handbook of advanced materials: enabling new designs*. 2004: John Wiley & Sons.

115. Barsoum, M. and Barsoum, M., *Fundamentals of ceramics*. 2002: CRC press.

116. Hornbogen, E., *The effect of variables on martensitic transformation temperatures.* Acta Metallurgica, 1985. **33**(4): p. 595-601.

117. Meeker, G.P., Bern, A.M., Brownfield, I.K., Lowers, H.A., Sutley, S.J., Hoefen, T.M., and Vance, J.S., *The Composition and Morphology of Amphiboles from the Rainy Creek Complex, Near Libby, Montana.* American Mineralogist, 2003. **88**(11-12): p. 1955-1969.

118. Willich, P. *EPMA—A Versatile Technique for the Characterization of Thin Films and Layered Structures.* 1992. Vienna: Springer Vienna.

119. Newbury, D.E. and Ritchie, N.W.M., *Performing elemental microanalysis with high accuracy and high precision by scanning electron microscopy/silicon drift detector energy-dispersive X-ray spectrometry (SEM/SDD-EDS).* Journal of Materials Science, 2015. **50**(2): p. 493-518.

120. Agangi, A., Przybyłowicz, W., and Hofmann, A., *Trace element mapping of pyrite from Archean gold deposits–A comparison between PIXE and EPMA.* Nuclear Instruments and Methods in Physics Research Section B: Beam Interactions with Materials and Atoms, 2015. **348**: p. 302-306.

121. Friel, J.J. and Lyman, C.E., *Tutorial Review: X-ray Mapping in Electron-Beam Instruments.* Microscopy and Microanalysis, 2006. **12**(1): p. 2-25.

122. Lowe, J., Barton, N., Blockley, S., Ramsey, C.B., Cullen, V.L., Davies, W., Gamble, C., Grant, K., Hardiman, M., Housley, R., Lane, C.S., Lee, S., Lewis, M., Macleod, A., Menzies, M., Müller, W., Pollard, M., Price, C., Roberts, A.P., Rohling, E.J., Satow, C., Smith, V.C., Stringer, C.B., Tomlinson, E.L., White, D.,

Albert, P., Arienzo, I., Barker, G., Borić, D., Carandente, A., Civetta, L., Ferrier, C., Guadelli, J.-L., Karkanas, P., Koumouzelis, M., Müller, U.C., Orsi, G., Pross, J., Rosi, M., Shalamanov-Korobar, L., Sirakov, N., and Tzedakis, P.C., *Volcanic ash layers illuminate the resilience of Neanderthals and early modern humans to natural hazards.* Proceedings of the National Academy of Sciences, 2012. **109**(34): p. 13532-13537.

123.   Hay, J.C., Bolshakov, A., and Pharr, G., *A critical examination of the fundamental relations used in the analysis of nanoindentation data.* Journal of materials Research, 1999. **14**(6): p. 2296-2305.

124.   Pharr, G.M., Strader, J.H., and Oliver, W., *Critical issues in making small-depth mechanical property measurements by nanoindentation with continuous stiffness measurement.* Journal of Materials Research, 2009. **24**(3): p. 653-666.

125.   Rho, J.-Y., Tsui, T.Y., and Pharr, G.M., *Elastic properties of human cortical and trabecular lamellar bone measured by nanoindentation.* Biomaterials, 1997. **18**(20): p. 1325-1330.

126.   Oliver, W.C. and Pharr, G.M., *An improved technique for determining hardness and elastic modulus using load and displacement sensing indentation experiments.* Journal of Materials Research, 2011. **7**(6): p. 1564-1583.

127.   Bei, H., George, E.P., Hay, J.L., and Pharr, G.M., *Influence of Indenter Tip Geometry on Elastic Deformation during Nanoindentation.* Physical Review Letters, 2005. **95**(4): p. 045501.

128.   Merle, B., Maier-Kiener, V., and Pharr, G.M., *Influence of modulus-to-hardness ratio and harmonic parameters on continuous stiffness measurement during nanoindentation.* Acta Materialia, 2017. **134**: p. 167-176.

129.   Tsui, T., Oliver, W., and Pharr, G., *Influences of stress on the measurement of mechanical properties using nanoindentation: Part I. Experimental studies in an aluminum alloy.* Journal of Materials Research, 1996. **11**(3): p. 752-759.

130.   Tsui, T.Y., Oliver, W.C., and Pharr, G.M., *Influences of stress on the measurement of mechanical properties using nanoindentation: Part I. Experimental studies in an aluminum alloy.* Journal of Materials Research, 2011. **11**(3): p. 752-759.

131.   Oliver, W.C. and Pharr, G.M., *Measurement of hardness and elastic modulus by instrumented indentation: Advances in understanding and refinements to methodology.* Journal of materials research, 2004. **19**(1): p. 3-20.

132.   Pharr, G. and Oliver, W., *Measurement of thin film mechanical properties using nanoindentation.* Mrs Bulletin, 1992. **17**(7): p. 28-33.

133.   Zhou, L., Giri, A., Cho, K., and Sohn, Y., *Mechanical anomaly observed in Ni-Mn-Ga alloys by nanoindentation.* Acta Materialia, 2016. **118**: p. 54-63.

134.   Pharr, G.M., Oliver, W.C., and Brotzen, F.R., *On the generality of the relationship among contact stiffness, contact area, and elastic modulus during indentation.* Journal of Materials Research, 2011. **7**(3): p. 613-617.

135.   Pharr, G. and Bolshakov, A., *Understanding nanoindentation unloading curves.* Journal of Materials Research, 2002. **17**(10): p. 2660-2671.

136. Zayak, A.T., Entel, P., Rabe, K.M., Adeagbo, W.A., and Acet, M., *Anomalous vibrational effects in nonmagnetic and magnetic Heusler alloys.* Physical Review B, 2005. **72**(5): p. 054113.

137. Radovic, M., Lara-Curzio, E., and Riester, L., *Comparison of different experimental techniques for determination of elastic properties of solids.* Materials Science and Engineering: A, 2004. **368**(1): p. 56-70.

138. Recarte, V., Zbiri, M., Jiménez-Ruiz, M., Sánchez-Alarcos, V., and Pérez-Landazábal, J.I., *Determination of the vibrational contribution to the entropy change at the martensitic transformation in Ni–Mn–Sn metamagnetic shape memory alloys: a combined approach of time-of-flight neutron spectroscopy and ab initio calculations.* Journal of Physics: Condensed Matter, 2016. **28**(20): p. 205402.

139. Kota, S., Agne, M., Zapata-Solvas, E., Dezellus, O., Lopez, D., Gardiola, B., Radovic, M., and Barsoum, M.W., *Elastic properties, thermal stability, and thermodynamic parameters of MoAlB.* Physical Review B, 2017. **95**(14): p. 144108.

140. Ağduk, S. and Gökoğlu, G., *First-principles study of elastic and vibrational properties ofNi2MnIn magnetic shape memory alloys.* The European Physical Journal B, 2011. **79**(4): p. 509-514.

141. Radovic, M. and Lara-Curzio, E., *Mechanical properties of tape cast nickel-based anode materials for solid oxide fuel cells before and after reduction in hydrogen.* Acta Materialia, 2004. **52**(20): p. 5747-5756.

142.   Seiner, H., Kopeček, J., Sedlák, P., Bodnárová, L., Landa, M., Sedmák, P., and Heczko, O., *Microstructure, martensitic transformation and anomalies in c'-softening in Co–Ni–Al ferromagnetic shape memory alloys.* Acta Materialia, 2013. **61**(15): p. 5869-5876.

143.   Radovic, M., Barsoum, M.W., Ganguly, A., Zhen, T., Finkel, P., Kalidindi, S.R., and Lara-Curzio, E., *On the elastic properties and mechanical damping of Ti3SiC2, Ti3GeC2, Ti3Si0.5Al0.5C2 and Ti2AlC in the 300–1573K temperature range.* Acta Materialia, 2006. **54**(10): p. 2757-2767.

144.   Migliori, A., Sarrao, J.L., Visscher, W.M., Bell, T.M., Lei, M., Fisk, Z., and Leisure, R.G., *Resonant ultrasound spectroscopic techniques for measurement of the elastic moduli of solids.* Physica B: Condensed Matter, 1993. **183**(1): p. 1-24.

145.   Leisure, R.G. and Willis, F.A., *Resonant ultrasound spectroscopy.* Journal of Physics: Condensed Matter, 1997. **9**(28): p. 6001.

146.   Maynard, J.D. *Resonant ultrasound spectroscopy*. in *Medical Imaging '98*. 1998. SPIE.

147.   Heczko, O., Seiner, H., Sedlák, P., Kopeček, J., Kopecký, V., and Landa, M., *Resonant ultrasound spectroscopy – a tool to probe magneto-elastic properties of ferromagnetic shape memory alloys.* The European Physical Journal B, 2013. **86**(2): p. 62.

148.   Gao, P., Bolon, A., Taneja, M., Xie, Z., Orlovskaya, N., and Radovic, M., *Thermal expansion and elastic moduli of electrolyte materials for high and*

intermediate temperature solid oxide fuel cell. Solid State Ionics, 2017. **300**: p. 1-9.

149. Saunders, N. and Miodownik, A.P., *CALPHAD (calculation of phase diagrams): a comprehensive guide.* Vol. 1. 1998: Elsevier.

150. Lukas, H., Fries, S.G., and Sundman, B., *Computational thermodynamics: the Calphad method.* 2007: Cambridge university press.

151. Andersson, J.-O., Helander, T., Höglund, L., Shi, P., and Sundman, B., *Thermo-Calc & DICTRA, computational tools for materials science.* Calphad, 2002. **26**(2): p. 273-312.

152. Manning, J.R., *Cross terms in the thermodynamic diffusion equations for multicomponent alloys.* Metallurgical and Materials Transactions B, 1970. **1**(2): p. 499-505.

153. Borgenstam, A., Höglund, L., Ågren, J., and Engström, A., *DICTRA, a tool for simulation of diffusional transformations in alloys.* Journal of phase equilibria, 2000. **21**(3): p. 269.

154. Larsson, H., *A model for 1D multiphase moving phase boundary simulations under local equilibrium conditions.* Calphad, 2014. **47**: p. 1-8.

155. Larsson, H. and Höglund, L., *Multiphase diffusion simulations in 1D using the DICTRA homogenization model.* Calphad, 2009. **33**(3): p. 495-501.

156. Anand, M. and Agarwala, R., *Diffusion of palladium, silver, cadmium, indium, and tin in aluminum.* 1967, Bhabha Atomic Research Centre, Bombay.

157. Chao, Y.-H., Chen, S.-W., Chang, C.-H., and Chen, C.-C., *Phase equilibria of Sn-Co-Ni system and interfacial reactions in Sn/(Co, Ni) couples.* Metallurgical and Materials Transactions A, 2008. **39**(3): p. 477-489.

158. Prince, A., *Aluminium-Nickel-Tin.* Ternary Alloys, VCH Verlagsgesellschaft, Weinheim, Germany, 1993. **7**: p. 3.

159. Committee, ASTM Handbook, *Metals handbook.* Vol. 2. 1973: American society for Metals.

160. Polmear, I., Stjohn, D., Nie, J.-F., and Qian, M., *Light alloys: metallurgy of the light metals.* 2017: Butterworth-Heinemann.

161. Orlov, D., Beygelzimer, Y., Synkov, S., Varyukhin, V., and Horita, Z., *Evolution of microstructure and hardness in pure Al by twist extrusion.* Materials Transactions, 2008. **49**(1): p. 2-6.

162. Ito, Y. and Horita, Z., *Microstructural evolution in pure aluminum processed by high-pressure torsion.* Materials Science and Engineering: A, 2009. **503**(1-2): p. 32-36.

163. Franke, P., *An assessment of the ordered phases in Mn–Ni using two-and four-sublattice models.* International Journal of Materials Research, 2007. **98**(10): p. 954-960.

164. Jain, K.C. and Bhan, S., *The system Sn-MnSn2-Ni3Sn4.* Transactions of the Indian Institute of Metals, 1965. **18**: p. 4.

165. Köster, W. and Rittner, H., *Aufbau und Eigenschaften der Kobalt-Nickel-Mangen-Legierungen.* Zeitschrift für Metallkunde, 1954. **45**: p. 4.

166.   Okamoto, H., *Mn-Sn (manganese-tin).* Journal of Phase Equilibria; Materials Park, 1999. **20**(5): p. 1.

167.   Schmetterer, C., Flandorfer, H., Richter, K.W., Saeed, U., Kauffman, M., Roussel, P., and Ipser, H., *A new investigation of the system Ni–Sn.* Intermetallics, 2007. **15**(7): p. 869-884.

168.   Somerday, M., Wert, J., and Comstock, R., *Effect of grain size on the observed pseudoelastic behavior of a Cu-Zn-Al shape memory alloy.* Metallurgical and Materials Transactions A, 1997. **28**(11): p. 2335-2341.

169.   Dvorak, I. and Hawbolt, E., *Transformational elasticity in a polycrystalline Cu-Zn-Sn alloy.* Metallurgical Transactions A, 1975. **6**(1): p. 95-99.

170.   Ma, J., Karaman, I., and Noebe, R.D., *High temperature shape memory alloys.* International Materials Reviews, 2010. **55**(5): p. 257-315.

171.   Evirgen, A., Basner, F., Karaman, I., Noebe, R.D., Pons, J., and Santamarta, R., *Effect of aging on the martensitic transformation characteristics of a Ni-rich NiTiHf high temperature shape memory alloy.* Functional Materials Letters, 2012. **5**(04): p. 1250038.

172.   Nam, T.H., Saburi, T., and Shimizu, K., *Cu-content Dependence of Shape Memory Characteristics in Ti-Ni-Cu Alloys.* Materials Transactions Jim, 1990. **31**(11): p. 959-967.

173.   Payne, J., Welsh, G., Christ, R.J., Nardiello, J., and Papazian, J.M., *Observations of fatigue crack initiation in 7075-T651.* International Journal of Fatigue, 2010. **32**(2): p. 247-255.

174. Upadhyaya, G.S., *Sintered Metallic and Ceramic Materials: Preparation, Properties, and Applications*. 1999: Wiley.

175. Eldridge, J., Hussey, R., Mitchell, D., and Graham, M., *Thermal oxidation of single-crystal aluminum at 550 C.* Oxidation of metals, 1988. **30**(5-6): p. 301-328.

176. Jeurgens, L., Sloof, W., Tichelaar, F., and Mittemeijer, E., *Thermodynamic stability of amorphous oxide films on metals: Application to aluminum oxide films on aluminum substrates.* Physical Review B, 2000. **62**(7): p. 4707.

177. Shinohara, K., Seo, T., and Kyogoku, H., *Transmission electron microscopy studies on the oxidation of aluminum.* Chemischer Informationsdienst, 1983. **14**(11): p. no-no.

178. Jeurgens, L., Sloof, W., Tichelaar, F., and Mittemeijer, E., *Structure and morphology of aluminium-oxide films formed by thermal oxidation of aluminium.* Thin solid films, 2002. **418**(2): p. 89-101.

179. Fang, Z.Z., *Sintering of advanced materials*. 2010: Elsevier.

180. Gutin, S., Panov, A., and Khlopin, M., *Effect of oxide films in the sintering of aluminum powders.* Powder Metallurgy and Metal Ceramics, 1972. **11**(4): p. 280-282.

181. James, D., Watanabe, T., and Yamada, K., *Effects of methods of adding copper on the strength of sintered aluminum copper alloys.* International Journal of Powder Metallurgy, 1968. **4**(3): p. 37-47.

182. Goetzel, C.G., *Treatise on powder metallurgy*. 1949: Interscience publishers.

183.   Dudas, J. and Dean, W., *The Production of Precision Alumininium P-M parts.* International Journal of Powder Metallurgy, 1969. **5**(2): p. 21-36.

184.   Kimura, A., Shibata, M., Kondoh, K., Takeda, Y., Katayama, M., Kanie, T., and Takada, H., *Reduction mechanism of surface oxide in aluminum alloy powders containing magnesium studied by x-ray photoelectron spectroscopy using synchrotron radiation.* Applied physics letters, 1997. **70**(26): p. 3615-3617.

185.   Kondoh, K., Kimura, A., and Watanabe, R., *Analysis of tin behaviour on surface of rapidly solidified aluminium alloy powder particles during heating.* Powder metallurgy, 2001. **44**(3): p. 253-258.

186.   Lumley, R., Sercombe, T., and Schaffer, G., *Surface oxide and the role of magnesium during the sintering of aluminum.* Metallurgical and Materials Transactions A, 1999. **30**(2): p. 457-463.

187.   Zhao, Y.H., Liao, X.Z., Zhu, Y.T., and Valiev, R.Z., *Enhanced mechanical properties in ultrafine grained 7075 Al alloy.* Journal of Materials Research, 2011. **20**(2): p. 288-291.

188.   Berg, L.K., Gjønnes, J., Hansen, V., Li, X.Z., Knutson-Wedel, M., Waterloo, G., Schryvers, D., and Wallenberg, L.R., *GP-zones in Al–Zn–Mg alloys and their role in artificial aging.* Acta Materialia, 2001. **49**(17): p. 3443-3451.

189.   Park, J.K. and Ardell, A.J., *Correlation between microstructure and calorimetric behavior of aluminum alloy 7075 and Al☐Zn☐Mg alloys in various tempers.* Materials Science and Engineering: A, 1989. **114**: p. 197-203.

190.   Adler, P.N. and Deiasi, R., *Calorimetric studies of 7000 series aluminum alloys: II. Comparison of 7075, 7050 and RX720 alloys.* Metallurgical Transactions A, 1977. **8**(7): p. 1185-1190.

191.   Richard, D. and Adler, P.N., *Calorimetric studies of 7000 series aluminum alloys: I. Matrix precipitate characterization of 7075.* Metallurgical Transactions A, 1977. **8**(7): p. 1177-1183.

192.   Ma, K., Wen, H., Hu, T., Topping, T.D., Isheim, D., Seidman, D.N., Lavernia, E.J., and Schoenung, J.M., *Mechanical behavior and strengthening mechanisms in ultrafine grain precipitation-strengthened aluminum alloy.* Acta Materialia, 2014. **62**: p. 141-155.

193.   Groza, J.R. and Zavaliangos, A., *Sintering activation by external electrical field.* Materials Science and Engineering: A, 2000. **287**(2): p. 171-177.

194.   Munir, Z.A., Anselmi-Tamburini, U., and Ohyanagi, M., *The effect of electric field and pressure on the synthesis and consolidation of materials: A review of the spark plasma sintering method.* Journal of Materials Science, 2006. **41**(3): p. 763-777.

195.   Matsugi, K., Wang, Y., Hatayama, T., Yanagisawa, O., and Kiritani, M., *Rapid consolidation by spark sintering of rapidly solidified 7075 aluminum alloy powder.* Radiation effects and defects in solids, 2002. **157**(1-2): p. 233-244.

196.   Wu, C., Fang, P., Luo, G., Chen, F., Shen, Q., Zhang, L., and Lavernia, E.J., *Effect of plasma activated sintering parameters on microstructure and*

mechanical properties of Al-7075/B4C composites. Journal of Alloys and Compounds, 2014. **615**: p. 276-282.

197.   Shen, Q., Wu, C., Luo, G., Fang, P., Li, C., Wang, Y., and Zhang, L., *Microstructure and mechanical properties of Al-7075/B4C composites fabricated by plasma activated sintering.* Journal of Alloys and Compounds, 2014. **588**: p. 265-270.

198.   Chua, A.S., Brochu, M., and Bishop, D.P., *Spark plasma sintering of prealloyed aluminium powders.* Powder Metallurgy, 2015. **58**(1): p. 51-60.

199.   International, ASTM., *Standard Practice for Heat Treatment of Wrought Aluminum Alloys.* 2017: West Conshohocken, PA.

200.   International, ASTM., *Standard Test Methods for Tension Testing Wrought and Cast Aluminum- and Magnesium-Alloy Products.* 2015: West Conshohocken, PA.

201.   Rokni, M.R., Widener, C.A., and Crawford, G.A., *Microstructural evolution of 7075 Al gas atomized powder and high-pressure cold sprayed deposition.* Surface and Coatings Technology, 2014. **251**: p. 254-263.

202.   Pascual, R., *Acoustic emission and dislocation multiplication during serrated flow of an aluminum alloy.* Scripta Metallurgica, 1974. **8**(12): p. 1461-1466.

203.   Leacock, A.G., Howe, C., Brown, D., Lademo, O.-G., and Deering, A., *Evolution of mechanical properties in a 7075 Al-alloy subject to natural ageing.* Materials & Design, 2013. **49**: p. 160-167.

204.	Dastur, Y.N. and Leslie, W.C., *Mechanism of work hardening in Hadfield manganese steel.* Metallurgical Transactions A, 1981. **12**(5): p. 749-759.

205.	Li, M. and Lege, D.J., *Serrated Flow and Surface Markings in Aluminum Alloys.* Journal of Engineering Materials and Technology, 1998. **120**(1): p. 48-56.

206.	Rodriguez, P., *Serrated plastic flow.* Bulletin of Materials Science, 1984. **6**(4): p. 653-663.

207.	Panigrahi, S.K. and Jayaganthan, R., *Effect of ageing on microstructure and mechanical properties of bulk, cryorolled, and room temperature rolled Al 7075 alloy.* Journal of Alloys and Compounds, 2011. **509**(40): p. 9609-9616.